



Forschungszentrum Karlsruhe
Technik und Umwelt

Wissenschaftliche Berichte
FZKA 6582

Damage Evaluation of Vertical Targets and First Walls during ITER-FEAT Off-normal Events

**H. Würz, S. Pestchanyi, I. Landman,
B. Bazylev, F. Kappler**

**Institut für Hochleistungsimpuls- und
Mikrowellentechnik
Programm Kernfusion**

März 2001

Forschungszentrum Karlsruhe

Technik und Umwelt

Wissenschaftliche Berichte

FZKA 6582

Damage evaluation of vertical targets and first walls during ITER-FEAT off-normal events

H. Würz, S. Pestchanyi¹, I. Landman¹, B. Bazylev², F. Kappler

Institut für Hochleistungsimpuls- und Mikrowellentechnik

Programm Kernfusion

permanent address

¹Troitsk Institute for Innovation and Fusion Research, 142092 Troitsk, Russia

²Luikov Institute of Heat and Mass Transfer, Minsk, Belarus

This work was performed in the frame of the EFDA Technology Programme T438 - 08 and was supported by the WTZ agreements RUS 99/566 and BLR 98/002

Forschungszentrum Karlsruhe GmbH, Karlsruhe

2001

Abstract

For modelling of hot plasma wall interaction, for calculation of erosion by evaporation of the ITER-FEAT vertical divertor target and for calculation of the impurity transport in the divertor, the 2-D R-MHD code FOREV-2 was developed. FOREV-2 uses a 2 ½ -D MHD model, a 2-D scheme for anisotropic radiation transport and a solution of the magnetic field equations in the plasma shield for all three components of the magnetic field.

Disruption simulation experiments performed at the plasma gun facilities at TRINITI Troitsk were used for validation of FOREV-2 and for investigations of the MHD of typical plasma shields. The 2-D numerical analysis of the disruption simulation experiments allows to conclude that such experiments adequately simulate the Tokamak plasma shield properties and its dynamics. From the results of the numerical analysis of the simulation experiments it is concluded that turbulence in the Tokamak shields is absent and that the stability of the cold and dense part of the Tokamak plasma shields which determines the target erosion can be adequately modeled by FOREV-2 by use of the classical magnetic field diffusion coefficient. Line radiation and an appropriate model for anisotropic radiation transport are necessary for a realistic calculation of radiation from the plasma shield. Moreover inclusion of line radiation allows to get a realistic radiation cooling of the plasma shield after switching off the heating.

The extensive validation exercise of FOREV-2 against disruption simulation experiments gives confidence that the numerical analysis of erosion for the ITER-FEAT vertical targets performed with FOREV-2 is based on sound principles and covers all important aspects of plasma shield behavior and plasma shield stability. In relation with vapor shields there still has to be answered the question whether a vapor shield exists in VDE events with peak target heat loads below 1 GW/m² and time duration up to 100 ms.

For simulation of brittle destruction in carbon based materials a 2-D numerical model was developed. By comparing the numerical results on brittle destruction with experimental results for volumetric heating and with results from mechanical destruction tests of graphite samples a typical failure stress value for surface bonds of $\sigma_{0s}=0.005$ was derived. Volumetric heating produces cracks inside of the sample, surface heating results in crack propagation into the depth of the sample. In both cases some predamageing of the sample might occur. Enhancement of brittle destruction under cyclic heat loads thus can't be excluded.

Melt layer erosion of metals is dominated by melt flow. For modelling of the melt flow a 1-D fluid dynamics model based on the shallow water approximation was developed. The driving force behind the melt flow was investigated. Lorentz forces might trigger a pronounced melt motion which might sweep away a considerable part of the melt layer. The melt layer erosion thus can be considerably larger than the melt thickness formed during the heat load period.

Melt layer erosion always is accompanied by splashing. Up to 20% of the eroded mass is splashed away by droplets. Flaking from redeposited layers, dust, melt flow and droplet splashing during disruptions produce complex layers with considerable surface roughness and drastically changed thermophysical properties. The hot spots of such layers are responsible for enhanced impurity production. A characterization of such layers is urgently required.

First numerical estimations show that the maximum tolerable ELM energy is noticeably lower for redeposited layers with considerable surface roughness than for the virgin vertical target and that the ELM energy has to be reduced to values below 4 MJ for vertical targets.

Zusammenfassung

Schädigung von vertikalem Target und erster Wand bei ITER-FEAT nicht normalen Betriebszuständen

Zur numerischen Simulation der Plasma Wand Wechselwirkung, zur Berechnung der Erosion durch Verdampfen an ITER-FEAT vertikalen Targets und zur Berechnung des Transports von Verunreinigungen wurde das 2-D Strahlungs-Magnetohydrodynamik-Programm (R-MHD) MHD FOREV-2 entwickelt. FOREV-2 verwendet ein 2 1/2-D Modell, ein 2-D winkelabhängiges Strahlungstransportmodell und eine Lösung der Magnetfeldgleichungen im Plasmaschild für alle 3 Magnetfeldkomponenten. Disruptions-Simulationsexperimente, die an den Plasmagananlagen von TRINITI Troitsk durchgeführt werden, wurden zur Validierung von FOREV-2 und zur Untersuchung des MHD Verhaltens typischer Plasmaschilde verwendet. Die 2-D numerische Analyse hat den Nachweis erbracht, dass die Simulationsexperimente die Eigenschaften und das MHD Verhalten von Tokamak Plasmaschilden simulieren. In diesen gibt es auch bei vertikalen Targets keine Turbulenz und zur Beschreibung des MHD Verhaltens kann der klassische Magnetfelddiffusionskoeffizient verwendet werden.

Zur numerischen Simulation der Brittle Zerstörung von Graphit wurde ein 2-D Modell entwickelt. Durch Vergleich der numerischen mit experimentellen Resultaten für volumetrische Heizung und mit Resultaten mechanischer Zerstörungstests konnte der Versagenswert für die Oberflächenbindung bestimmt werden. Volumetrische Heizung produziert Risse im Innern der Probe, Oberflächenheizung verursacht Risspropagation in die Tiefe der Probe. Dies kann zur Vorschädigung führen. Damit kann es bei zyklischer Wärmebelastung zu größerer Brittle Zerstörung kommen.

Die Erosion geschmolzener Metallschichten wird durch Fluidodynamik der Schmelze bestimmt. Ein 1-D fluiddynamisches Modell wurde zur Beschreibung der Schmelzbewegung entwickelt. Lorentz Kräfte können eine Schmelzbewegung triggern. Als Folge kann ein beträchtlicher Teil der Schmelzschicht weggespült werden. Dadurch kann die Erosionstiefe größer werden als die Dicke der Schmelzschicht.

Die Erosion geschmolzener Schichten wird begleitet von Splashprozessen. Bis zu 20% der geschmolzenen Masse kann als Tropfen weggesprüht werden. Abplatzungen von redeponierten Schichten, Staub, Schmelzbewegung und Tropfenbildung erzeugen Materialschichten mit beträchtlicher Oberflächenrauigkeit und drastisch reduzierter Wärmeleitfähigkeit. An den Hot spots solcher Schichten kommt es zu verstärkter Ablation. Erste numerische Abschätzungen zeigen, dass die pro ELM maximal tolerierbare Energie für redeponierte Schichten mit Oberflächenrauigkeit beträchtlich niedriger ist als für unversehrte Oberflächen und dass für vertikale Targets die Energie der ELMs unter 4 MJ bleiben muss.

CONTENTS

1	Introduction	1
2	Further improvements of the 2-D code FOREV-2	2
2.1	Heat conduction into the target and vaporization model	
2.2	Transfer of thermal energy to the target	
3	The plasma gun facility MK-200 UG for disruption simulation experiments	6
4	Thermal energy transfer in simulation experiments	7
5	Validation of FOREV-2 against results from the UG facility	8
5.1	Plasma shield properties, dynamics and erosion for perpendicular graphite targets	
5.2	Plasma shield dynamics and erosion for vertical targets	
6	Diamagnetic effects and plasma shield dynamics	12
6.1	Perpendicular target	
6.2	Vertical target	
7	Erosion of ITER-FEAT vertical targets	14
8	Impurity production and transport during ELMs	15
9	Brittle destruction of graphite	16
9.1	Damage threshold energy value	
9.2	Jebis electron beam simulation experiments	
9.3	Brittle destruction by run away electrons (RAES)	
10	Target screening by dust particles	19
10.1	Numerical results for JEBIS	
10.2	Numerical results for tokamaks and simulation experiments	
11	Melt layer erosion of metals	20
11.1	The 1-D fluid dynamics simulation of melt motion	
11.2	JEBIS electron beam simulation experiments	
11.3	Tokamak conditions	
11.4	Melt layer thickness in typical off normal events without melt motion	
11.4.1	Disruptions	
11.4.2	Run away electrons (RAEs)	
11.4.3	Vertical displacement events (VDEs)	
12	Numerical simulation of brittle destruction	27
12.1	Lattice model of graphite	
12.2	Numerical model of brittle destruction	
12.3	Crack generation during uniform heating	
13	Estimation of the characteristic failure stress value σ_{0s}	30
13.1	Mechanical compression test	
13.2	Volumetric energy deposition	
14	Conclusions	31
15	References	34

1 Introduction

Whether graphite or a high Z material (tungsten or molybdenum) will be used as divertor material is still an open issue. The low Z material graphite doesn't melt, shows rather low erosion by evaporation and has a low impurity radiation level. However chemical erosion and Tritium co-deposition might be unacceptably high [1,2]. Thermal stress produces cracks in graphite. Crack propagation into the depth of the sample indicates predamaging. Enhancement of brittle destruction under cyclic heat loads then can't be excluded [3]. This might increase total erosion of graphite considerably and could reduce the lifetime and by dust formation could cause a safety problem [3,4]. The high Z material tungsten has low sputtering yields and the contamination of the central plasma with tungsten remains low [5]. But there is melt layer erosion resulting in rather large total erosion, in formation of a large surface roughness and in droplet splashing as indicated in simulation experiments with electron beams [6]. The influence of melt motion on melt layer erosion was discussed recently for tokamak off normal events [7]. The influence of eddy currents on melt layer dynamics was recently emphasized [8]. However the numerical results given in [8] are not consistent and thus this problem still remains to be solved for tokamak off normal conditions. A combination of both materials such as graphite as vertical target and tungsten as dome material could result in still more complex surface layers being a mixture of graphite dust, of metal droplets of redeposited carbon and of flakes. Such layers show a drastically reduced heat conductivity and they might enhance impurity production at hot spots and thus could limit the tolerable ELM energy [7].

Before any recommendations for any material to be used as divertor material can be given the total erosion of these materials has to be quantified among others. Damage mechanisms to be considered are evaporation and brittle destruction of graphite and evaporation and melt layer erosion of metals. Vapor shielding and target screening by dust particles was taken into account in the numerical simulations [4].

A numerical simulation model for brittle destruction of carbon based materials (CBMs) based on crack generation by thermal shocks is under development. Crack generation in heated graphite samples depends among others on the grain anisotropy, the grain size, the failure stress value of the bonds connecting adjacent grains and on the temperature and the temperature gradient in the sample. The value to be used for the characteristic failure stress was obtained from a numerical simulation of destructive compression tests and from a comparison of calculated and measured onset of brittle destruction for volumetric heating. Crack propagation into the depth of the sample indicates that predamaging might occur resulting in an enhancement of brittle destruction under cyclic heat loads for typical ITER-FEAT off-normal events [3].

Erosion in metals is mainly due to melt layer motion. For description of melt motion, mountain formation at the crater edge and melt layer erosion a 1-D fluid dynamics model is being developed and first numerical results on melt layer erosion and formation of mountains were obtained [9].

For calculation of target erosion by evaporation, the plasma shield formation and its shielding efficiency in front of the target have to be known. For this purpose the 2-D multifluid radiation magnetohydrodynamics (R-MHD) code FOREV-2 was developed. FOREV-2 validation is completed with numerical simulation of plasma shield dynamics and erosion of perpendicular and vertical graphite targets and comparison with experimental results obtained at the MK-200 UG plasma gun facility. Plasma shield stability is essential for a high shielding efficiency and needs to be modelled for calculation of realistic erosion values. FOREV-2 was used for calculation of erosion of vertical targets by hot plasma impact typical for off normal events in ITER-FEAT.

2 Further improvements of the 2-D code FOREV-2

For a reliable prediction of tokamak divertor erosion by evaporation the physical properties and the long term behavior of the plasma shield have to be known but can't be studied in existing tokamaks. Because of the rather small power density of the disruptive hot plasma in present day tokamaks evaporation of target material is negligible at these machines. Moreover operation of appropriate diagnostics during a disruption is not guaranteed. Experimental facts can only be obtained from disruption simulation experiments performed in such plasma gun facilities which allow to produce plasma shields and to analyse their behavior under the guidance of an external magnetic field [10]. First activities on physical properties of plasma shields were related with simulation experiments at the 2 MK-200 CUSP facility at TRINITI Troitsk and with 1-D modelling [11]. 2-D modelling however is required for ITER-FEAT because of the rather complicated divertor geometry with possible tilting of targets in the poloidal plane (vertical targets) and the asymmetrical power density profile of the impacting hot plasma across the SOL [12] because of the rather complex dynamics of the plasma shield [13] and because of reradiation from the plasma shield to the side walls and other nearby components with possible damage to these components [14]

The plasma shields in the disruption simulation experiments are two temperature plasmas [15] with a rather dense cold plasma layer close to the target and a low dense rather hot plasma corona. Target shielding in the simulation experiments mainly is provided by the cold dense plasma. Target erosion thus depends on the dynamics and the stability of this cold plasma layer.

An adequate modelling of the plasma shield dynamics is a necessary prerequisite for a realistic quantification of the erosion of the ITER-FEAT vertical targets and of calculation of impurity transport. Therefore a comparison of numerical and experimental results on plasma shield formation, on plasma shield properties and dynamics for perpendicular and vertical targets was performed and consequences for target erosion by evaporation are discussed.

FOREV-2 is a 2-D two fluid radiation magneto hydrodynamics code and thus allows a 2-D modelling of magnetized hot plasma target interaction. FOREV-2 is described in [15]. Therefore here only further improvements which have been implemented recently and which are not documented up to now will be discussed. This concerns a consistent vaporization model and an analysis of the role and importance of the thermal energy transfer for the calculation of the target heat load of targets shielded by plasma shields.

Before starting the discussion the 2-D numerical grids used for the calculations for horizontal and vertical targets are described. Fig. 1 shows the simplified 2-D geometry describing one ITER-FEAT divertor leg with a horizontal and a vertical target in the poloidal plane. The distance along the target is counted positive in upstream direction with the separatrix strike point (SSP) at zero. The same geometry is used for the modeling of the simulation experiments as is to be seen from Fig. 2 showing the scheme of the 2-D geometry of the simulation experiments (xy plain) performed at the MK-200 UG facility for a perpendicular and a vertical target. As there is no toroidal magnetic field the "horizontal target" is called perpendicular target to indicate that the magnetic field lines B_x are perpendicular to the target surface. The experimental geometry schematically shown in Fig. 2 is 2-D cylindrical for perpendicular but 3-D for vertical (tilted) targets. The 2-D experimental geometry is approximated in 2-D planar geometry in the (xy) plain by assuming the same dependencies in y and z direction. The cylindrical hot plasma beam has a Gaussian power density profile in y- and z-direction with a full width at half maximum of 7 cm. For vertical targets the experimental geometry can be described only in an approximative manner in a 2-D planar system.

For horizontal targets the computational region is up to $150 \times 40 \text{ cm}^2$ (x and y). There is used a grid with meshes growing in size in x-direction and homogeneous in y-direction as shown in Fig. 3a. Typical mesh sizes in a region up to a few cm distance from the target are $2 \times 2 \text{ mm}^2$. In total up to 60×80 meshes are used. For vertical targets the computational region is up to $220 \times 40 \text{ cm}$. It is represented by two different grids as shown in Fig. 3b. Close to the target there is used a grid with homogeneous meshes. Further away a grid with meshes growing in size in x-direction and homogeneous in y-direction is used. Two different numbers of total meshes were used; 100×40 with typical mesh size of $5 \times 5 \text{ mm}^2$ in region 1 and 200×100 meshes with mesh size of $2 \times 2 \text{ mm}^2$ in region 1.

2.1 Heat conduction into the target and vaporization model

For the calculation of the heat conduction into the solid and liquid target the heat fluxes from the plasma region are used. It is assumed that the incoming heat fluxes from the hot SOL plasma ions S_{hi} , from radiation S_{rad} and from thermal energy transfer S_{th} are deposited at the target surface. The Maxwellian plasma electrons from the incoming hot SOL plasma are volumetrically heating the bulk of the target.

The 2-D heat conduction equation taking into account the motion of the vaporization front with u_{vap} the velocity of this front is given as

The 2-D heat conduction equation is given as

$$\rho c \frac{\partial T}{\partial t} = \vec{\nabla} \cdot (\kappa \vec{\nabla} T) + u_{vap} \rho c \frac{\partial T}{\partial x} + S_{he} \quad (1)$$

The heat capacity $c(T)$ is given as

$$c(T) = \begin{cases} c_s, & \text{if } T < T_m - \frac{\Delta T}{2} \\ \frac{1}{2}(c_s + c_l) + \frac{Q_m}{\Delta T}, & \text{if } T_m - \frac{\Delta T}{2} < T < T_m + \frac{\Delta T}{2} \\ c_l, & \text{if } T_m + \frac{\Delta T}{2} < T \end{cases} \quad (2)$$

With c_s the specific heat of the solid target

c_l the specific heat of the liquid

T_m the melt temperature

Q_m the heat of melting

$\Delta T \ll T_m$ small temperature intervall (usually $\Delta T = 0.01 T_m$) used for numerical simulation of the phase transition between the solid and the liquid phase (Stefan problem [16]).

$$\kappa(T) = \begin{cases} \kappa_s, T < T_m \\ \kappa_l, T > T_m \end{cases} \quad (3)$$

S_{he} the volumetric heating by hot plasma electrons given as

$$\sum_i N_i v_i \frac{dE_i}{dx} \text{ is described in [15]}$$

ρ, T density and temperature of the bulk material

The boundary between the solid and liquid phase inside of the target is defined by the condition $T(x,y) = T_m + \Delta T$.

The melt front velocity u_m is calculated according to

$$\kappa_s \frac{\partial T}{\partial x} \Big|_{\chi=\zeta-0} - \kappa_l \frac{\partial T}{\partial x} \Big|_{\chi=\zeta+0} = -\rho Q_m u_m \quad (4)$$

The heat conduction equation (eq. (1)) is solved in 2 substeps using the local 1-D technique, according to

$$\begin{aligned} \rho c \frac{\partial T}{\partial t} &= \frac{\partial}{\partial x} \left(\kappa \frac{\partial T}{\partial x} \right) + u_{vap} \rho c \frac{\partial T}{\partial x} + S_{he} \\ \rho c \frac{\partial T}{\partial t} &= \frac{\partial}{\partial y} \left(\kappa \frac{\partial T}{\partial y} \right) \end{aligned} \quad (5)$$

The boundary conditions for eq.(1) are

$T_{x \rightarrow \infty} \rightarrow T_{\text{room}}$ and at the evaporating surface

$$-\kappa \left. \frac{\partial T}{\partial x} \right|_{x=0} = S_{\Sigma} - \rho u_{\text{vap}} \Delta H_{\text{vap}} \quad (6)$$

with ΔH_{vap} the enthalpy for evaporation and $S_{\Sigma} = S_{\text{th}} + S_{\text{hi}} + S_{\text{he}}$ the total surface heat load. Temperature dependent data for c and κ are taken from [17].

Although principally the 2-D heat conduction equation is used in FOREV-2 its solution in x -direction only is sufficient because the characteristic length of the temperature distribution in y -direction (along the target) is about 4 orders of magnitude larger than in x -direction.

Surface evaporation starts when the surface temperature achieves a value T_s for which the pressure of the saturated vapor equals or exceeds the external pressure given as sum of the stagnation pressure $p = \frac{1}{2} \rho u^2$ (with u the ion impact velocity and ρ the ion density) and the pressure of the evolving plasma shield. u_{vap} is calculated using the nonsteady state model of surface evaporation [18,19] based on a kinetic model of the vapor expansion inside of the Knudsen layer as described in appendix A1. Using u_{vap} the eqs. (1) and (5) are solved iteratively till the relative change of T_s remains below 0,1 %.

The fluxes of mass of vapor F_m , of energy F_E and of momentum F_F entering the plasma shield at the cell next to the vaporization position (the first mesh of the numerical grid) are calculated according to

$$\begin{aligned} F_m &= \rho_g u_g \Delta y \\ F_E &= \frac{3}{2} \frac{\rho_g}{m_c} u_g T_g \Delta y \\ F_F &= \rho_g u_g^2 \Delta y \end{aligned} \quad (7)$$

with Δy the width of the mesh and m_c the mass in this mesh. The quantities density ρ_g and velocity u_g of the expanding vapor and its temperature T_g are obtained from the nonsteady state model as described in appendix A1.

2.2 Transfer of thermal energy to the target

Adjacent to the target the temperature in the plasma shield across a rather thin layer may change from vaporization temperature T_{vap} at the target surface to some value T_{max} with up to several eV at the right boundary of this layer. Heating of this layer is mainly by electron heat conduction and most energy is consumed for ionization. Assuming single charged carbon ions in this layer only the temperature at this right boundary can be restricted to $T_{\text{max}} =$

1,5 eV. The typical size of the ionization layer is 10 μm and thus much less than any mesh size in a realistic 2-D numerical calculation. For obtaining a realistic temperature drop in the first mesh an analytical mode for calculation of the effective target surface temperature T_b based on a hydrodynamic approach was developed and is described in the appendix A2. The parameters flux of evaporating atoms j_o ; pressure at the target surface P_o and target heat load W_o ; are known from FOREV-2. In each FOREV-2 time step these parameters are used to calculate the temperature profile near the target starting from T_{vap} till T_{max} and the thickness δ of this layer. δ is compared with the width Δ of the first mesh in FOREV-2. For small values of the target heat load W_o it is valid $\delta > \Delta$ and the boundary temperature T_b is calculated according to

$$T_b = T_{vap} + (T_{max} - T_{vap}) \frac{\Delta}{\delta} \quad (8)$$

if $\delta < \Delta$ then it is used $T_b > T_{max}$. Using the values T_b a more realistic thermal energy transfer S_{th} from the plasma shield to the target is calculated by the use of the electron heat conduction equation according to

$$S_{th} = \kappa \frac{dT}{dx} \quad (9)$$

with κ the electron heat conductivity and T the temperature in the plasma shield.

As shown in the appendix A2 the thermal energy transfer S_{th} in the hydrodynamics approximation can't exceed the value of the neutral kinetic heat flux $S_{th,n}$ which is given according to

$$S_{th,n} = \alpha N_n u_{thn} T_{vap} \quad (10)$$

With α an accommodation coefficient of typically $\frac{1}{2}$, $u_{thn} = (2 T_{vap}/m_a)^{1/2}$ the atom thermal velocity, N_n the density of the atoms and T_{vap} the vaporization temperature.

3 The plasma gun facility MK-200 UG for disruption simulation experiments

Magnetized plasma stream target experiments were performed at the plasma gun facility MK-200 UG of TRINITI Troitsk [10]. The plasma β value is around 0.3. The plasma ion impact energy is about 1,5 keV. The Maxwellian distributed electrons have temperatures up to 300 eV. In the simulation experiments there is no toroidal magnetic field ($B_z=0$). The targets are either perpendicular to the guiding magnetic field given as $B_0 = (B_x, 0, 0)$ or tilted with respect to B_x . In the MK-200 UG facility the experimental geometry schematically shown in Fig.2 is 2-D cylindrical for perpendicular targets but 3-D for tilted targets. The time evolution of the hot plasma as used in the calculations is shown in Fig. 4 with a full width at half maximum of around 25 μs . Peak power density is reached after about 10 μs , remains constant for 15 μs and then decays exponentially. The guiding magnetic field is 2 T at the target position. The peak power density is 350 GW/m^2 . The position of the peak power density of the Gaussian profile in the following is called separatrix.

At the simulation facility target erosion experiments and local measurements of electron temperature and density were performed in carbon plasma shields by Thomson laser scattering (TS). Optical interferometry (IF) was used for a measurement of line averaged electron density distributions along the target surface at different target distances. The lines of sight for the interferometry are indicated in Fig. 1. A detailed discussion of diagnostics used is given in [11].

4 Thermal energy transfer in simulation experiments

The influence of the thermal heat flux S_{th} to the target on the modelling results was studied. Three different variants for calculation of S_{th} were used. Firstly S_{th} was calculated according to eq. (9) with adjusted wall temperature as described in appendix A2 (the reference case), secondly for S_{th} was used the kinetic flux of neutrals (see eq (10)) with the three values for the accommodation coefficient α with $\alpha = 0, 1$ and 3 and finally an extreme case was used with S_{th} described by an electron kinetic flux given according to

$$S_{th,e} = N_e u_{the} (T_e - T_{vap}) \quad (11)$$

With $u_{the} = (2T_e/m_e)^{1/2}$ the electron thermal velocity, N_e the electron density, T_{vap} the vaporization temperature and T_e the plasma temperature. T_e , N_e and u_{the} depend on the distance from the target and thus on the size of the first mesh.

For the MK-200 UG facility with its peak power density of 350 GW/m^2 calculated target heat fluxes at the separatrix strike point (SSP) are shown in Fig. 5 for the above mentioned 5 cases. Using for S_{th} the kinetic flux of neutrals with $\alpha = 1$ yields target heat loads rather comparable to the reference case. Increasing S_{th} results in a decrease of the radiative heat load and in an increase of the erosion rate as is seen from Fig. 6. The carbon density close to the target increases with increasing erosion rate, as a consequence the plasma temperature drops there and thus the radiative target heat load decreases. The time dependent total target heat load for the 3 cases of neutrals kinetic flux with $\alpha = 0$ and 3 and for the reference case remains rather constant as can be seen from the calculated erosion which varies between $0.35 \text{ }\mu\text{m}$ and $0.45 \text{ }\mu\text{m}$. The measured value is $0.4 \text{ }\mu\text{m}$. Moreover the plasma shield dynamics is rather similar in all cases. Thus the thermal target heat load S_{th} only weakly influences the numerical results and in all further calculations S_{th} was assumed to be calculated according to the reference case. For the extreme case with the thermal energy transfer given by the electron kinetic flux the time dependent total target heat load is larger at early times but drops faster at later times (see Fig. 5). Consequently the erosion rate is largest at early times but becomes zero after $15 \text{ }\mu\text{s}$. The plasma shield dynamics at early times is only slightly different with a more pronounced flow of plasma towards the separatrix.

5 Validation of FOREV-2 against results from the UG facility

Due to the time duration of the hot plasma of up to 50 μs plasma shields are produced and a rather dense and cold plasma layer appears close to the target. Experiments at the UG facility thus allow to investigate the MHD expansion of the hot and of the cold part of the plasma shield. For the numerical simulations of the UG facility 69 group Planck opacities were used for describing the optical properties of the carbon plasma shields. Calculations were performed for classical and Bohm diffusion and in one case 24 group Rosseland opacities were used. For the magnetic field diffusion coefficient of the graphite target a χ_m value of $1,5 \cdot 10^5 \text{ cm}^2/\text{s}$ was used describing the situation with B_x frozen in at the target.

5.1 Plasma shield properties, dynamics and erosion for perpendicular graphite targets

Fig. 7 shows the calculated plasma flow pattern and the electron density distribution in the carbon plasma shield at 24 μs and 38 μs for the dense cold carbon plasma with temperature below 2eV. At early times and close to the target there is a flow of dense cold plasma toward the separatrix then along the separatrix upstream and laterally outward thus forming lateral plasma jets outside of the separatrix. At 30 μs flow reversal occurs in the dense cold plasma close to the target and at 38 μs the outward plasma flow is rather well developed. At 24 μs the dense plasma layer at the separatrix has grown to a thickness of 2.1 cm whereas the lateral plasma jets extend over a length of about 6.5 cm. At 38 μs the dense plasma layer has grown to a thickness of 5 cm and the lateral plasma jets extend over a length of about 16 cm. Also indicated in Fig. 7 are lines of sight for the interferometry measurements (IF) and the Gaussian power density profile of the incoming hot plasma with the position of the separatrix.

Fig. 8 shows calculated electron density distributions in the carbon plasma shield (in y-direction) along the IF lines of sight at 30 μs and 40 μs for different distances from the target. The lateral plasma jets are clearly to be seen as density peaks outside of the central axis evolving at target distances larger than 2 cm. Fig. 9 shows a comparison of calculated and measured line averaged electron density distributions. The calculated values were obtained by averaging over the density distributions shown in Fig. 8 assuming that the plasma shield shows cylindrical symmetry. Shown is the quantity $n(x) = \frac{1}{R} \int_0^R n(r, x) dr$ passing the beam

axis. There is agreement between measurement and calculation at 10 μs as seen from Fig. 9. At 30 μs and 40 μs the calculated values at distances larger than 2 cm from the target are also quite adequately reproducing measured values.

Fig. 10 shows a comparison of calculated and measured local electron temperature profiles along the separatrix. The temperature increase at 30 μs occurs at a target distance of 1.5 cm at 40 μs at 5 cm and at 50 μs at 8 cm thus indicating the extension of the dense cold plasma along the separatrix. The measured and calculated carbon plasma density and temperature values demonstrate that FOREV-2 results are describing the MHD expansion of the dense cold plasma along the separatrix adequately. Fig. 11 shows a comparison of measured (by Thomson scattering TS) and calculated evolution of the local electron density and tempera-

ture at the separatrix at 3 cm and 10 cm distance from the target. The sudden drop in electron temperature at 30 μs corresponds to a decrease of the power density of the incoming hot plasma, to the arrival of the denser part of the plasma shield at the measurement position and to an effective radiative cooling down of the plasma due to line radiation emitted laterally from the plasma shield. At 3 cm distance from the target the density peak arrives about 6 μs earlier in the calculation than in the measurement and the calculated amplitude is about 60% larger. At 10 cm the TS values of electron density show a continuous increase with time whereas the calculation again shows the arrival of a dense plasma at 45 μs . Between 20 μs and 40 μs the calculated values are a factor of 2 smaller than the TS data but are in agreement with the IF data which indicate at distances above 7 cm density values below 10^{17} cm^{-3} . Using 24 group Rosseland opacities results in an overestimation of electron densities close to the target and in a drastic overestimation of the electron temperature at later times indicating again that the lateral leakage radiation flux from the plasma shield is drastically underestimated when using Rosseland opacities.

There are only minor differences in the calculated temperature profiles along the separatrix as is to be seen from Fig. 10 when using classical and Bohm diffusion. From the rather identical time evolution of the thickness of the dense cold plasma layer at the separatrix it is concluded that the MHD behavior of the cold dense plasma practically remains the same for classical and Bohm diffusion. Moreover there is no significant difference in the calculated evolution of electron density and temperature (see Fig. 11). The numerical results using classical diffusion are even in closer agreement with the experimental results.

The TS value on electron density at 40 μs and at a target distance of 2 cm with $2.5 \times 10^{17} \text{ cm}^{-3}$ is in agreement with the calculated value shown in Fig. 8. Unfortunately at 30 μs and at target distances below 3 cm TS data on electron densities are not available. Thus the IF data at 30 μs (Fig. 7)) close to the target can't be checked. A comparison of the TS and IF data on electron density confirms the existence of lateral jets. At 30 μs and 3 cm distance the TS value is below 10^{17} cm^{-3} , the IF value is about $4 \times 10^{17} \text{ cm}^{-3}$. Thus the density valley at the center as shown in the calculated density distributions along the target surface (see Fig. 8) is confirmed by the measurements. The calculated value at 30 μs and at 3 cm distance is below 10^{17} cm^{-3} and thus in good agreement with the TS value.

Finally Fig. 12 shows the time evolution of the surface temperature for the perpendicular graphite target due to the external pressure being the sum of the stagnation pressure of the impacting hot plasma and the pressure of the plasma shield. Under the UG conditions T_s achieves about $T_s = 1,3 T_{\text{vap}}$ with T_{vap} the boiling temperature in vacuum. Erosion measurements were also performed for perpendicular and tilted quartz targets. At the quartz target the poloidal field lines are not frozen in but are moving freely. To simulate this the magnetic field diffusion coefficient χ_m of the target was assumed to be $\chi_m = 10^6 \text{ cm}^2 / \text{s}$. Fig. 13 shows the calculated plasma flow pattern and the quartz density distribution in the plasma shield at two different time moments for a horizontal target. The plasma close to the target all the times flows along the target in outward direction away from the separatrix and thus shows a rather different behavior in comparison with graphite.

5.2 Plasma shield dynamics and erosion for vertical targets

FOREV-2 validation is completed with the numerical simulation of the plasma shield dynamics and of erosion of vertical graphite targets and comparison with experimental results obtained at the MK-200 UG plasma gun facility (vertical means target surface tilted with respect to the poloidal magnetic field(see Fig.2)).

Recently disruption simulation experiments have been performed at the plasma gun facility MK-200 UG at Troitsk with vertical graphite targets, inclined at 20° to the direction of the incident hot hydrogen plasma [10]. The experimental arrangement schematically is shown in Fig. 14. The peak target heat load in these experiments was 100 GW/m^2 . In the experiments the SSP was located only 2 cm away from the upstream target edge. Thus the target covered only the downstream half of the power density profile. Experimentally determined have been the erosion profiles and the time integrated visible and soft X-ray radiation. Moreover time dependent photographs of visible radiation were taken by a high speed framing camera. From the plasma pictures which showed that the radiating region at the target widens it was concluded that the plasma expands along the target downstream and thus across the magnetic field lines. From the additionally measured time integrated soft X-ray spectras CV and CVI lines have been found near the target, indicating plasma temperatures higher than 20 eV (CV and CVI ions exist in noticeable quantities only at such temperatures). Thus it was concluded that a high temperature plasma moves across the magnetic field lines. This was at first understood by assuming that turbulence exists in the plasma shield [20].

From the results of the numerical analysis of this experiment with FOREV-2 using the classical Spitzer diffusion coefficient other conclusions were drawn. First of all, from the widening of the radiative spot close to the target it can't be concluded that there is a movement of hot plasma across magnetic field lines. From Fig. 15 it is seen that the widening of the radiative spot is due to an increase of the width of the vaporization region with time reflecting the width of the Gaussian profile of the incoming power density. Fig. 16 shows calculated plasma electron temperature distributions along the axis, perpendicular to the target at the SSP and at different times. A high temperature plasma shield exists at distances less than 1 cm only during the first about $9 \mu\text{s}$. At later times due to ongoing evaporation and consequently increasing carbon density as seen from Fig. 17a cold plasma layer is formed near the target. Calculated plasma flow patterns are shown in Fig. 18 at two different times. The arrows indicate the plasma flow $\Gamma = N_c v$ with N_c the carbon density and v the velocity, the lines show carbon density contours. The densities N_c are indicated. At early times the plasma flow is strictly along the magnetic field lines. After formation of the cold plasma layer there occurs a downstream drift of the plasma shield along the target surface in the part of the target downstream of the SSP. In the upstream part of the target (upstream of the SSP) as is seen from Fig. 19 showing the whole target there is a pronounced flow of cold plasma upstream. There is another interesting fact. As seen from Figs. 15 and 17 both the erosion profile and the carbon density are gradually shifted upstream with time. As a consequence the final position of the maximum erosion is 6 cm upstream of the SSP. This is not a consequence of the downstream plasma drift but is caused by reradiation from the expanding plasma shield. The radiative target heat load from the expanding plasma shield shows a maximum upstream of the SSP because the radiation has shorter distances to the upstream part of the target and

moreover hits it under angles closer to 90° . The increase of the upstream shift with time is caused by the expansion of the radiation region away from the target.

The theoretically predicted upstream shift of the erosion profile is confirmed by the experimental results. Fig. 20a shows measured erosion profiles for the vertical target in downstream direction and for a perpendicular target. The profile width is rather similar for both targets. However the vertical target because of the tilting angle of 20° should show a profile widening of a factor of 3. There is only one possible explanation: namely upstream shift of the erosion profile for the vertical target by 70 mm. As can be seen from Fig. 15 this experimentally determined profile shift is in quite good agreement with the theoretically predicted value of 6 cm. Measured erosion profiles for a perpendicular and a vertical quartz target are shown in Fig. 20b. For the vertical target the SSP was at a distance of about 9 cm from the upstream target edge and the figure shows the downstream erosion profile. The full widths at half maximum of the erosion profiles are 11 cm for the perp target and 40 ± 2 cm for the vertical target. Taking into account the tilting angle of 20° then it is seen that the full width at half maximum of the erosion profile of the vertical target is about 7 cm larger. This increase is due to the predicted upstream shift.

Figs. 21a and b show calculated radiative target heat load profiles for a vertical graphite and a quartz target demonstrating the upstream shift of the radiation profiles.

The rather complex distribution of radiation inside of the plasma shield of a tilted graphite target is shown in Fig. 21. The arrows indicate the direction and the value of the radiation flux. The radiative target heat load as seen from Fig. 21 comes from the radiating bubble which with on going time moves upstream. In the vicinity of this bubble the radiation flux is highly anisotropic. To describe such a situation adequately anisotropic radiation transport has to be used [15].

Fig. 22 shows the calculated plasma flow pattern and the quartz density distribution in the plasma shield for a vertical quartz target at two different times. Despite the rather different boundary conditions for the magnetic field at the target surface (frozen in at graphite and free movement at quartz) the plasma flow pattern is rather similar for both target materials. There is always a downstream drift of cold plasma in the region downstream of the SSP and in the upstream part of the target there is a flow of cold plasma upstream

Measured and calculated target erosion values are listed in Table 2 for graphite and quartz. Because of the low impact energy in the simulation experiments direct energy deposition is negligible as target heat load source. The target heat load is dominated by radiation. As is seen from Table 2 the mesh size influences the calculated erosion for tilted targets. For mesh sizes of typically $2 \times 2 \text{ mm}^2$ the calculated erosion values are in reasonable agreement with the measured values. Use of larger mesh sizes results in an overestimation of the calculated radiative target heat load and thus in erosion as is seen from Fig. 23 which shows a comparison of calculated radiative target heat loads for two different mesh sizes. Fig. 24 shows the calculated time evolution of the peak radiative target heat load and of the impacting hot plasma.

6 Diamagnetic effects and plasma shield dynamics

The dynamics of the experimental plasma shields for horizontal and vertical targets are determined by the MHD of the cold dense plasma layer close to the target surface. The plasma shield dynamics depends on the pressure distribution inside of the plasma shield and on the geometry of the external magnetic field. The magnetic field geometry is influenced by the plasma shield itself (diamagnetic effect) by the boundary condition for the magnetic field at the solid target and by its diffusion coefficient in the plasma shield. In case of a two temperature plasma shield as it exists in the experimental plasma shields (see for instance Fig. 10) both the low dense hot part and the rather dense but cold part of the plasma shield contribute to the diamagnetic effect. Plasma turbulence if occurring at all in plasma shields is related with the hot part only and as a consequence a turbulent hot plasma produces no diamagnetic effect and thus can't influence the dynamics of the cold dense plasma layer. The influence of the diamagnetic effect on the MHD behavior of the dense cold part and on target erosion was quantified. Numerical investigations were performed for the experimental conditions of the UG facility. For carbon plasma shields 69 group Planck opacities were used for describing the optical properties of the carbon plasma [15].

6.1 Perpendicular target

Fig. 25 shows the calculated plasma flow pattern and the plasma density distribution in a carbon plasma shield at $30 \mu\text{s}$ for classical diffusion for a horizontal graphite target. The two boundary conditions free movement of the magnetic field at the target ($\chi_m = 10^6 \text{ cm}^2/\text{s}$) and magnetic field frozen in at the target surface ($\chi_m = 2 \cdot 10^4 \text{ cm}^2/\text{s}$) were assumed. Additionally shown are the calculated pressure profiles of the plasma shield close to the target. The plasma flow regimes are rather different for both cases. For the frozen in case there is a flow of cold plasma towards the separatrix within a layer of a few mm. The inward flow results in the formation of a dense cold plasma close to the SSP which then flows along the separatrix upstream. After $30 \mu\text{s}$ the thickness of this layer (in y-direction) with carbon densities up to 10^{19} cm^{-3} has grown to 2 cm, after $40 \mu\text{s}$ to 4 cm as is seen from Fig. 17 showing plasma temperature profiles along the separatrix for the two different flow regimes. The lateral width of this dense layer (in y-direction) is about 4 cm. In this regime the plasma temperature remains below 2 eV, everywhere else in the plotted region it remains below 5eV.

For the case of magnetic field not frozen in at the target there is a flow of cold dense plasma outward. This again occurs within a layer of thickness of a few mm. Due to the outward flow the carbon density at the separatrix decreases to values below 10^{18} cm^{-3} and the plasma temperature increases as seen from Fig. 26 to values above 10 eV. Along the separatrix thus no cold dense plasma layer is formed plasma shielding at the SSP is reduced and as a consequence the erosion at the SSP increases as is seen from Fig. 27 which shows calculated erosion profiles for three different values of the magnetic field diffusion coefficient χ_m at the target. For non frozen magnetic field because of plasma flow away from the separatrix the erosion profile is strongly peaked and the highest erosion value is achieved with a peak erosion value of $0.8 \mu\text{m}$. For the frozen in situation ($\chi_m = 2 \times 10^4 \text{ cm}^2/\text{s}$) with its plasma flow to the separatrix the erosion in the center is about $0.3 \mu\text{m}$ and the erosion profile becomes wider. For intermediate χ_m values ($\chi_m = 1.5 \times 10^5 \text{ cm}^2/\text{s}$) the plasma flow to the separatrix in

comparison with the frozen in case is reduced but is still existing. Thus shielding at the separatrix is improved and a peak erosion of 0.45 μm is obtained. The measured peak erosion value is 0,4 μm determined as average value after 15 shots. Calculated target heat fluxes are shown in Fig. 28 for the perpendicular graphite target. During all times radiation dominates the target heat load. Direct energy deposition continues up to 4 μs . Afterwards the hot plasma stream is fully stopped in the plasma shield. Its energy deposition to the target remains below 4 J/m^2 . The contribution of the thermal energy transfer to the target heat load is negligible.

To summarize this discussion: the plasma shield efficiency for horizontal targets sensitively depends on the MHD behaviour of the cold dense plasma which exists rather close to the target. According to the y component of the momentum equation which writes as

$$\frac{\partial \rho u_y}{\partial t} + \bar{\nabla} \rho u_y \bar{u} + \frac{\partial}{\partial y} \left(P + \frac{B^2}{2\mu_0} \right) - \frac{I}{\mu_0} (\bar{B} \bar{\nabla}) B_y = 0 \quad (12)$$

a lateral plasma motion (in y direction) occurs due to the gradient of the total pressure $\frac{\partial P_{tot}}{\partial y} = \frac{\partial}{\partial y} (P + B^2/8\pi)$ and due to the evolution of the y component of the poloidal magnetic field with initially $B_y=0$ (fourth term of the left hand side eq. (12)). The plasma pressure of the impacting hot plasma is shown in Fig. 29 at different times. The diamagnetic effect of the plasma shield pushes B_x away from the separatrix (dilution of B_x). The time evolution of the pressure of the poloidal magnetic field B_x is shown in Fig. 30. Comparing Figs. 29 and 30 it is seen that the pressure of the poloidal magnetic field B_x is comparable to the plasma pressure. Due to this the problem becomes quite simple. The evolution of the total pressure is shown in Fig. 31. The diamagnetic effect results in a reduction of the pressure gradient of the total pressure. The resulting pressure gradient drives an outward movement of the cold plasma away from the separatrix. This is valid for both cases frozen in and not frozen in. The case of magnetic field frozen in the diamagnetic effect of the plasma shield results additionally in a bending of the magnetic field lines near the target and thus a y-component of the poloidal magnetic field (B_y) arises as shown in Fig. 32 for lateral positions below the separatrix. Fig. 32 shows the time evolution of the y-component of the magnetic field for the both cases frozen in and not frozen in B_x field at the target. Later in time ($t > 30 \mu\text{s}$) pushing out the B_x in the plasma shield decreases because of decreasing plasma shield pressure and due to the diffusion of B_x in the bulk target B_y disappears. The B_y term dominates in the motion equation and thus as long as $B_y \neq 0$ the lateral motion of the cold plasma for the frozen in magnetic field is towards the separatrix. Later in time when $B_y = 0$ the pressure term dominates and flow reversal occurs with outward flow of the cold plasma.

6.2 Vertical target

Calculated plasma flow patterns in plasma shields of vertical targets are rather similar for the two cases with the boundary conditions free movement of the magnetic field at the target and magnetic field frozen in at the target. From this it is concluded that the plasma pressure gradient determines the downstream drift of the cold dense plasma in the lower part of the tar-

get. For the case of frozen in magnetic field at the target the time behavior of the poloidal magnetic field B_x in the carbon plasma shield is shown in Fig. 33 for two different time moments for the conditions of the MK-200 UG facility. Pushing away of B_x and formation of a B_y component of the magnetic field occurs essentially downstream of the SSP. There the plasma pressure gradient dominates and therefore despite an opposing force due to B_y the dense cold plasma flows downstream away from the SSP. Upstream of the SSP because of zero B_y the plasma pressure gradient and the upstream shift of erosion cause the upstream flow of the cold dense plasma. The upstream shift of erosion is due to reradiation from the plasma shield as discussed in chapter 5.2. This reradiation is coming from the rather narrow transition region between the cold rather dense plasma layer close to the target and the hot plasma corona. Turbulence in the hot plasma corona does not influence the reradiation but could influence the diamagnetic effect of the plasma shield. The diamagnetic effect as shown only weakly influences the dynamics of the cold dense plasma layer. Therefore turbulence in the hot plasma corona does not influence neither the dynamics of the cold dense plasma layer nor its long term stability

7 Erosion of ITER-FEAT vertical targets

The off normal events used for damage evaluation of the ITER-FEAT divertor and the first walls (FW) are listed in Table 1. The inclination of the magnetic field lines in toroidal direction is 2° , the target inclination in the poloidal plane is 20° . Fig. 14 also describes the tokamak situation but only in the poloidal plane. The power density profile across the scrape off layer (SOL) is unsymmetrical and not Gaussian [15]. Target materials considered are graphite and tungsten. The two peak target heat loads 3 and 30 GW/m^2 with 10 ms and 1 ms time duration (total energy density of the hot plasma of 30 MJ/m^2 in each case) were used. The toroidal magnetic field was assumed to be 5 T . Fig. 34 shows the obtained results on erosion profiles and time evolution of target heat loads for tungsten vertical targets. Fig 35 shows the results for graphite vertical targets.

The SSP is at position zero and the positive direction is along the target upstream. The target heat loads belong to the position of maximum erosion. Similar to the results from the simulation experiment (compare Fig. 34 with Fig. 15) the erosion profiles for the 30 GW/m^2 case always are shifted upstream with respect to the SSP. This upstream shift is caused by reradiation from the expanding plasma shield. The upstream shift at 1 ms is up to 40 cm for tungsten. There is erosion where the power density of the impacting hot plasma is below 3 W/m^2 and negligible erosion at the SSP with peak power density of 30 GW/m^2 . With only direct heating negligible evaporation would occur at the 3 GW/m^2 position within 1 ms . The shift rate in the tokamak case is much less than for the UG facility. For the tokamak case because of the toroidal inclination angle of the magnetic field lines of 2° the plasma shield expansion velocity along the separatrix in the poloidal plane is smaller than for the UG facility where there is no such toroidal inclination. The smaller expansion velocity keeps the radiating region closer at the SSP and thus causes the smaller shift rate in comparison with the UG situation. The time dependence of the upstream shift of the radiative target heat load is shown in Fig. 36 for a tungsten vertical target and in Fig. 37 for the graphite vertical target. The reduced radiative target heat load at the SSP and the more pronounced plasma drift along the target surface downwards favoured by the unsymmetrical power density profile of

the impacting hot plasma and by the larger density of the cold plasma close to the target provide the strong shielding at the SSP which effectively results in zero erosion there.

The situation is quite different for the low power density case (3 GW/m^2) having larger heat deposition times. For the case with downstream SSP there is only a small upstream shift of the peak erosion in relation to the SSP. As can be seen from the time evolution of the target heat loads direct heating dominates up to 1,0 ms, evaporation starts after 1 ms when radiation contributes to the target heat load. 0,5 ms later the radiative target heat load decreases again. The radiation is confined to a narrow region around the SSP and therefore the upstream shift of the erosion profile remains rather small. Again zero erosion at the SSP is due to downstream drift of the plasma.

Despite a factor of 10 lower power density of the impacting hot plasma the erosion for tungsten because of longer deposition times and reduced plasma shielding efficiency becomes comparable to the high power density case. Whereas for graphite erosion increases by a factor of 25 and gets values of up to 10 microns after 2,7 ms. Vertical targets are effectively dissipating the energy in high power density off normal events. For low power densities however vertical targets offer no advantage in comparison with horizontal targets.

Fig. 38 shows the results on erosion profiles and time evolution of target heat loads for tungsten dome targets upstream separatrix. The erosion values for high and low peak power densities are comparable and are up to a factor of 2,5 larger than for the case of the downstream separatrix. For the 30 GW/m^2 case there is an upstream shift of the erosion profile again caused as discussed previously by reradiation from the plasma shield. The shift is smaller than for the case with downstream separatrix because there is lacking preheating of the upstream part of the target by the impacting hot plasma. Fig. 39 shows the time evolution of the carbon plasma shield for a vertical graphite target. Below the separatrix and at times up to $100 \mu\text{s}$, there is a predominant plasma drift downstream along the target surface and an upward movement of the plasma shield outside of the separatrix. With increasing upstream shift of erosion upstream motion dominates. Figs. 40 and 41 show the time evolution of the tungsten plasma shield for a vertical tungsten target and for the tungsten dome target with separatrix upstream. In both case dominates the downstream flow. Outside of the impacting SOL plasma the target plasma bubble moves upward towards the x-point.

8 Impurity production and transport during ELMs

ELMs when depositing their energy into layers with roughened surfaces might result in enhanced impurity production at hot. This might have been experienced at JET when after the Be melt experiment a standard discharge with separatrix strike point (SSP) just at the damaged area ended with a density limit disruption [21]. Hot spot impurity production was analysed by use of the multifluid 2D radiation magneto-hydrodynamics (R-MHD) code FOREV-2 [15]. The heat load at the vertical target with inclination angle of 20° was assumed to be 1 GW/m^2 during 0.5 ms. In this first estimation it is assumed that 10% of the heat deposited area consists of hot spots which then because of energy conservation are heated by 10 times the nominal target heat load. The hot spots in this first estimation are assumed to consist of the same material as the bulk target.

For graphite the heat conductivity was reduced by a factor of 4 to simulate redeposited layers. Fig. 42 shows the calculated evolution of carbon density distributions for densities in the range from 10^{14} to 10^{18} cm^{-3} and the flow pattern (arrows, Nv) in the plasma shield of the outer divertor leg of ITER-FEAT. During target heating by the ELM two plasma fans form on either side of the separatrix. After switching off heating the cold dense plasma to the target surface drifts downstream along the target surface in agreement with results from simulation experiments with vertical targets [20]. The low dense plasma with densities up to 10^{15} cm^{-3} moves between the outer wall and the separatrix upwards towards the x-point. In total $2 \cdot 10^{19}$ carbon atoms have been evaporated per 1 cm toroidal length during the ELM. About 25% of them will approach the x-point.

Fig. 43 shows the calculated evolution of tungsten density distributions for the density range from 10^{14} to 10^{17} cm^{-3} and the flow pattern in the plasma shield. During heating the tungsten plasma shield shows a pronounced downstream drift along the target surface. After switching off heating a weak downstream drift continues but the plasma now mainly moves close to the separatrix upwards towards the x-point. The total number of tungsten atoms between .3 and 1.2 m distance from the separatrix strike point per 1 cm of toroidal length is shown in Fig. 44. $8 \cdot 10^{17}$ tungsten atoms have been evaporated and after 5 ms about $2 \cdot 10^{17}$ atoms are approaching the ITER-FEAT x-point. The graphite and tungsten ion/neutral flux close to the x-point typically are $6.5 \cdot 10^{22}$ atoms/ cm^2s $1.2 \cdot 10^{20}$ atoms/ cm^2s . In total $6 \cdot 10^{20}$ tungsten atoms and 10^{22} carbon atoms are reaching the x-point. These neutrals both have the potential to dissipate a considerable fraction of the thermal energy of the central plasma. Therefore an ELM energy of 0.5 MJ/m^2 under the hot spot conditions as described is hardly tolerable.

Flaking from redeposited layers, dust, melt flow and droplet splashing produced during disruptions produce complex layers with considerable surface roughness and drastically changed thermophysical properties. The hot spots of such layers are responsible for enhanced impurity production. A characterization of such layers is urgently required. First numerical estimations show that the maximum tolerable ELM energy is noticeable lower for redeposited layers with considerably surface roughness than for the virgin vertical target.

9 Brittle destruction of graphite

The estimations on brittle destruction of graphite as discussed here are based on a phenomenological approach using a threshold energy value for onset of brittle destruction as suggested in [22]. A realistic model of brittle destruction based on cracking of bonds between the different grains under thermal shocks is discussed below. Impact of hot electrons results in volumetric heating, being calculated by Monte Carlo [23]. The evolution of surface temperature and of profiles of temperature and accumulated specific energy in the bulk are calculated by solution of the 2-D heat conductivity equation. The motion of dust particles and target screening by these particles are calculated by the multifluid 2-D radiation magneto hydrodynamics code FOREV-2 [15].

9.1 Damage threshold energy value

The experimental results on total erosion of graphite of the GOL-3 electron beam facility were used to determine the damage threshold value for onset of brittle destruction with volumetric heating [22]. Due to the short pulse duration and the rather high power density of the electron beam erosion by evaporation remains below 10 microns and the total erosion is due to brittle destruction. Significant brittle destruction starts at a deposited energy of about (11 ± 1) MJ/m². Considerable scattering of the experimental data with a band width of ± 2 MJ/m² was observed. For the numerical simulation of brittle destruction the spectral distribution of the flux of electrons used in the GOL-3 experiments was approximated by the 4 distributions shown in Fig. 45a called original and modified M1 to M3 together with some experimental data for which error bars were not specified [22]. The modified flux spectra differ in the intensity of the high energetic electrons. Decreasing this intensity from the spectrum original to M3 the flux of the intermediate electrons was increased within limits compatible with the experimental data points. The energy deposition corresponding to the different spectra normalized to 1 MW/cm² and calculated by Monte Carlo are shown in Fig. 45b. Calculated erosion curves based on these different energy depositions are shown in Fig. 46 for two different damage threshold values together with the experimental erosion curves. Assuming validity of the spectrum original requires rather high damage threshold values to get agreement between calculated and measured erosion. The trend in erosion when going from the original spectrum via M1 to M3 is also clearly to be seen, the erosion rate decreases. But only for the spectra M2 and M3 the experimental values can be reproduced and only when introducing damage threshold values which are dependent from the depth position inside of the bulk sample. In concluding there is no clear indication for a unique damage threshold value to be derived from the GOL-3 experiments not only because of the scattering of the experimental erosion data but also because of the rather drastic influence of the flux spectrum of the electron beam which is not known with adequate accuracy. Using a constant threshold value only allows to reproduce onset of brittle destruction and erosion up to about 150 microns.

Brittle destruction occurs several times during the 5 μ s heat deposition time. In each of these events a layer of material is destroyed. The maximum thickness of each destroyed layer remains below 100 microns per event. Onset of brittle destruction is due to electrons up to 200 keV. The frequent sequence of brittle destruction can be explained from Fig. 47 showing typical profiles of deposited specific energy in the bulk sample for spectrum M3. Volumetric energy deposition results in rather broad distributions of deposited energy. Upon reaching the damage threshold value the material layer up to the depth where this condition is fulfilled is destroyed. The emitted material adds to the target shielding. The bulk is further heated starting now at a larger surface temperature.

Because of the short time intervall involved the emitted dust particles are assumed to be at rest. Their density is up to a factor of 2 smaller than solid density. Target screening is taken into account in such a way that the electrons after having passed through the eroded layer are impacting with reduced energy onto the new solid surface behind the destructed layer. The energy loss in the dust layer is seen from Fig. 48 showing the initial energy spectrum of the electrons and the spectra after transmission of 200 and 400 microns of graphite. In the dust layer of thickness of 200 microns 44% of the energy is absorbed, in the 400 micron

layer 67%. Comparing the energy spectra of Fig. 48 it is seen that the high energetic electrons essentially are slowed down in energy by keeping their spectral shape constant. The energy loss is approximately 0,1 MeV per 200 microns.

9.2 Jebis electron beam simulation experiments

A comparison of measured and calculated total mass losses (evaporation and brittle destruction) for pyrolytic graphite and for CFC for the JEBIS facility [24] for a 70 keV electron beam with peak power density of 1,8 GW/m² Gaussian power density profile of half width of 5 mm and pulse duration of 2 ms is shown in Fig. 49a for CFC graphite and in Fig. 49b for pyrolytic graphite of different initial temperatures. Included in Figs. 49a and b is the calculated mass loss due to brittle destruction. A mass loss of 1 mg corresponds to an erosion depth of 65 microns. The size of the dust particles typically is a few microns. For calculation of brittle destruction the damage threshold energy value of 10 kJ/g was used. Brittle destruction only weakly depends on the initial temperature of the sample. Fig. 50 shows the calculated energy deposition of the monoenergetic electrons of energy of 70 keV into graphite for different impact angles. The reflected energy is indicated in the figure. Fig. 51 shows the calculated time dependencies of brittle destruction and of evaporation for the same damage threshold value of 10 kJ/g for fine grain graphite of initial temperature of 1200 K. Brittle destruction occurs several times within the heat load deposition time of 2 ms. Changing the damage threshold value in the range from 8 to 11 kJ/g changes total erosion only by about $\pm 10\%$ but mainly influences the contribution of evaporation and brittle destruction. For 8 kJ/g total erosion is by brittle destruction, for 11 kJ/g brittle destruction is reduced by a factor of 2,5. Reducing the damage threshold energy value (absorbed specific energy) means a reduction of the surface temperature of the bulk target. The relation between both is shown in Fig. 52.

Target screening by the carbon vapor is of no concern in these JEBIS experiments because the vapor density within the region of the impacting electron beam as obtained from a 2-D hydrodynamic calculation of the expansion of the ablated material into vacuum with FOREV-2 remains rather small. Fig. 53 shows the calculated vapor flow and the vapor densities in the cloud. The arrows indicate the particle flow Γ given as $\Gamma = n_c v$ with n_c the carbon density and v its velocity. The lines describe density contours with given densities. The vapor density drops within a distance of 1 cm from the target by more than a factor of 10 to values below $2 \cdot 10^{17} \text{ cm}^{-3}$. Therefore the energy deposition into the vapor cloud is negligible. The vapor temperature is around 0,7 eV and thus consists of neutrals.

9.3 Brittle destruction by run away electrons (RAES)

The impact energy of the RAEs was assumed to be 15 MeV and the guiding magnetic field 5T. The calculated energy deposition into graphite is shown in Fig 54 for different impact angles of the magnetic field lines. Numerical results on total erosion and brittle destruction under RAE impact of energy density of 50 MJ/m² and inclination angle of 1° are shown in Figs. 55a and b for CFC graphite for different target heat loads and two different damage threshold values. For 0.5 GW/m² the specific energy within 100 ms remains below 9 kJ/g. There is occurring only evaporation. Reducing the damage threshold value to 8 kJ/g in-

creases brittle destruction considerably and evaporation drops down to 10 microns. Now brittle destruction also occurs for 0.5 GW/m².

10 Target screening by dust particles

Target screening due to the dust particles from brittle destruction in these JEBIS experiments was investigated with FOREV-2. It is assumed that brittle destruction and levitation of dust particles occur when a surface layer of the thickness of 2 microns has accumulated a certain amount of specific energy which corresponds to the threshold energy value for onset of brittle destruction. The particles start with a velocity of 10⁴ cm/s perpendicular to the target surface. Different threshold energy values were used.

The particle transport using the hydrodynamic approximation treats the dust as a gas with density equal to the number of particles per unit volume and gas velocity equal to the mean particle velocity. The equations for dust particle transport are

$$\frac{\partial N_d}{\partial t} + \text{div}(N_d \mathbf{V}_d) = 0 \quad \frac{\partial \mathbf{V}_d}{\partial t} = \frac{\mathbf{F}_{drag}}{M_d} \quad (13)$$

with N_d the density of dust particles, \mathbf{V}_d their mean velocity, \mathbf{F}_{drag} a drag force and M_d the mass of the dust particle. For numerical solution of the dust particle motion equations the same technique is applied as for the motion of the plasma shield [15].

The drag force \mathbf{F}_{drag} imposed by the surrounding plasma shield ions is obtained from a kinetic approach by integration of the momentum transfer of the plasma shield ions resulting in

$$\mathbf{F}_{drag} = C \rho_{pl} V_{thi} \Delta \mathbf{V} S_d \quad (14)$$

with ρ_{pl} the plasma density, V_{thi} the thermal velocity of the plasma shield ions $\Delta \mathbf{V} = \mathbf{V}_{plasma} - \mathbf{V}_d$ the relative velocity between dust particles and plasma ions, S_d the cross section of the dust particles and C a coefficient of order of 1 depending on the shape of the particles. For calculation of \mathbf{F}_{drag} it is assumed that the carbon plasma ions impinge on the rear and front side surfaces of the dust particles with a Maxwellian shifted by $\pm \Delta \mathbf{V}$.

10.1 Numerical results for JEBIS

The numerical simulation of target screening by dust particles for JEBIS was performed for 70 keV electrons with peak power density of 1,8 GW/m² with Gaussian power density profile of half width of 5 mm and pulse duration of 2 ms. The vapor is heated by the impacting hot electrons. The vaporised mass contributes to the plasma shield. Results on dust particle motion are shown in Fig. 56 at three different times after onset of a brittle destruction event at 1.2 ms. The dust cloud due to pressure gradients initially expands isotropically. Later the isotropy is destroyed in the region where the electron beam heats and evaporates the parti-

cles. After about 130 μs the dust vapour cloud becomes transparent again for the electron beam as can be seen from Fig. 57 showing the energy deposition into the target which with onset of brittle destruction drops to half the initial value but recovers within 130 μs .

Moreover it is seen that the time during which the target is shielded decreases with ongoing time. This is due to the increasing density of the background vapor which drives the dust particles by drag forces [4].

10.2 Numerical results for tokamaks and simulation experiments

For numerical simulation of dust particle behaviour in a plasma shield and of target screening a horizontal graphite target and a peak target heat load of 100 GW/m^2 were assumed. The plasma shield motion and plasma densities in the poloidal plane are shown in Fig. 58 without dust particles. The plasma shield moves along the target surface away from the separatrix strike point (SSP) thus depleting the shielding there.

Fig. 59 shows the calculated motion pattern of the dust particles together with the evolving plasma shield. Evaporation of dust particles is taken into account. It is assumed that all radiative energy transferred to the particles is spent for vaporization. The vaporized mass contributes to the plasma shield. The radiative energy transfer from the plasma shield to the target is influenced by the dust particles. This is taken into account by using a modified absorption coefficient for the plasma shield containing dust particles.

The influence of different damage threshold energy values on total erosion was investigated for the MK-200 UG plasma gun facility with a horizontal target and a peak power density of 350 GH/m^2 . The total erosion when decreasing the damage threshold value for brittle destruction from 10 to 6.4 kJ/g increases only by 50% because of improved target screening by the dust particles. Target screening results in drastically reduced surface temperatures as seen from Fig. 60. Fig. 61 shows the time dependent brittle destruction. For the damage value of 8.6 kJ/g brittle destruction occurs only once during the first 5 μs , then the target remains screened for the remaining heat load period. For lower damage threshold values a first brittle destruction event occurs early in time, then target screening reduces the surface temperature. Later the temperature increases again resulting in a second brittle destruction event followed again by a temperature reduction due to the improved target screening. Similar results were obtained for ITER-FEAT conditions. In this first estimation a vertical graphite target with realistic power density profile, peak target heat load of 30 GW/m^2 and heat load deposition time of 1 ms was used. Without brittle destruction erosion is 2.5 microns. Using the damage threshold value of 10 kJ/g total erosion becomes 5 microns half of that is by brittle destruction.

11 Melt layer erosion of metals

Experimental results from e-beam facilities on melt layer erosion demonstrate the existence of a rather pronounced motion in the melt layer [6,25]. As a result mountains of ejected melt material are formed at the crater edge as is demonstrated in Fig. 62 for tungsten showing typical results for the JEBIS facility which is operated without external magnetic field [6].

Preliminary melt layer erosion experiments at plasma gun facilities have been performed for aluminum [26,27]. The observed typical mountains at the crater edge again indicate melt motion. 70 keV electrons simulate for tungsten a surface heat load. Penetration is less than 3 microns as is to be seen from Fig. 63 showing the calculated energy deposition for 3 different impact angles. Moreover as is also indicated in Fig. 63 because of absence of a guiding magnetic field a significant fraction of electrons is reflected.

During such off-normal events as disruptions, ELMs and VDEs (see Table 1) the energy flux at the targets reaches values sufficient for melting of metals and a thin melt layer appears at the target surface. Melt motion might increase significantly the erosion of metallic divertor plates. Therefore the investigation of the melt layer dynamics is an important problem for the lifetime evaluation of metallic components. The numerical simulation of melt motion is based on a 1-D fluid dynamics model using the shallow water approximation [28]. This drastically facilitates the problem as compared to a 2-D modelling [29]. The modelling is described in [9].

11.1 The 1-D fluid dynamics simulation of melt motion

A plane target surface is assumed. According to Fig. 64 the fluid forms at the initially solid surface due to melting caused by the surface heat load S_{Σ} . The surface of the fluid is described by the function $h(y,t)$, the solid surface determined by the thermal transport in the fluid is described by the function $H(y, t)$. It is assumed that the width L of the molten layer is much larger than h and H . In this case the shallow water approximation is valid [28] in which the physical parameters in the fluid equations are averaged over the fluid thickness $X(y, t) = H + h$. The fluid is assumed to be incompressible.

The physical processes taken into account in the model of melt layer dynamics are:

heating, melting and melt front propagation; heat transport in the fluid;
melt motion by the following forces: viscosity, surface tension, pressure of the saturated vapor (plasma shield), gravitational force, stagnation pressure of the impacting plasma, Lorentz force due to external and Eddy currents.

The fluid velocity V_y and the temperature T in the fluid are averaged over the melt layer thickness X according to $A = \frac{1}{X} \int_{-H}^h A(x) dx$. For averaging a parabolic dependence of V_y and T on X is assumed. X is described by the continuity equation, V_y by the averaged Navier stokes equation and T by the averaged heat conduction equation according to

$$\frac{\partial X}{\partial t} + \frac{\partial}{\partial y} (XV_y) = u_m \quad (15)$$

$$\frac{dV_y}{dt} = g_y - \frac{V_y u_m}{X} + \frac{3k_\alpha}{2X\rho} \frac{\partial T(X)}{\partial y} - \frac{3\nu V_y}{X^2} - \frac{\partial P}{\rho \partial y} + \frac{J_x B_z}{\rho c} \quad (16)$$

gravity friction due surface viscosity pressure Lorentz
to increment tension gradient force
of fluid mass

$$\frac{dT}{dt} = \frac{3S_\Sigma}{2\rho c_p X} - \frac{3\kappa T}{\rho c_p X^2} - \frac{T u_m}{X} + \frac{3\nu V_y^2}{c_p X^2} + \frac{1}{c_p \nu} \left(\frac{k_\alpha}{2\rho} \frac{\partial T(X)}{\partial y} \right)^2 + \frac{J_x^2}{\sigma \rho c_p} \quad (17)$$

external thermal cooling due viscosity heating by surface Joule
heating conduction to increment heating tension heating
of fluid mass

with P the total pressure given as

$$P = P_{ext} + \rho g_x h - \alpha \frac{\partial^2 X}{\partial y^2} \quad (18)$$

$$T(X) = \frac{3}{2} T + \frac{S_\Sigma X}{4\kappa} \quad (19)$$

and \vec{g} the gravitational constant, α the surface tension with $k_\alpha = d\alpha/dt$, ρ the density of the fluid, ν the viscosity, κ the thermal conductivity P_{ext} the external pressure given as $P_{ext} = P_{irr} + P_{sat}$ with the P_{irr} the irradiation pressure and P_{sat} the pressure of the saturated vapor at the surface. In case of irradiation of the target by electrons P_{sat} gets larger than P_{irr} . P_{sat} is a known function of the surface temperature $T(X)$. S_Σ the external heat load, σ the electric conductivity, J_x an electric current in the target B_z the toroidal magnetic field and u_m the melt front velocity. The external heat source S_Σ is corrected by the black body radiation from the surface as $S_\Sigma = S_\Sigma^{(o)} - 0,1T^4$.

The melt front velocity u_m according to eq (4) is determined from the difference between the heat load S_+ to the melt front and that of the heat load S_- into the bulk target. S_+ is given according to

$$S_+ = \kappa_l \frac{\partial T}{\partial x} \Big|_{x=-H+o} = \kappa_l T_o' \quad (20)$$

with T_o' the derivative at the melt front given as $T_o' = 3\frac{T}{X} - \frac{S_\Sigma}{2\kappa}$

For S_- the heat load into the bulk target, an analytical expression is used corresponding to the self similar solution of the thermal conductivity equation inside of the target with fixed boundary temperatures $T_{x=0} = 0$ and $T_{x=-\infty} = T_{room}$ and initial temperature $T_{t=0} = T_{room}$ at $-\infty \leq x \leq 0$ [28] with T_{melt} the origin of the temperature scale. S_- is given as

$$S_- = T_{room} \sqrt{\frac{\kappa_s \rho c_s}{\pi t}} \quad (21)$$

Eqs (15-17) are one-dim hydrodynamics equations with effective density ρX . The terms on the right hand side (RHS) of eq (16) provide acceleration of the fluid along $x=0$ due to pressure gradient, gravity, gradient of surface tension, viscose friction and Lorentz force. According to eq (17) the fluid is heated by the external heat load S_Σ , by the viscous heating caused by fluid motion, by the gradient of the surface tension and by Joule heating. Cooling of the fluid is by the thermal flux into the solid target.

11.2 JEBIS electron beam simulation experiments

Experimental results from the JEBIS e-beam facility on melt layer erosion of tungsten targets demonstrate a rather pronounced motion in the melt layer. As a result the erosion depth on average was about 150 microns and mountains of ejected melt material are formed at the crater edge [6]. Due to the melt motion the melt layer erosion was a factor of 2 larger than the melt layer thickness. For a quantification of melt layer erosion therefore cause and consequences of melt motion has to be investigated.

In order to validate the developed 1-D fluid dynamics model of melt motion the JEBIS results for tungsten were simulated. Gaussian profiles for the spatial and time distribution of the heat load were used. The calculated erosion profile is shown in Fig. 65 after complete resolidification which needs about 1,5 ms. The crater depth is 30 microns, the thickness of the resolidified layer is 60 μm . A mountain is formed at the crater edge. However the numerical results differ significantly from the experimental ones. Variations of such parameters as viscosity and pressure of saturated vapor only weakly are influencing the depth of the erosion crater. For example decreasing the viscosity by a factor of 2 resulted in an increase of the depth of not more than 30%. For the e-beam facility typical electric currents of densities up to 3 A/cm² contribute negligible to Joule heating. Lorentz forces because of no external magnetic field are absent. Droplet splashing from the melt produces momentum which results in additional pressure acting on the melt. This effect was estimated too by assuming that 10% of the melt is splashed by droplets. Negligible influence on melt motion was obtained.

11.3 Tokamak conditions

A first application of numerical simulation of melt motion was done for hot plasma impact onto a vertical tungsten target. A typical ITER-FEAT condition with peak power density of 3 GW/m² and time duration of 3 ms was used. Time dependent target heat loads and plasma shield pressures obtained from FOREV-2 calculations were used. The target heat loads are shown in Fig. 66. The pressure of the plasma shield is typically up to 2 bar. The pressure

profiles are similar to the heat load profiles shown in Fig. 66. During irradiation the temperature of the molten material reaches boiling temperature and thus a significant amount of energy is accumulated in the melt layer. During the load time melt motion is only weakly developed with a maximum surface roughness of 60 microns. The depth of the melt layer is about 210 microns as is to be seen from Fig. 67a, showing the melt layer just at the end of the heating. In Fig. 67b the calculated erosion profile after resolidification which starts at the bottom of the melt and which needs 18 ms is shown. The weak melt motion which is going on till complete resolidification produces a significant roughness at the melted region and causes melt layer erosion with typically 150 microns. The influence of electric currents crossing the melt layer perpendicularly to the target surface was estimated. A typical target current of 1 kA/cm² in a magnetic field of 5 T parallel to the target surface was assumed. The depth of the melt layer is not influenced by Joule heating, but the Lorentz force reverses the flow direction thus shifts the mountains to the left, increases the melt motion, and increases the melt layer erosion up to about 200 microns as is seen from Fig. 67c. Melt motion results in melt layer erosion which is comparable to the melt layer thickness calculated without melt motion. The resolidification time drops due to increased melt motion down to 13 ms.

In the case of RAE impact eddy currents add to the Lorentz force if the current quench time remains below 100 ms [30] and if the eddy currents are produced well within 20 ms after the RAE impact because of resolidification of the melt. The Lorentz force exists for a longer time period and thus increases melt motion and melt layer erosion further.

11.4 Melt layer thickness in typical off normal events without melt motion

As first step for damage analysis of metal walls the melt layer thickness due to realistic heat loads was calculated for the different off normal events as listed in Table 1. The 2-D heat conduction equation as given in eq (1) was used.

11.4.1 Disruptions

For ITER-FEAT disruptions the effective target heat loads at vertical tungsten targets calculated with FOREV-2 are shown in Figs. 66 and 68 for 3 and 30 GW/m² for the case with separatrix downstream. For the low power density case up to now heat loads are available up to 3 ms. The upstream shift of the heat load for the case with 30 Gw/m² is clearly to be seen. This upstream shift results in a widening of the width of the melt layer up to 50 cm as is to be seen from Fig. 69. The typical thickness of the melt layer is about 130 microns after 1 ms. For the case with 3 Gw/m² the width of the melt layer remains below 20 cm, the maximum melt layer thickness after 3 ms achieves values of around 160 microns as is to be seen from Fig. 70. Due to the rather long deposition time removal of the melt layer by melt motion if occurring might drastically enhance these values. A detailed analysis still needs to be performed. Figs. 71 and 72 show the surface temperature for the two cases with peak power densities of 30 and 3 GW/m².

Reradiation from the plasma shield preferentially hits the inner side wall made from tungsten [15]. Whether melting occurs under such heat loads was investigated. The radiative heat load at the inner side wall is shown in Figs. 73 and 74 for graphite and tungsten plasma shields for the two different target heat loads 3 and 30 GW/m². The reradiation fluxes from

carbon and tungsten plasma shields at a target heat load of 30 GW/m² are comparable as is to be seen from Figs. 73 and 74. For 3 GW/m² the reradiated flux from carbon plasma shields is larger than from tungsten plasma shields. However the results for tungsten are preliminary. The adequacy of Rosseland averaging is not evaluated up to now. The evolution of the surface temperature of the tungsten side wall is shown in Figs. 75 for reradiation from a plasma shield of a tungsten vertical target and in Fig. 76 for reradiation from a plasma shield of a graphite vertical target for a heat load of 30 GW/m² in both cases. Melting of the tungsten inner side wall starts after 0,4 ms for the reradiation from the tungsten plasma shield on front of the tungsten vertical target and after 0,16 ms for the graphite case. Typical melt layer profiles are shown in Figs. 77 and 78 for the cases of the vertical target heat load of 30 GW/m² for a tungsten (Fig. 77) and a graphite (Fig. 78) vertical target. Melting of the tungsten inner side wall does not occur for the 3 GW/m² case within the time period up to 3,1 ms.

11.4.2 Run away electrons (RAEs)

Here it was assumed that the energy density deposited onto the First Wall (FW) reaches up to 50 MJ/m² per event. The impact energy of the RAE's was assumed to be up to 15 MeV, the impact angle 1°. As FW materials beryllium and tungsten were assumed. The volumetric energy deposition was calculated by Monte Carlo [23]. Vapor shielding by the evaporated target material was taken into account assuming that the evaporated mass can be taken into account as a layer in which a part of the energy of the RAE's is lost in accordance with the energy deposition function calculated for the solid material. The energy deposition inside of the target with vapor shielding $F'(x)$ is calculated according to

$$F'(x) = F(x + m_v(t) / \rho) \quad (22)$$

with $m_v(t)$ the mass of the vapor at the time moment t , $F(x)$ the initial energy deposition function as calculated by Monte Carlo [23], ρ the density of the target material, and x the coordinate counted from the surface into the target. The calculated energy deposition for the RAEs of different impact angles is shown in Fig. 79. Temperature dependent thermophysical data were taken from [17]. Results for tungsten are shown in Figs 80-82 with evolution of the surface temperature, depth of the evaporated layer and thickness of the melt layer which amounts up to 1050 microns. Results for beryllium are shown in Figs. 83-85 showing the same quantities time evolution of surface temperature, depth of evaporated layer and thickness of the melt layer which for beryllium amounts up to 1,9 mm. For beryllium and with 2,5 GW/m² volumetric boiling occurs after 16 ms at a depth of 500 μ m. As a consequence melt splashing with droplets might occur. In Fig. 85 the two cases complete removal of the melt layer by droplet splashing up to the depth where volumetric boiling occurs (dashed curve for 2,5 GW/m²) and the negligible melt splashing by droplets is shown. However melt motion occurs also and starts earlier. A consistent modelling is required. The results on calculated evaporation and melt layer thickness are listed in Table 3 for the two FW materials tungsten and beryllium. Melt layer erosion by melt motion is not included in this case. Melt layer erosion can become up to a factor of 3 larger than the melt layer thicknesses given in Table 3.

11.4.3 Vertical displacement events (VDEs)

For VDEs it is assumed that the energy density deposited to the FW by the hot plasma is up to 50 MJ/m² per event. The maximum impact energy of the hot plasma is assumed to be 1 keV. Ions and electrons are assumed to contribute the same amount of energy. The existence of a vapor shield which would reduce the target heat load and which also would influence the impurity production has to be investigated. For demonstration of the consequences of a vapor shield the two cases without and with target shielding were considered. The stagnation pressure of the impacting hot plasma was taken into account. The 2-D heat conductivity equation as described in chapter 2.1 was solved and the nonsteady state model of surface evaporation as described in chapter 2.1 was solved and the nonsteady state model of surface evaporation as described in appendix A1 was used. For the case with target shielding the vapor shield effect was taken into account by the following way: from FOREV-2 results the effective target heat load given by direct energy deposition and radiation as function of the plasma shield mass is known for target heat loads above 1 GW/m². For target heat loads between 0,1 and 0,5 GW/m² the effective target heat load was obtained by linear extrapolation using a logarithmic scale for the initial target heat load. Results in evaporation and melt layer thickness are listed in Table 4. The melt layer thickness only weakly is influenced by target shielding. However evaporation sensitively depends on the existence of a vapor shield. The consequences of this are discussed below.

Fig. 86 shows a comparison of the time evolution of the surface temperature of beryllium for 3 different cases. Without target shielding the surface temperature for beryllium during a time interval of about 90 ms gets about 2500 K. This is below the boiling temperature of Be but due to the temperature dependence of the saturation pressure evaporation occurs resulting in an evaporated layer thickness of 500 microns. The thickness of the evaporated layer in each case is indicated at the curves of Fig. 86. Fig. 87 shows a comparison of the evolution of the vapor density in front of the FW for the same 3 cases. Assuming no target shielding then vapor densities above 10^{17} cm³ are occurring beyond the Knudsen layer. Such densities within a layer thickness of less than 0,5 cm are sufficient to absorb the impacting energy and thus are providing sufficient mass for an efficient target shielding. Therefore the assumption of no target shielding is not realistic and target shielding is occurring in any case. In the case with target shielding there is no continuous evaporation but consecutive cycles of evaporation and stop of evaporation because of improved target shielding. This oscillating behavior is not shown in the plot of the vapor density. The third case shown in Figs. 86 and 87 and labeled as modified shielding should come more close to the reality. In this case it is assumed that the plasma shield shields the target only between 0,1 and 1 ms then the plasma shield is removed by plasma turbulence and this process starts again with formation and removal of the vapor shield.

Assuming a few microns as a realistic erosion during a hot plasma VDE event could result in a drastic impurity influx into the central plasma. Additionally there is melt motion in the melt causing considerable surface roughness and droplet-splashing resulting in enhanced impurity production thus still increasing the core plasma dilution. For evaluating the impurity production the influence of the self regulating process of evaporation and target screening has to be modeled consistently. A realistic modelling of such events requires a two fluid MHD

description because hydrogen accumulation in the vapor shield could change the shielding properties considerably.

12 Numerical simulation of brittle destruction

For volumetric heating brittle destruction dominates erosion and produces considerable amounts of dust [4]. There are experimental indications that under hot plasma impact brittle destruction might also occur [31]. Brittle destruction of CBMs when occurring could become a limiting factor for the lifetime of graphite divertor targets because predamage of the sample under volumetric heating and under cyclic surface heat loads finally might result in a drastic increase of divertor plate erosion. For understanding of brittle destruction and its quantification for ITER-FEAT off normal conditions a numerical simulation model is developed. It was shown previously that thermal stress in a heated graphite sample results in breaking of lattice bonds due to anisotropy of thermal expansion and thermal conductivity [32]. As a consequence of intense cracking macroscopic layers are destroyed and graphite dust is produced [4]. Important for brittle destruction to occur are the anisotropy of the graphite grains, the failure stress distribution of the bonds connecting adjacent grains and the temperature and its gradient in the bulk target. Cracks preferentially are propagating into the depth of the sample. Such a crack propagation indicates occurrence of predamage under repetitive heat loading and finally might result in drastically enhanced erosion of graphite [3]. This could reduce the lifetime and by dust formation could cause a safety problem.

The analysis of brittle destruction is mandatory for a damage evaluation of graphite. First numerical results of a 2-D analysis of brittle destruction of graphite under hot plasma and hot electron impact and target screening by dust particles are presented. Predamage of the sample and enhancement of brittle destruction under cyclic heat loads are discussed.

12.1 Lattice model of graphite

For numerical simulation of brittle destruction a lattice model was developed simulating real graphite which consists of grains of different size and different anisotropy directions. The numerical lattice model uses a special procedure which generates grains of random size and shape in a rectangular coordinate system. A typical numerical lattice is shown in Fig. 88. It consists of cubic cells of identical size a . Grains consist of an integer number of cells. The grain sizes are Gaussian distributed around a mean number of cells per grain - mean grain size (MGS). Neighbouring cells of the same grain are connected via internal bonds, neighbouring grains via surface bonds. Each bond (ij) has its individual failure stress value σ_{ij} . The mean failure stress value of the internal bonds is assumed to be a factor of 10 larger than the mean value for the surface bonds. Therefore breaking of bonds preferentially will occur along the surface of the grains. In Fig. 88 for better illustration of the grains, cell sizes are drastically increased. The sample is turned by 45° relative to the direction of the incoming flux because heat fluxes parallel to cell boundaries correspond to a highly degenerated arrangement of the sample and never correspond to the real situation. Additionally there are small grains filling the gaps between the larger ones.

The anisotropy of the physical properties of the grains determined by the atomic structure of graphite is taken into account. The Young's moduli E_1 and E_2 , the thermal conductivities λ_1 and λ_2 and the thermal expansion coefficients α_1 and α_2 are assumed to be different parallel and perpendicular to the anisotropy axis which denotes the direction perpendicular to the atomic carbon layers as is seen from Table 5.

It is assumed that the individual failure stress values for the surface bonds are uniformly distributed in the interval $\sigma_{0s} \cdot (0.5, 1)$ and are sampled by use of a random number generator. For adjacent cells belonging to different grains there are 3 possible anisotropy axes directions: parallel or perpendicular to the bond connecting both cells and parallel for one and perpendicular for the adjacent cell (last column of Table 5b).

In case of broken bonds the expansion of the cells during heating can result in stretching (increasing distance between broken bonds) or in compression (closure of gap). For the latter situation the conditions of Table 5b are assumed to be valid, for the former Young's modulus and thermal conductivity is assumed to be zero.

12.2 Numerical model of brittle destruction

Heating of a graphite sample results in local temperature changes thus producing forces acting on the grains due to thermal expansion. Nevertheless, the sample is at rest during heating. In the 2-D numerical lattice model, heating results in 8 different forces acting on each individual cell as shown schematically in Fig. 89 and as described in the appendix A3. Using these forces the evolution of the lattice is calculated with ongoing temperature changes. It is assumed that the relaxation of the stress occurs much faster than the propagation of the heat wave. Therefore after each change of temperature the mechanical equilibrium of the lattice system is assumed to be established instantaneously.

The temperature distribution in the grain system can be described by means of a discrete analogue of the thermal conductivity equation

$$\frac{dT_i}{dt} = \sum_j v_{ij} (T_j - T_i) + \omega_i \quad v_{ij} = \frac{\lambda_{ij}}{\rho c a^2} \quad \omega_i = \frac{w_i}{\rho c} \quad (23)$$

with T_i the temperature at the centre of the i -th cubic cell, ρ the density, c the specific heat capacity, a the size of the cells, λ_{ij} the effective thermal conductivity of the bond connecting the i -th and the j -th cell of the rectangular lattice and w_i the heating power within the i -th cell. The sum of j means summation over all neighbouring cells in x and y directions. The values λ_{ij} used are listed in Table 5. The elastic properties of the sample are described by means of a Born type Hamiltonian [33,34] which takes into account both normal and shear stresses

$$H = \sum_{i,j} h_{ij} = \sum_{i,j} h_{ij}^{(x)} + h_{ij}^{(y)}, \quad (24)$$

with h_{ij} the interaction energy density for a pair of adjacent cells. In the 2 directions x and y of a 2-D lattice h_{ij} is given according to

$$\begin{aligned} h_{ij}^{(x)} &= \frac{E_{ij}a}{2} (x_j - x_i - a\alpha_{ij}\Delta T_{ij})^2 + \frac{G_{ij}a}{2} (y_j - y_i)^2 \\ h_{ij}^{(y)} &= \frac{E_{ij}a}{2} (y_j - y_i - a\alpha_{ij}\Delta T_{ij})^2 + \frac{G_{ij}a}{2} (x_j - x_i)^2 \end{aligned} \quad (25)$$

with $(x_i, y_i) = \mathbf{r}_i$ the displacement vector of the cell centres, E_{ij} the Young's modulus, $G_{ij} = E_{ij}/2(1+\mu)$ the shear modulus with $\mu = 0.33$ for all cells, α_{ij} the effective linear expansion coefficient describing the adjacent cells i and j and $\Delta T_{ij} = (T_i + T_j)/2 - T_0$ the difference of the average temperature of adjacent cells and the initial temperature T_0 . Again as with the effective thermal conductivity λ_{ij} the quantities E_{ij} , σ_{ij} and α_{ij} are defined according to the different possible directions of the anisotropy axes as listed in Table 5. The mechanical equilibrium of the system is calculated using a set of auxiliary equations

$$\frac{d\mathbf{r}_i}{dt} = \mathbf{F}_i = -\frac{\partial H}{\partial \mathbf{r}_i} \quad (26)$$

with \mathbf{F}_i the total force acting on the i -th cell. Eq. (26) is solved iteratively until the total force acting on each cell is close to zero $\mathbf{F}_i \approx 0$. Despite this the stresses of the surface bonds can remain rather large – of the order of $F \sim (\alpha_1 - \alpha_2)a^{-1}E_1(T - T_0)$ due to the anisotropy of the grains. To simulate brittle destruction of the grain system due to these thermal stresses the following stress-failure criterion for a bond (ij) is used.

$$\left| \frac{\partial h_{ij}}{\partial x_i} \right| + \left| \frac{\partial h_{ij}}{\partial y_i} \right| \geq \sigma_{ij} E_{ij} a^2. \quad (27)$$

According to eq. (27) a bond is assumed to be broken if the combination of normal and shear thermal stresses (left-hand side of eq (27)) exceeds a value specified for this bond. This condition is checked after each time step and the bonds for which it is fulfilled are disrupted.

A broken bond represents an elementary crack. The model takes into account that the mechanical properties depend on the crack density and are, thus, time-dependent. Merging of the neighbouring cracks simulates crack propagation. Furthermore, due to merging of cracks at various places, different clusters of grains are formed within the sample. Isolated clusters at the surface are removed as dust particles. This process simulates the motion of the fracture boundary inside of the sample.

12.3 Crack generation during uniform heating

Using the lattice model crack generation in the sample was calculated for uniform heating. The system of equations to be solved is described in the Appendix and is not repeated here. Results of the numerical simulation are shown in Fig. 90. Plotted is the normalised crack density n defined as the ratio of the number of broken surface bonds in the sample to the

total number of surface bonds as function of the bulk temperature for different failure stress values σ_{0s} of the surface bonds and for two different lattices with the same mean grain size but different numbers of cells per grain. The crack density during uniform heating depends only weakly on the number of cells per grain and is independent from the cell size. A dependence on the mean grain size is only due to non-uniform heating.

Simulating stretching of a graphite sample, destruction was obtained when about 30–50% of all surface bonds were cracked. Thus it is reasonable to assume that the sample is destroyed when up to about one half of the surface bonds are broken (critical density). From Fig. 90 it is seen that there is a certain threshold temperature T_{br} for onset of cracking. T_{br} depends on the failure stress value, on the value of Young's modulus and on the thermal expansion coefficient.

After onset of cracking the normalised crack density n_c increases with temperature and for $T > T_{br} + T_f$ becomes constant. Analytically the temperature dependence of the crack density n can be approximated in the following manner

$$n = \begin{cases} 0 & T < T_{br} \\ n_c (T - T_{br}) / T_f & T_{br} < T < T_{br} + T_f \\ n_c & T > T_{br} + T_f \end{cases} \quad (28)$$

with T_f the temperature interval in which n changes from 0 to n_c and m an empirical exponent between 1 and 2. Real splitting off of grains occurs at $n_{sp} < n_c$ and therefore occurs at some intermediate temperature T_{sp} with $T_{br} \leq T_{sp} \leq T_{br} + T_f$.

13 Estimation of the characteristic failure stress value σ_{0s}

For a numerical simulation of brittle destruction the failure stress value σ_{0s} has to be known. However this parameter can't be measured. Therefore it is estimated from a comparison of numerical results with experimental results on destruction of the sample by mechanical compression and onset of brittle destruction by volumetric heating.

13.1 Mechanical compression test

From compression experiments of graphite it is known that graphite is destroyed when compressing the sample to approximately 99% of its initial thickness [35]. Uniform compression of a graphite sample might result in production of large cracks but not in a full destruction of the sample. Therefore the numerical simulation of the compression might result in an underestimation of the σ_{0s} value. For the numerical simulation one surface of the sample was fixed in the direction perpendicular to the sample surface, the cells forming the other surface were incrementally shifted into the sample in steps of $\varepsilon L/N$ with $\varepsilon = \Delta L/L$ the final compression factor, N is the number of the compression steps, L is the sample thickness. The resulting forces cause shifting of the interior cells and breaking of surface bonds. The procedure was repeated till 80% of the surface bonds were broken.

The results obtained are shown in Fig. 91 for a mean grain size consisting of 3 cells of size $a = 1 \mu\text{m}$. The critical density $n_c = 0.3 \div 0.5$ is reached at different relative deformations of the sample depending on the failure stress of the surface bonds σ_{0s} . For obtaining a fracture deformation in the range of about 1% the failure stress for surface bonds was obtained to be in the range $\sigma_{0s} = (0.5-1) \cdot 10^{-2}$. According to Fig. 90 this corresponds to a characteristic temperature of the sample of the order of $T_{br} \sim 3000-4000 \text{ K}$, assuming the value $\alpha_1 = 3 \cdot 10^{-6}$ for the thermal expansion coefficient of the graphite grain. Fig. 92 shows the influence of the mean grain size on the intensity of crack formation. 3 different mean grain sizes with 3, 12 and 26 cells were used. The cell size is $1 \mu\text{m}$ for the mean grain with 3 and 26 cells and $0,4 \mu\text{m}$ for the mean grain with 12 cells. The threshold character of the destruction process depends only weakly on the mean grain size.

13.2 Volumetric energy deposition

Volumetric heating results in a clear and complete destruction of the sample. Therefore experimental results on brittle destruction by volumetric heating were used additionally for a determination of the failure stress value σ_{0s} . Results of the numerical simulation for the electron beam facility GOL-3 are shown in Fig. 93 for $\sigma_{0s} = 0.005$. The energy spectrum of the electron beam impacting perpendicular into the target was taken from [4]. The corresponding volumetric heat load used for the numerical simulation was calculated by Monte Carlo [23]. Onset of brittle destruction occurs at about 10 MJ/m^2 in agreement with the experimental results obtained at the GOL-3 facility [22]. At 14 MJ/m^2 the average experimental value is about 70 microns. The numerical simulation with a failure stress value of $\sigma_{0s} = 0.005$ is in rather close agreement as is seen from Fig. 93. For a typical power density for RAEs Fig. 94 shows calculated typical crack patterns and crack propagation into the bulk target with ongoing time. Volumetric heating initially results in crack formation inside of the bulk target. The brittle destruction front propagates along the predamaged path. Applying a cyclic heat load to such a predamaged sample might result in enhancement of erosion by brittle destruction.

The numerical simulation model was tested for near surface heat loads typical for the electron beam facility JEBIS with perpendicular impact of 70 keV electrons [24]. It is assumed that initially the graphite sample is at a uniform temperature of 1200 K. Heating of the surface near target layer occurs due to a constant heat flux of 1.8 GW/m^2 for 2 ms. The energy deposition into graphite shows a maximum at a depth of 20 microns. A comparison of calculated erosion rates by brittle destruction using numerical simulation and results from another analysis in which a damage threshold value of 10 kJ/g was used for start of brittle destruction [22] is shown in Fig. 95. Crack formation and propagation of brittle destruction are rather similar to that one shown in Fig. 94 for run away electrons.

14 Conclusions

Shielding of divertor materials by their own vapour occurs during ITER-FEAT plasma disruptions and ELMs. To predict erosion by evaporation of the ITER-FEAT vertical targets a 2-D radiation magneto-hydrodynamic (R-MHD) code is necessary not only because of the rather complicated divertor geometry, the reradiation from a plasma shield to the side walls and other nearby components, the finite width of the impacting hot SOL plasma and its charac-

teric power density profile across the SOL width, but also because of the 2-D MHD behaviour of the plasma shield and its influence on target erosion. The newly developed 2-D R-MHD code FOREV-2 uses a 2-D scheme for anisotropic radiation transport, a 2 1/2-D MHD model and a solution of the magnetic field equations in the plasma shield for all three components of the magnetic field.

Disruption simulation experiments performed at the plasma gun facilities at TRINITI Troitsk were used for code validation of FOREV-2 and for investigations of the MHD of typical plasma shields. The 2-D numerical analysis of the disruption simulation experiments allows to conclude that such experiments adequately simulate the tokamak plasma shield properties and its dynamics. Target erosion in the simulation experiments is caused by radiative target heat loads. The agreement between calculated and measured erosion for graphite demonstrates the adequacy of the calculated 2-D radiative target heat loads when using multigroup Planck opacities. The use of multigroup Planck opacities with an adequate frequency group structure for a resolution of individual lines and for line radiation transport is necessary. Only inclusion of line radiation allows to get a realistic radiation cooling of the carbon plasma shield after switching off the heating. For a realistic calculation of reradiation from plasma shields anisotropic radiation transport has to be used and line radiation has to be included.

The numerical results on local temperature and density values in a carbon shield plasma and the data measured by Thomson scattering in the plasma shield close to the target are in agreement. This demonstrates that the dynamics of the cold dense plasma layer close to the target is adequately described by FOREV-2 for the whole time duration of the pulsed heat load which is up to 50 μ s.

The experimentally observed downstream drift of the carbon plasma shield along the surface of a vertical graphite target downstream of the SSP can be explained by the lateral motion of the cold dense plasma layer close to the target. This motion is driven by lateral gradients of the pressure of the plasma shield which change the geometry of the external magnetic field. The guiding magnetic field with 2T in the simulation experiments is depleted at the separatrix (pushed out). In the case of an electrically conducting target a lateral (y) component of magnetic field appears. Both magnetic field components via the momentum equation are influencing the lateral MHD motion of the cold dense part of the plasma shield. The observed upstream shift of the erosion profiles of vertical targets in the simulation experiments can be explained by reradiation from the expanding plasma shield. The radiative target heat load along the target surface shows a maximum always upstream of the SSP. With upstream expansion of the cold dense plasma the maximum of the radiative target heat load also moves upstream and thus the erosion profile too.

The experimental plasma shields are two temperature plasmas with a cold dense plasma layer close to the target and a low dense hot plasma corona. The MHD behavior and the stability of the cold and dense part of the tokamak plasma shields which determines the target erosion can be adequately modeled by FOREV-2 by use of the classical magnetic field diffusion coefficient. Turbulence of the hot low dense part of the tokamak plasma shields does not influence the MHD behavior of the cold dense plasma layer and thus is not influencing the target erosion. The dynamics of the cold plasma is determined by the gradient of the pressure of the plasma shield and the diamagnetic effect of the cold plasma itself. Thus

the extensive validation exercise of FOREV-2 against disruption simulation experiments gives confidence that the numerical analysis of erosion for the ITER-FEAT vertical targets to be performed with FOREV-2 is based on sound principles and covers all important effects for modelling of plasma shield behavior and plasma shield stability.

A realistic damage evaluation for vertical targets for disruptions and ELMs with energy densities up to 30 MJ/m² has been done. Similar to the results from the simulation experiments the erosion profiles of vertical targets are shifted upstream with respect to the SSP. This is due to the upstream shift of the reradiation from the expanding plasma shield. In high power density off-normal events this reradiation is intense enough to evaporate target material up to 50 cm upstream of the SSP. The plasma shield effectively shields the target and dissipates the incoming energy. Peak erosion per event remains below 1 micron for tungsten but becomes at least a factor of 10 larger for graphite. Vertical targets in comparison with horizontal ones offer clear advantages. The peak erosion is reduced at least by a factor of 5. In low power density off-normal events the reradiation is only intense enough to evaporate target material to upstream distances from the SSP up to 10 cm. The peak target erosion is comparable to the erosion for the high power density events and becomes comparable to that one for horizontal targets. First Investigations on existence and consequences of vapor shields at target heat loads of typically up to 0,5 GW/m² (VDEs) and evaluation of target damage for such cases have been done. VDEs at metallic FWs have the potential to produce a considerable amount of impurities and by melt motion a drastic increase of melt layer erosion and surface roughness. A consistent modeling has still to be done based on a two fluid approach with evaporated target material as fluid no. 1 and impacting hydrogen as fluid no. 2.

Erosion of carbon based materials (CBMs) is due to vaporization and brittle destruction. Thermal stress in heated graphite sample results in breaking of lattice bonds due to the anisotropy of the thermal expansion and the thermal conductivity. As a consequence of intense cracking macroscopic layers are destroyed and graphite dust is produced. For volumetric heating brittle destruction dominates erosion and produces a considerable amount of dust. There are experimental indications that under hot plasma impact brittle destruction might also occur. Brittle destruction of CBMs when occurring could become a limiting factor for the lifetime of graphite vertical targets. For understanding of brittle destruction and its quantification for ITER-FEAT off normal conditions a 2-D numerical simulation model was developed. By comparing the numerical results on brittle destruction with experimental results for volumetric heating and with results from mechanical destruction tests of graphite samples a typical failure stress value for surface bonds of $\sigma_{0s}=0.005$ was derived. First numerical results of brittle destruction of graphite under hot plasma and hot electron impact and target screening by dust particles were obtained. Volumetric heating produces cracks inside of the sample, surface heating results in crack propagation into the depth of the sample. In both cases some predamage of the sample occurs. Enhancement of brittle destruction under cyclic heat loads thus can't be excluded.

Melt layer erosion of metals is dominated by melt flow. The driving force behind the melt flow was investigated. Lorentz forces due to currents flowing in the target during the heat load period might trigger a pronounced melt motion which might sweep away a considerable part of the melt layer. The melt layer erosion thus can be comparable or even larger than the melt thickness formed during the heat load period. In the case of RAE impact eddy currents add

to the Lorentz force if the current quench time remains below 100 ms [30] and if the eddy currents are produced well within 20 ms after RAE impact because of resolidification of the melt. The Lorentz force exists for a longer time period and thus increases melt motion and melt layer erosion further. For RAE impact melt layer erosion can become up to a factor of 3 larger than the melt layer thickness. For RAE impact erosion of tungsten FWs can thus be up to 3 mm, for Be up to 5 mm. Due to the large damage for RAEs it is mandatory to limit the tolerable RAE energy density to values below 15 MJ/m^2 . Due to the considerable implications of melt motion on melt layer erosion more experimental and theoretical investigations on this topic are urgently required both for surface and volumetric heating.

Melt layer erosion always is accompanied by splashing. Up to 20% of the eroded mass is splashed away by droplets. Flaking from redeposited layers, dust, melt flow and droplet splashing during disruptions produce complex layers with considerable surface roughness and drastically changed thermophysical properties. The hot spots of such layers are responsible for enhanced impurity production. A characterization of such layers is urgently required. First numerical estimations show that the maximum tolerable ELM energy is noticeably lower for redeposited layers with considerable surface roughness than for the virgin vertical target and that the ELM energy has to be reduced to values below 4 MJ for vertical targets.

15 References

- [1] G. Federici et al., In vessel tritium retention and removal in ITER, J. Nucl. Mater 266-269, 1999, 14.
- [2] J. Roth, Chemical erosion of carbon based materials in fusion devices, J. Nucl. Mater 266-269, 1999, 51.
- [3] S. Pestchanyi, H. Würz, Brittle destruction of carbon based materials under off-normal ITER-FEAT conditions, submitted to Physica Scripta.
- [4] H. Würz et al., Dust production in ITER-FEAT off normal events and target screening by dust particles, EPS-27, June 2000, Budapest.
- [5] K. Krieger et al., Conclusions about the use of tungsten in the divertor of ASEDEX Upgrade, J. Nucl. Mater 266-269, 1999, 207.
- [6] K. Nakamura et al., Disruption erosion of various kinds of tungsten, Fus. Eng. and Design 39-40, 1998, 295-310.
- [7] H. Würz et al., Vertical target and FW erosion during off normal events and impurity production and transport during ELMs typical for ITER-FEAT, presented at PSI-14, May 22-26, 2000, Rosenheim; submitted to J. Nucl. Mater.
- [8] G. Tsotridis, Modelling of surface deformations during plasma disruptions, Fus. Technology 37, 2000, 185.

- [9] I. Landman, H. Würz, 1-D fluiddynamic simulation of melt motion, FZKA report 6517, in preparation.
- [10] N.I. Arkhipov et al., Fusion Technology 1996, Vol. 1, 1997, 507.
- [11] H. Würz et al., Fusion Technology 32, 1997, 45.
- [12] H. Würz et al., Fusion Technology, 1996, Vol 1, 1997, 191.
- [13] S. Pestchanyi et al., Proc. 24th European Conf. Controlled Fusion and Plasma Physics, Berchtesgaden, June 9-13, 1997, Vol 21 A, Part III, 981.
- [14] H. Würz, et al. Fusion Technology 30, 1996, 739.
- [15] H. Würz et al., Report FZKA-6198, March 1999.
- [16] A.A. Samarski, E.S. Nicolaev, Numerical methods for grid equations Vol 2. Birkhäuser Verlag, Basel, 1980.
- [17] R. Hultgren, Selected Values of Thermodynamic Properties of the Elements American Society for Metals Park, Ohio, 1973.
- [18] S.I. Anisimov et al., The Action of High Power Radiation of Metals, Nauka, Moscow, 1970.
- [19] S.I. Anisimov, A.Kh., Rakhmatulina, Sov. Phys., JETP, Vol. 37, 1973.
- [20] N.I. Arkhipov et al., Proc. 26th EPS Conf. Maastricht, June 14-18, 1999.
- [21] B.J.D. Tubbing et al., 22nd EPS Bournemouth, Vol., 19C, Part III, 1995.
- [22] V.T. Astrelin et al., Nucl. Fusion, Vol. 37, No. 11, 1997, 1541.
- [23] G. Miloshesvski, H. Würz, FZKA report 6482, 2000.
- [24] K. Nakamura et al., J. Nucl. Mater, 212-215, 1994, 1201.
- [25] A. Lodato et al., to be published in Fus. Eng. and Design.
- [26] V.N. Litunovsky et al., Fus. Eng. and Design 30-40, 1998, 303.
- [27] N.I. Arkhipov et al., Fusion Technology 1994, Vo. 1, 463, 1995.
- [28] L.D. Landau, E.N. Lifshits, Hydrodynamics Moscow Nauka, 1986 (in Russian)
- [29] V.V. Semak et al., J. Phys. D. Appl. Phys. 32, 1999, 1819.

- [30] M. Hashizuma et al., Fus. Eng. and Design 9, 1989, 219.
- [31] M. Guseva et al., Tech. Phys. 41, 578, 1966.
- [32] S. Pestchanyi et al., Fusion Technology, 1998, Vol. 1, 275, 1998.
- [33] G.N. Hassold, D.J. Srolovitz, Phys. Rev. B 39, 9273, 1989.
- [34] J. Astrom et al., Phys. Rev. E 55, 4757, 1999.
- [35] Gmelin, Handbuch der anorganischen Chemie Kohlenstoff, Teil B Verlag Chemie Weinsheim, 1967.
- [36] C.H. Wu et al., J. Nucl. Mater, 258-263, 1998, 782.

Table 1: Off normal events used for damage analysis and impurity production at vertical targets and First Walls (FW) in ITER-FEAT

Type of event	location	energy density (MJ/m ²)	time duration (ms)	target heat load used in analysis		impact energy (keV)	type of particles
				GW/m ²	(ms)		
thermal disruption	Vertical target	30	≤ 10	30 3	1 10	10	hot plasma
ELMS	Vertical target	0.5	≤ 1.0	1	0.5	3	hot plasma
RAEs	FW	50	≤ 50	0.5-2.5	20-100	up to 20 MeV	electrons
VDE	FW	50	100	0.5	100	≤ 3 keV	hot plasma

Table 2: Comparison of measured and calculated erosion for perpendicular and tilted graphite and quartz targets for the two different plasma gun facility MK-200 UG.

Target material	Target arrangement	Erosion (μm)		Number of meshes	Mesh size close to target (xy) mm ²
		Measured	calculated		
Graphite	perp.	0.4	0.45	60 x 80	2 x 2
quartz	perp.	1.0 - 1.3	1.3	60 x 80	2 x 2
Graphite	tilted	0.20	0.7	100 x 40	5 x 5
			0,35	200 x 100	2 x 2
Quartz	tilted	0.55	1.5	100 x 40	5 x 5
			0,65	200 x 100	2 x 2

Table 3: Calculated evaporation and melt layer thickness of Tungsten and Beryllium for RAEs of impact energy of 15 MeV and impact angle 1 ° without melt motion. Vapor shielding for RAEs is taken into account. Initial temperature of FW is 400 K.

impacting particles	power density in beam (GW/m ²)	time duration (ms)	thickness (μm)			
			Tungsten		Beryllium	
			melted	evaporated	melted	evaporated
RAEs	0.5	100	1230	15	1900	100
	1.0	50	1220	30	1850	100
	2.5	20	1150	280	1700(*)	50

(*) volumetric boiling occurs after 16 ms at a depth of 500 μm

Table 4: Calculated evaporation and melt layer thickness of Tungsten and Beryllium FWs for VDE events with 50 MJ/m². Initial temperature of FW is 400 K.

impacting particles	power density in beam (GW/m ²)	time duration (ms)	thickness (μm)				
			Tungsten		Beryllium		
			melted	evaporated	melted	evaporated	
hot plasma	0.5	100	with	350	0.1	190	1.0
			without	850	120	700	500

Table 5a. Mechanical and thermal characteristics of adjacent cells (ij) within the same grain

Parameter of (i,j)-th bond	Anisotropy axes parallel to bond plain	Anisotropy axes perpendicular to bond plain
Young's modulus E_{ij} (dyn/cm ²)	$E_1 = 2 \cdot 10^{11}$	$E_2 = (0.3-0.7) E_1$
Thermal conductivity λ_{ij} (W/mK)	$\lambda_1 = 3.5$	$\lambda_2 = (0.5-0.7) \lambda_1$
Thermal expansion coefficient α_{ij} (K ⁻¹)	$\alpha_1 = 3 \cdot 10^{-6}$	$\alpha_2 = (2-4) \alpha_1$
Failure stress	distributed in the interval $10 \sigma_{0s} (0.5,1)$	

Table 5b. Mechanical and thermal characteristics of adjacent cells (ij) belonging to two different grains

Parameter of (i,j)-th bond	Anisotropy axes parallel to plain of surface bond	Anisotropy axes perpendicular to plain of surface bond	One axis parallel, adjacent perpendicular to plain of surface bond
Young's modulus E_{ij} (dyn/cm ²)	$E_1 = 2 \cdot 10^{11}$	$E_2 = (0.3-0.7) E_1$	$(E_1 + E_2)/2$
Thermal conductivity λ_{ij} (W/mK)	$\lambda_1 = 3.5$	$\lambda_2 = (0.5-0.7) \lambda_1$	$\lambda_1 \lambda_2 / (\lambda_1 + \lambda_2)$
Thermal expansion coefficient α_{ij} (K ⁻¹)	$\alpha_1 = 3 \cdot 10^{-6}$	$\alpha_2 = (2-4) \alpha_1$	$(\alpha_1 + \alpha_2)/2$
Failure stress σ_{0s}	distributed in the interval $\sigma_{0s} (0.5,1)$		

Appendix A1: Non steady state model of surface evaporation

Vapor above the surface of a condensed phase exists in a wide temperature range up to the critical temperature. The pressure p_s of the saturated vapor increases exponentially with the surface temperature. Surface evaporation starts when the pressure of the saturated vapor exceeds the external pressure p_0 given as sum of the stagnation pressure of the impacting hot plasma and the pressure of the plasma shield. The vaporization rate and the velocity of the evaporation front can change in a rather wide range depending on the surface temperature T_s , and the external pressure p_0 .

The parameters of the vapor behind the Knudsen layer expanding into the plasma shield (temperature T_g , density ρ_g , and expansion velocity u_g) can be expressed through the surface temperature T_s , the density of the saturated vapor ρ_s , and the sound velocity c_g corresponding to the surface temperature [18,19]. ρ_s is determined by the pressure of the saturated vapor and the surface temperature using the equation of state of the ideal gas (with μ and R the molar mass and the universal gas constant):

$$\rho_s = \mu p_s / RT_s \quad (\text{A1.1})$$

Data for the pressure of the saturated vapor $p_s(T_s)$ are taken from [17]. Metals are evaporated as single atoms graphite as mixture of atoms and molecules with C_3 the dominating species [32]. The total pressure of the saturated vapor of graphite is given as the sum of the partial pressure of its molecular components $p_i(T_s)$.

$$p_s(T_s) = \sum p_i(T_s) \quad (\text{A1.2})$$

with the summation over all species. The mean enthalpy of evaporation is averaged over the partial concentrations according to

$$\Delta H_{vap}(T_s) = \sum \Delta H_i^{vap} p_i(T_s) / p_s(T_s) \quad (\text{A1.3})$$

The mean molar mass μ of the graphite vapor is calculated according to

$$\mu = \sum \mu p_i(T_s) / p_s(T_s) \quad (\text{A1.4})$$

For the vapor expansion in case of presence of an external pressure three different cases are considered.

1. The external pressure p_0 is larger than the pressure of the saturated vapor p_s . Vaporization in this case is not occurring and the expansion velocity of the vapor is equal 0. No energy of the incoming fluxes is spent for vaporization and the surface temperature increases till the pressure of the saturated vapor exceeds the external pressure.

2. The pressure of the saturated vapor p_s is much larger than the external pressure p_0 ($p_s > 4p_0$). In this case the assumption of the vapor expansion into vacuum according to [18,19] can be applied with:

$$T_g = 0.67T_s, \quad \rho_g = 0.31\rho_s, \quad u_g = c_g \quad (\text{A1.5})$$

3. The pressure of the saturated vapor p_s is comparable with the external pressure $p_0 \leq p_s \leq 4p_0$. In this case the expansion velocity of the vapor behind the Knudsen layer is estimated from the hydrodynamic equation

$$\rho \frac{\partial u}{\partial t} = \frac{\partial p}{\partial x} \quad (\text{A1.6})$$

Solving eq. (A1.6) for the thin Knudsen layer results in

$$|u_g| = |p_s - p_0| \Delta t / \rho_s \Delta x \quad (\text{A1.7})$$

with Δt the time step, and Δx the characteristic size of the Knudsen layer (several mean free path of atoms, about 10^{-5} - 10^{-6} cm). The expansion velocity obtained from eq. (A1.7) is limited by the sound velocity ($u_g \leq c_g$). According to [18,19] the relative vapor temperature T_g/T_s and the relative vapor density ρ_g/ρ_s are functions of the relative expansion velocity $v = u_g/c_g$ and are given according to

$$\frac{T_g}{T_s} = F_T(v) = \frac{1 + 2,7v - 6,94v^2 + 2,64v^3}{1 + 2,7v - 4,46v^2 + 0,36v^3} \quad (\text{A 1.8})$$

$$\frac{\rho_g}{\rho_s} = F_\rho(v) = \frac{1 + 0,19v - 0,61v^2 + 0,4v^3}{1 + 2,28v - 0,15v^2 + 1,18v^3}$$

$v = u_g/c_g$ being known (u_g is obtained from eq. (A 1.7), the sound velocity c_g is calculated according to $c_g = \sqrt{5T_s/3m_a}$ with m_a the atomic mass of the evaporated species) then the unknown parameters T_g and ρ_g are obtained from eq. (A 1.8).

The velocity of the evaporation front is calculated from the mass conservation expression according to

$$u_{\text{vap}} = u_g \frac{\rho_g}{\rho} \quad (\text{A1.9})$$

with ρ the density of the condensed phase.

Appendix A2: Thermal energy transfer S_{th} to evaporating solid surfaces

For calculation of thermal energy transfer the conservation equations are solved with the 2 independent parameters: j_0 the flux of vaporized atoms and p_0 the pressure at the wall. The quasistationary conservation equations for mass, momentum and energy transfer are given as:

$$N_a u = j_0 \quad (A2.1)$$

$$m_a N_a u^2 + p = m_a j_0 u_0 + p_0 \quad (A2.2)$$

$$\left(\frac{1}{2} m_a N_a u^2 + w\right)u + S_{th} = \left(\frac{1}{2} m_a N_{a0} u_0^2 + w_0\right)u_0 + S_{th0} \quad (A2.3)$$

with N_a the density of the atoms, u the gas velocity, j_0 the number flux, p the total pressure (including electron pressure), w the enthalpy density $w = \varepsilon + p$ and m_a the mass of the atom. The internal energy density ε includes the thermal energy of ionized electrons and the ionization energy. The thermal heat flux S_{th} includes both atom and electron heat fluxes. The index 0 indicates the surface.

The pressure consists of two parts: $p = p_a + p_e$ with $p_a = N_a T$ the atom pressure and $p_e = N_e T$ the electron pressure with N_e the electron density. For quasineutrality $N_e = N_i$ is valid with N_i the ion density. Because of limited T_{max} ($T_{max} \leq 1.4$ eV) only singly ionized atoms are assumed ($0 \leq N_e \leq N_a$). It is valid $N_a = N_n + N_i$ with N_n the density of neutrals. At $N_e \rightarrow N_a$ all atoms are singly ionized. Local thermodynamic equilibrium is assumed, thus N_e is given by the Saha equation as

$$N_e^2 = 6 \cdot 10^{21} (g_i / g_n) N_n (T / \varepsilon_{eV})^{3/2} \exp(-I/T) \quad (A2.4)$$

with g_i and g_n the statistical weights of ions and neutrals, I the ground state ionization potential and ε_{eV} the energy associated with 1 eV. For the sake of simplicity equal values for g_i and g_n are used thus they disappear. The expression for w is given as $w = 2.5p + IN_e$.

The thermal heat flux S_{th} in the ionization layer is given as $S_{th} = -kdT/dx$ with k the thermal conductivity consisting of the two contributions from neutrals and electrons: $k = k_n + k_e$ (the contribution of ions is negligible compared to that of electrons). It is valid

$$k_n \approx \frac{1}{4} N_n T / (v_n m_a), \quad k_e \approx 3 N_e T / (v_e m_e) \quad (A2.5)$$

The neutral collision frequency is given as $\nu_n = N_n u_{thn} \sigma_n$ with $u_{thn} = (2T/m_a)^{1/2}$ the neutral thermal velocity and $\sigma_n \approx 5 \cdot 10^{-15} \text{ cm}^2$ typical neutral-neutral collision cross-section. The collisional frequencies of electrons with neutrals and ions are given as $\nu_e = \nu_{en} + \nu_{ei}$ with $\nu_{en} = N_n u_{the} \sigma_{en}$ and $\nu_{ei} \approx 10^{-5} N_i (\varepsilon_{eV}/T)^{3/2}$ with u_{th} the electron thermal velocity $u_{the} = (2T/m_e)^{1/2}$ and $\sigma_{en} \approx 5 \cdot 10^{-15} \text{ cm}^2$ the electron-neutral collisional cross-section.

Calculation of flow of carbon gas

For the following example are assumed: vaporization heat flux $S_{\text{vap}} = 1 \text{ GW/m}^2$ carbon gas pressure $p_0 = 2 \text{ bar}$ and graphite with $T_{\text{vap}} = 0.3 \text{ eV}$ and specific heat of vaporization $W_{\text{vap}} = 60 \text{ kJ/g}$.

The flux of vaporized atoms j_0 is obtained as $j_0 = S_{\text{vap}}/(m_a W_{\text{vap}}) \approx 10^{27} \text{ m}^{-2}\text{s}^{-1}$. At the wall the density of electrons is neglected. Thus $N_{a0} = p_0/T_0 \approx 4 \cdot 10^{24} \text{ m}^{-3}$ and $u_0 = j_0/N_{a0} \approx 2 \cdot 10^2 \text{ m/s}$ is obtained from Eq. (A2.1). It is necessary to check the Chapman-Jouguet condition that limits the velocity of the vaporizing gas as $u_0 < c_s \approx u_{\text{thn0}}$ with $c_s = (5T_{\text{vap}}/3m_a)^{1/2}$ the sound velocity. The neutral thermal velocity at the wall is obtained as $u_{\text{thn0}} \approx 2 \cdot 10^3 \text{ m/s}$, thus this requirement is met (for carbon it is met if the relation p_0/S_{vap} is large enough: $p_0[\text{bar}]/S_{\text{vap}}[\text{GW/m}^2] \geq 2$). For carbon it is valid $I = 11.2 \text{ eV}$. Using this in Eq. (A2.4), the electron density at the wall is obtained as $N_{e0} \approx 10^{18} \text{ m}^{-3}$. Thus the ionization degree at the wall is rather small ($N_{e0}/N_{a0} \approx 2 \cdot 10^{-7}$).

Assuming $S_{\text{th0}} = 0$ in eq. (A2.3), the temperature gradient is zero at $x = 0$. In this case the gas flux propagates from the wall without change keeping its parameters at any $x > 0$ equal to that at $x = 0$. If at some position x_{max} the temperature is given as $T = T_{\text{max}}$ ($T_{\text{max}} > T_{\text{vap}}$), the increase of T from T_{vap} to T_{max} is due to $S_{\text{th0}} > 0$. In the hydrodynamic approximation the absolute value of S_{th0} cannot exceed that of the neutral kinetic heat flux to the wall given as $S_{\text{kin0}} = -N_{a0}u_{\text{thn0}}T_{\text{vap}}/\pi^{1/2} \approx -250 \text{ GW/m}^2$. At larger $|S_{\text{th0}}|$ the hydrodynamics fails, and in front of the wall a gas of boundary temperature T_b with $T_b > T_{\text{vap}}$ arises. In a first step the system of eqs. (A2.1) to (A2.3) is solved for $|S_{\text{th0}}| < |S_{\text{kin}}|$.

After excluding u by using Eq. (A2.1), it is obtained from Eq. (A2.2) and Eq. (A2.3):

$$\frac{m_a j_0^2}{N_n + N_e} + (N_n + 2N_e)T = m_a j_0 u_0 + p_0 \quad (\text{A2.6})$$

$$k \frac{dT}{dx} = \left(\frac{1/2 m_a j_0^2}{N_n + N_e} + 2.5 N_n T + (5T + I) N_e \right) \frac{j_0}{N_n + N_e} - \left(\frac{1}{2} m_a j_0 u_0 + 2.5 p_0 \right) u_0 - S_{\text{th0}} \quad (\text{A2.7})$$

The boundary condition for eq. (A2.7) is given as $T|_{x=0} = T_{\text{vap}}$. At each step i of integration of eq. (A2.7) the value of $T(x_i)$ is known. After solving the system of eqs. (A2.4) and (A2.6) the values of N_n and N_e become also known. The heat conductivity k and the right hand side (RHS) of Eq. (A2.7) depend on T , N_n and N_e thus they are known, too. This allows to come to the next step with $x_{i+1} = x_i + \Delta$ using e.g. the simplest numerical scheme $T(x_{i+1}) = T(x_i) + (\text{RHS}/k)\Delta$ with Δ the size of the spatial mesh.

Results of calculations for $S_{\text{th0}} = 0.3 S_{\text{kin0}} \approx -7.5 \text{ GW/m}^2$ are shown in Figs. A2.1 - 4. As is to be seen from these Figures, a temperature change of 1 eV occurs in a layer of rather small thickness of 10 μm . With increasing x , the electron density changes drastically from 10^{18} up to $5 \cdot 10^{23} \text{ cm}^{-3}$. The neutral density changes from $4 \cdot 10^{24}$ down to $3 \cdot 10^{22} \text{ cm}^{-3}$. Substantial ionization occurs at $T > 1 \text{ eV}$. But even at smaller temperatures the thermal transport is dominated by electrons. Only just near the wall (at the distance of 0.1 μm) electron heat conduc-

tion vanishes and the electron heat flux transforms into the neutral heat flux. The electron heat flux changes significantly across the ionization layer because the thermal energy is consumed for ionization, heating and acceleration of the gas coming from the wall as demonstrates Fig. A2.4 for the gas velocity.

If $|S_{th0}| > |S_{kin0}|$, the hydrodynamic approach near the wall fails at a distance of one free path of the vapor particles. The atoms emitted from the wall get vapor temperature within the relaxation length l_r . l_r is assumed to be small compared to the thickness l of the ionization layer. The non-hydrodynamic increase of T from T_{vap} to T_b occurs over the region of $0 < x < l_r$. At $x > l_r$ the hydrodynamic approach is assumed to be valid. Due to the small l_r the parameters of the vapor in front of the wall are prescribed to the position $x = 0$, in particular it is valid $T_b = T_0$. This jump approximation fully ignores the structure of the narrow non-hydrodynamic region. Eq. (A2.3) doesn't depend on the hydrodynamic approximation. Due to this it fits together the wall and the vapor boundary at $x = 0$ as

$$\left(\frac{1}{2}m_a u_w^2 + 2.5T_{vap}\right)j_0 = \left(\frac{1}{2}m_a j_0 u_0 + w_0\right)u_0 + S_{th0}$$

In fact this is the equation for the vapor velocity u_w at the wall. Calculating u_w from here the Chapman-Jouguet condition $u_w < c_s$ is controlled.

A kinetic expression for S_{th0} is applied as

$$S_{th0} = S_{kin} = -\left(N_{n0}\sqrt{2T_b/m_a} + gN_{e0}\sqrt{2T_b/m_e}\right)T_b/\sqrt{\pi} \quad (A2.8)$$

The coefficient g in Eq. (A2.8) accounts for a barrier $e\phi_w$ due to an electric potential in an electrostatic sheath which prevents free arrival of the electrons at the wall. According to the sheath theory, in case of a not emitting wall the biased potential is given as $e\phi_w = \frac{1}{2}\ln(4\pi m_a/m_e) \approx 3.7T_b$. One electron brings the energy $2T_b$ to the wall, one ion brings $2.5T_b + e\phi_w$, and the number fluxes of ions and electrons to the wall are equal. Therefore, the kinetic energy flux of the charged particles is obtained as

$$S_{kin} = (2 + 2.5 + 3.7)T_b N_{i0}(2T_b/m_a)^{1/2}/(2\pi^{1/2}) = gN_{e0}(2T_b/m_e)^{1/2}T_b/\pi^{1/2} \quad (A2.9)$$

Thus at $N_{i0} = N_{e0}$ it is obtained $g = g_{min} = 4.1(m_e/m_a)^{1/2} \approx 2.8 \cdot 10^{-2}$.

In order to control the hydrodynamic approximation ($|S_{th}| < |S_{kin}|$) inside the ionization layer eq. (A2.8) can be used. If hydrodynamics fails then internal electrostatic sheathes appear inside the non-hydrodynamic regions. Electron emission from the plasma of the cold sheath side decreases the electric barrier drastically and thus increases the coefficient g . The internal electric thermal insulation becomes rather small and therefore is neglected thus $g = g_{max} = 1$. The electron emission is assumed to appear at the distance exceeding the electron free path λ_e from the wall. The final modeling expression for g is given as $g = g_{min} + (g_{max} - g_{min})/(1 + \lambda_e/x)$ with $\lambda_e = u_{the}/v_e$.

The values of N_{n0} and N_{e0} depend on T_b and are obtained from the equations $N_{a0} + n_{e0} = p_0/T_b$, $N_{a0} = N_{n0} + N_{e0}$ and from Eq. (A2.4) used for $T = T_b$, $N_n = N_{n0}$ and $N_e = N_{e0}$.

Thus the kinetic problem for the ionization layer is reduced to the previous hydrodynamic problem but the boundary condition for eq. (A2.7) is given as $T|_{x=0} = T_b$.

As an example the case with a non conducting wall and zero radiation flux is considered, thus $S_{th0} = -S_{vap}$. As previously, $p_0 = 2$ bar and $S_{vap} = 1$ GW/m² is assumed. Profiles of temperature and of $|S_{th}|$ and $|S_{kin}|$ are shown in Figs. A2.5 and A2.6. This example demonstrates that the ionization layer may require a kinetic description because its non-hydrodynamic part extends over more than 30% of the layer thickness. The boundary temperature of the vapor is obtained as $T_b \approx 0.8$ eV. The thickness δ as obtained from eq. A2.7 of the layer is about 1 μ m.

The developed model based on eq. (A2.7) was implemented in FOREV with the parameters j_0 and ρ obtained selfconsistently in the course of the simulation. Eq. (A2.9) is used for the control of the kinetic fluxes and the thickness of the non hydrodynamics region. For large energy fluxes where δ is smaller than the size Δ of the first mesh ($\delta \ll \Delta$) the small temperature region was neglected and the boundary condition $T_b = T_{max}$ was used in FOREV-2. In the opposite case when $\delta \geq \Delta$ the boundary temperature was obtained from the relation

$$T_b = T_{vap} + (T_{max} - T_{vap}) \frac{\Delta}{\delta} \quad (A2.10)$$

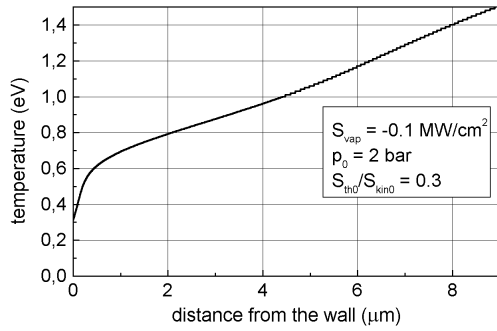


Fig. A2.1 Temperature profile across the ionization layer

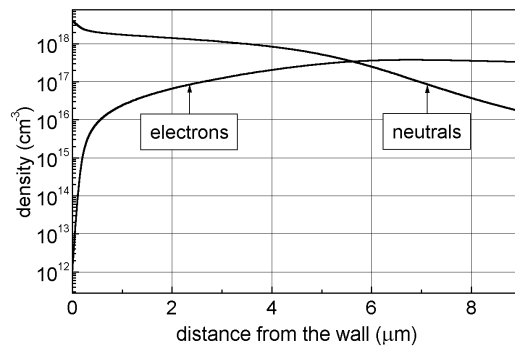


Fig. A2.2 Density of electrons and neutrals in the ionization layer

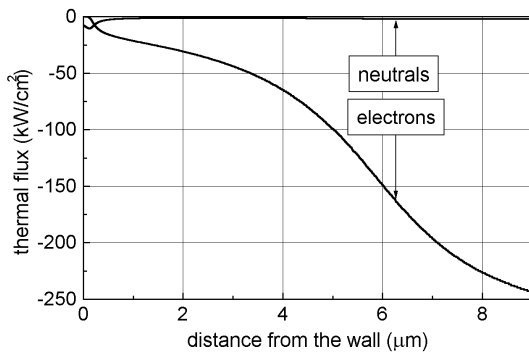


Fig. A2.3. Thermal flux across the ionization layer

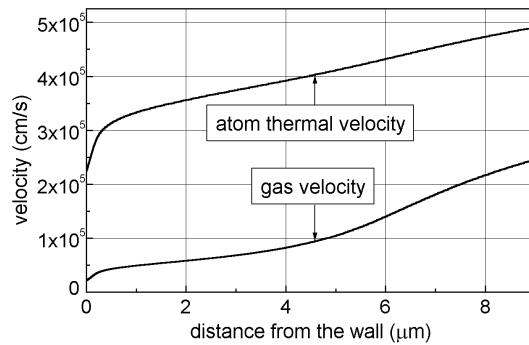


Fig. A2.4. Thermal velocity of atoms

Figs. A2.1-A2.4. Thermal energy transport to the wall for $S_{vap}=10GW/m^2$ in case of hydrodynamic approximation

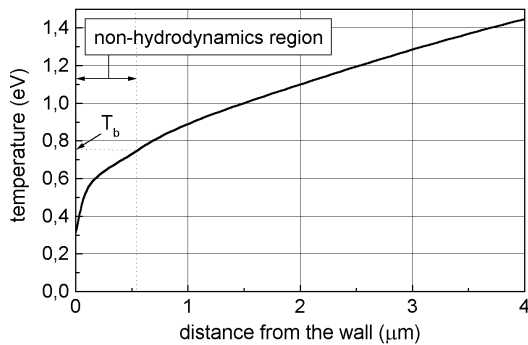


Fig. A2.5 Temperature profile in the ionization layer

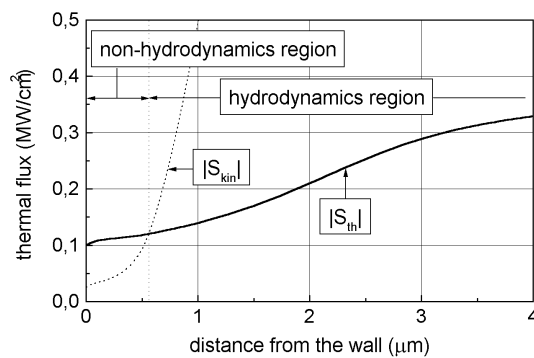


Fig. A2.6 Thermal flux profile in the ionization layer

Figs. A2.5 and A2.6. The ionization layer at $|S_{th0}|=S_{vap}=1GW/m^2$ and $p_0=2bar$.

Appendix A3: Numerical model of the brittle destruction

The graphite sample consists of quadratic cells, each of them are denoted by integer coordinates (i,j) , see Fig. 47. The variables of the problem, defined for each cell of the sample are:

$T_{i,j}$ - cell temperature defined in the centre of the (i,j) -th cell,

$r_{i,j} = (x_{i,j}, y_{i,j})$ – shift of the centre of the (i,j) -th cell centre from its initial position when $T_{i,j}=T_0$ for all i,j in the sample.

$F_{x,i,j}$ – elastic force, acting normally on the right side of the (i,j) -th cell in x direction.

$F_{y,i,j}$ – elastic force, acting normally on the upper side of the (i,j) -th cell in y direction.

$K_{x,i,j}$ – elastic force, acting tangentially on the upper side of the (i,j) -th cell in x direction.

$K_{y,i,j}$ – elastic force, acting tangentially on the right side of the (i,j) -th cell in y direction.

There are 8 forces, acting on each cell in the 2 dimensional sample. They are shown in Fig. 54. The elastic forces acting on a cell are calculated according to the following formulas:

On the right hand side of the (i,j) -th cell

$$F_{x,i,j} = E_{i+\frac{1}{2},j} \left\{ x_{i+1,j} - x_{i,j} - a\alpha_{i+\frac{1}{2},j} (T_{i+\frac{1}{2},j} - T_0) \right\}$$

$$K_{x,i,j} = G_{i,j+\frac{1}{2}} (x_{i,j+1} - x_{i,j})$$

On the upper side of the (i,j) -th cell

(A3.1)

$$F_{y,i,j} = E_{i,j+\frac{1}{2}} \left\{ y_{i,j+1} - y_{i,j} - a\alpha_{i,j+\frac{1}{2}} (T_{i,j+\frac{1}{2}} - T_0) \right\}$$

$$K_{y,i,j} = G_{i+\frac{1}{2},j} (y_{i+1,j} - y_{i,j})$$

where

$E_{i+\frac{1}{2},j} = (E_{i+1,j} + E_{i,j})/2$ – is the Young's modulus for deformations in the x direction for the interspace between the centres of the (i,j) -th and $(i+1,j)$ -th cell, $E_{i,j}$ is equal to E_1 or E_2 depending on the directions of the anisotropy axes of the (i,j) -th cell and of the $(i+1,j)$ -th cell.

$E_{i,j+\frac{1}{2}} = (E_{i,j+1} + E_{i,j})/2$ – is the Young's modulus for deformations in the y direction for the interspace between the centres of the (i,j) -th and $(i,j+1)$ -th cell.

$G_{i+\frac{1}{2},j} = (G_{i+1,j} + G_{i,j})/2$ – is the shear modulus for shear deformations in the y direction for the interspace between the centres of the (i,j) -th and $(i+1,j)$ -th cell, $G_{i,j}$ is equal to G_1 or G_2 depending on anisotropy axes directions of the (i,j) -th cell and of $(i+1,j)$ -th cell.

$G_{i,j+\frac{1}{2}} = (G_{i,j+1} + G_{i,j})/2$ – is the shear modulus for shear deformations in the x direction for the interspace between the centres of the (i,j) -th and $(i,j+1)$ -th cell.

$$T_{i+\frac{1}{2},j} = (T_{i+1,j} + T_{i,j})/2.$$

$$T_{i,j+\frac{1}{2}} = (T_{i,j+1} + T_{i,j})/2.$$

$\alpha_{i+\frac{1}{2},j} = (\alpha_{i+1,j} + \alpha_{i,j})/2$ – is the linear expansion coefficient in x direction for the interspace between (i,j) -th and $(i+1,j)$ -th cell centres, $\alpha_{i,j}$ is equal to α_1 or α_2 depending on anisotropy axes directions of the (i,j) -th cell and of $(i+1,j)$ -th cell.

$\alpha_{i,j+\frac{1}{2}} = (\alpha_{i,j+1} + \alpha_{i,j})$ – is the linear expansion coefficient in the y direction for the interspace between the directions of the (i,j) -th and $(i,j+1)$ -th cell.

Initially the sample consists of cubic cells of size a of uniform temperature T_0 . The cell centres are not shifted: all r_{ij} are equal to zero. According to eq. (A3.1) all the forces are zero at this moment, thus defining the equilibrium. Then, the sample is heated and the temperature changes according to the equation:

$$\frac{dT_{i,j}}{dt} = v_{i+\frac{1}{2},j}(T_{i+1,j} - T_{i,j}) + v_{i-\frac{1}{2},j}(T_{i,j} - T_{i-1,j}) + v_{i,j+\frac{1}{2}}(T_{i,j+1} - T_{i,j}) + v_{i,j-\frac{1}{2}}(T_{i,j} - T_{i,j-1}) + \omega_{i,j} \quad (\text{A3.2})$$

with $v_{i+\frac{1}{2},j} = (v_{i+1,j} + v_{i,j})/2$ – is the thermoconductivity coefficient in x direction for the transition from the (i,j) -th to the $(i+1,j)$ -th cell. $v_{i,j}$ is given as $v_{i,j} = \lambda_{i,j}/\rho ca^2$ with $\lambda_{i,j}$ equal to λ_1 or λ_2 depending on the directions of the anisotropy axes of the (i,j) -th cell and of the $(i+1,j)$ -th cell.

$v_{i,j+\frac{1}{2}} = (v_{i,j+1} + v_{i,j})$ – is the thermoconductivity coefficient in the y direction between the (i,j) -th and the $(i,j+1)$ -th cell $\omega_{i,j} = \frac{w_{i,j}}{\rho c}$, with $w_{i,j}$ the volumetric heating and λ_1 and λ_2 are thermal conductivity coefficients perpendicular and parallel to the atomic layers correspondingly.

Changing the cell temperatures results in the forces $F_{x,i,j}$ and $F_{y,i,j}$ due to the linear expansion coefficient α . The linear expansion of the cells results in a shift of the centre positions of the cells. The new positions are calculated from the condition of mechanical equilibrium for the sample according to the equations:

$$\frac{dx_{i,j}}{d\tau} = -\frac{\partial H}{\partial x_{i,j}} = (F_{x,i,j} - F_{x,i-1,j} + K_{x,i,j} - K_{x,i,j-1}), \quad (\text{A3.3})$$

$$\frac{dy_{i,j}}{d\tau} = -\frac{\partial H}{\partial y_{i,j}} = (F_{y,i,j} - F_{y,i-1,j} + K_{y,i,j} - K_{y,i,j-1}).$$

Mechanical equilibrium is achieved much faster, than the heat transport (according to eq. A3.2). Therefore instantaneous equilibration of the mechanical forces is assumed. Eq. A3.3 is solved using a fictitious time τ . The real time t and temperature distribution are not changed during this equilibration process. eq. A3.3 is solved in an iterative way – the shifts of the cell centres are used to calculate forces according to eq. A1 and then new shifts are calculated from eq. A3.3. This process is continued iteratively till all the shifts of the cell centres get stationary, $dx_{i,j}/d\tau=0$ and $dy_{i,j}/d\tau=0$, what means that all forces, acting on each cell are zero. In reality as criterion for stopping this process it was used the condition, that the final forces acting on the cells are less than 1% of the mean force.

Checking of breaking of bonds is done after achievement of equilibrium. The criteria are:

$$\left|F_{x,i,j}\right| + \left|K_{y,i,j}\right| \geq \sigma_{i,j} E_{i+\frac{1}{2},j} a^2 \text{ for the vertical bond, and} \quad (\text{A3.4})$$

$$\left|F_{y,i,j}\right| + \left|K_{x,i,j}\right| \geq \sigma_{i,j} E_{i,j+\frac{1}{2}} a^2 \text{ for the horizontal bond.}$$

If A3.4 is fulfilled then the corresponding bond is assumed to be broken.

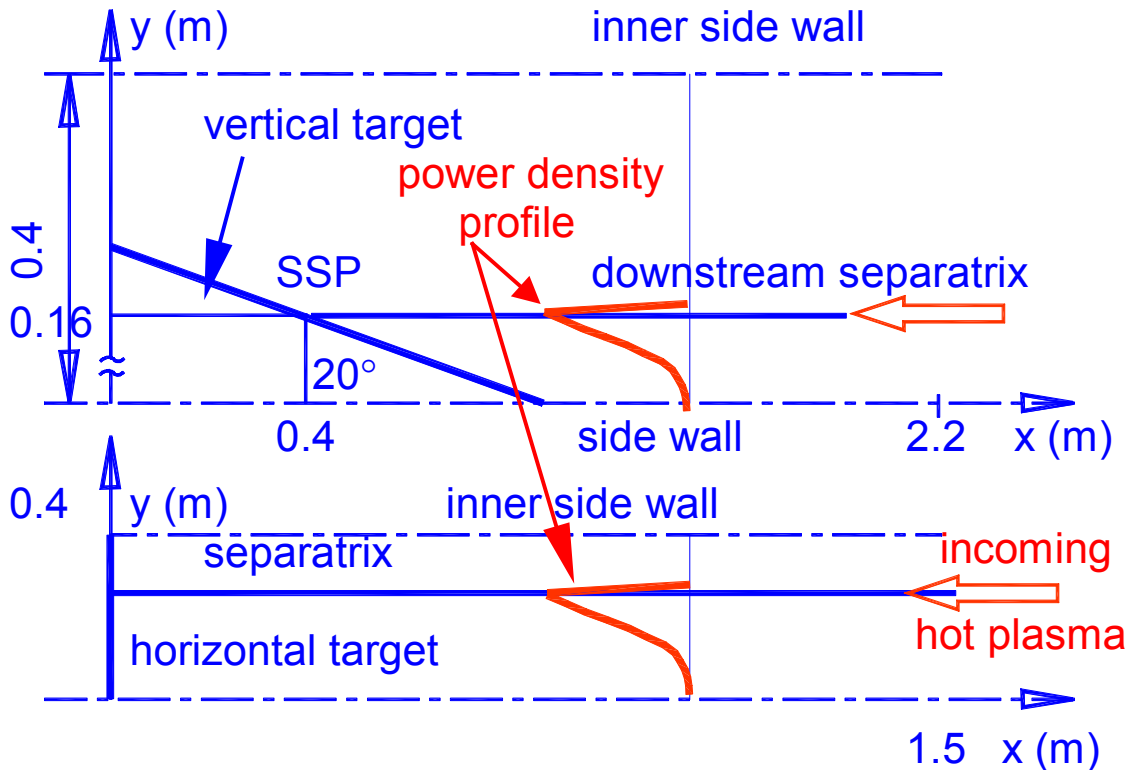


Fig.1. Simplified 2-D geometry for describing the ITER-FEAT divertor with a vertical and a horizontal target in the poloidal plane and the inner wall. The inclination angle in toroidal direction is 2° , the magnetic field is $\vec{B} = (B_x, B_y, B_z) = (0.17T, 0, 5T)$.

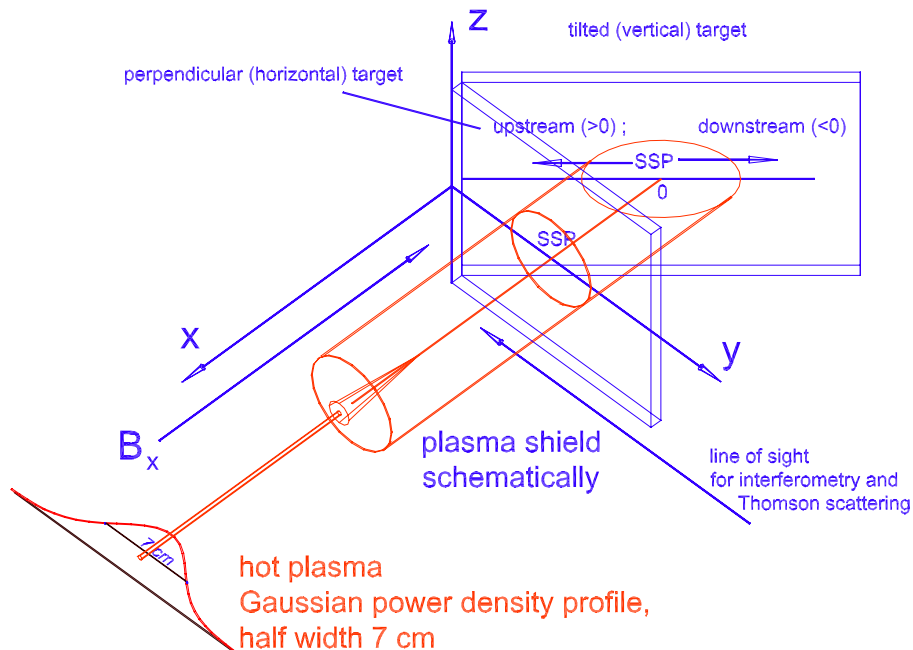


Fig. 2. Scheme of the 2-D geometry of the simulation experiments performed at the MK-200 UG facility for perpendicular and inclined targets.

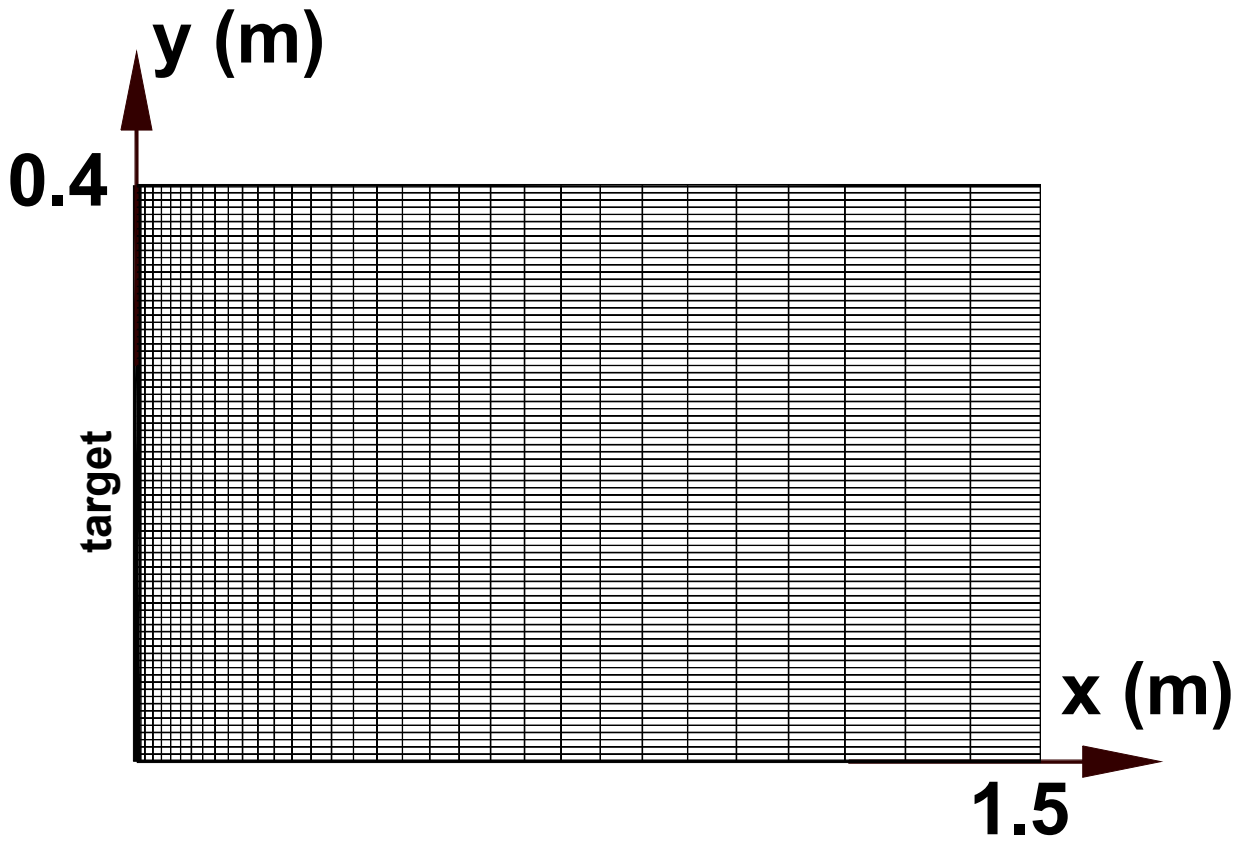


Fig. 3a. Computational grid for horizontal target in poloidal plane.

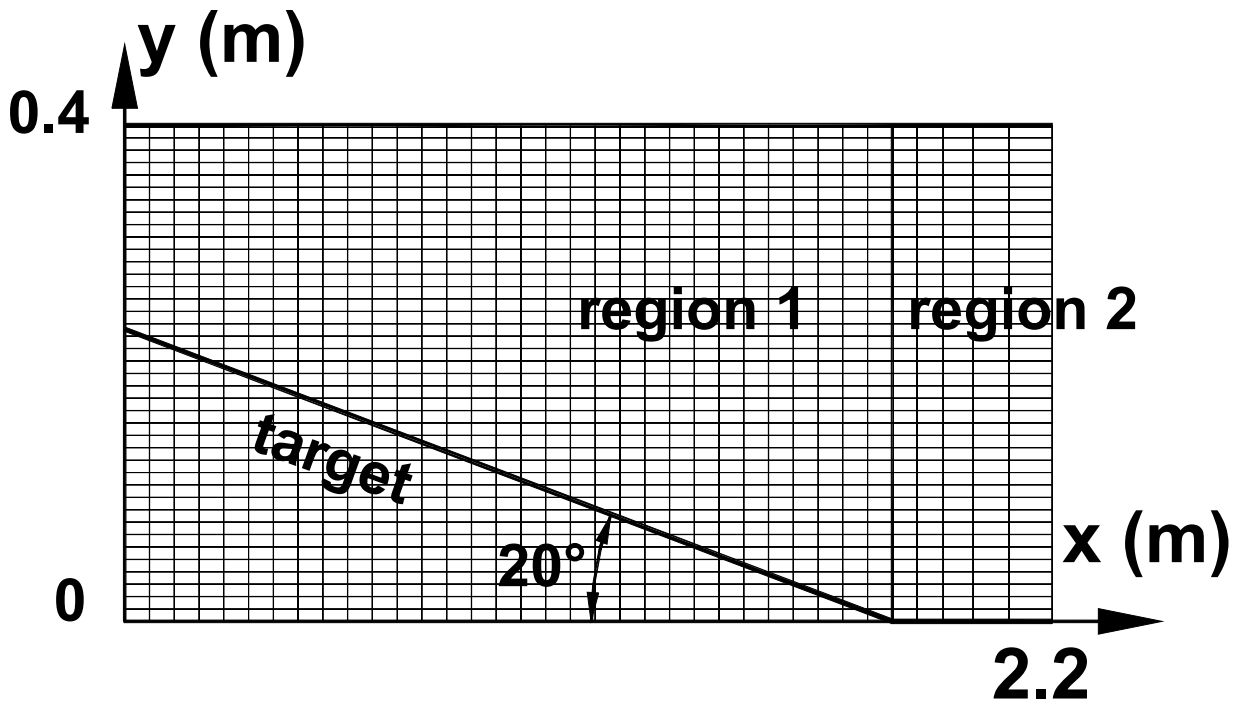


Fig. 3b. Computational grid for vertical target in poloidal plane.

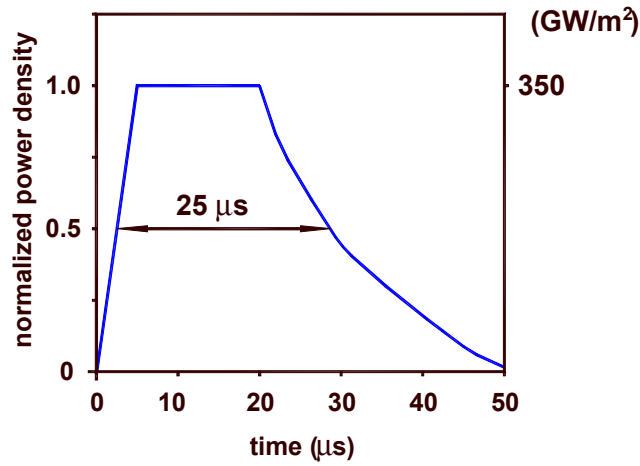


Fig.4. Time dependent power density as used in the simulation calculations for the MK-200 UG facility. Peak power density (target heat load) is 350 GW/m². Guiding magnetic field at the target position is 2 T.

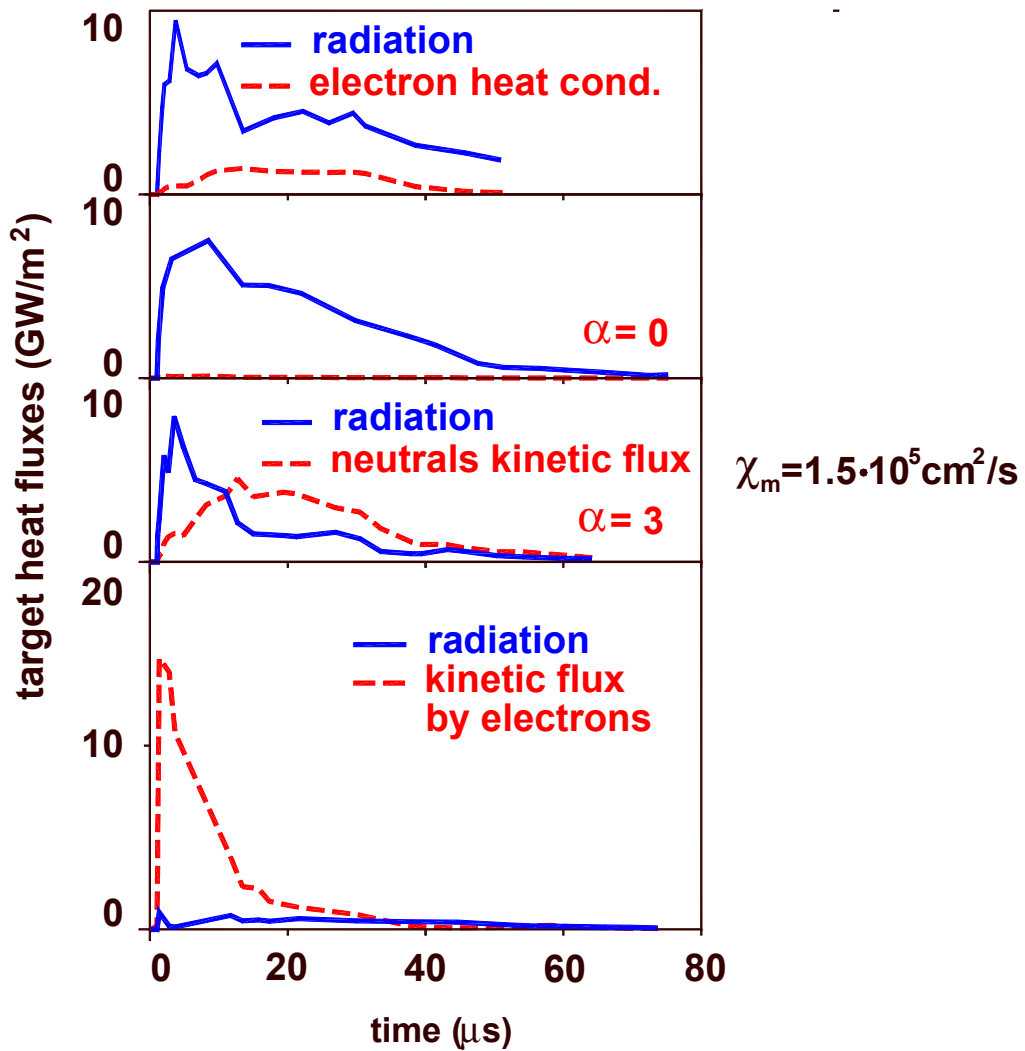


Fig. 5. Comparison of calculated target heat fluxes for different cases of the thermal energy transfer S_{th} to the target for a perpendicular graphite target at the MK-200 UG facility. Gaussian power density profile with peak power density of 350 GW/m².

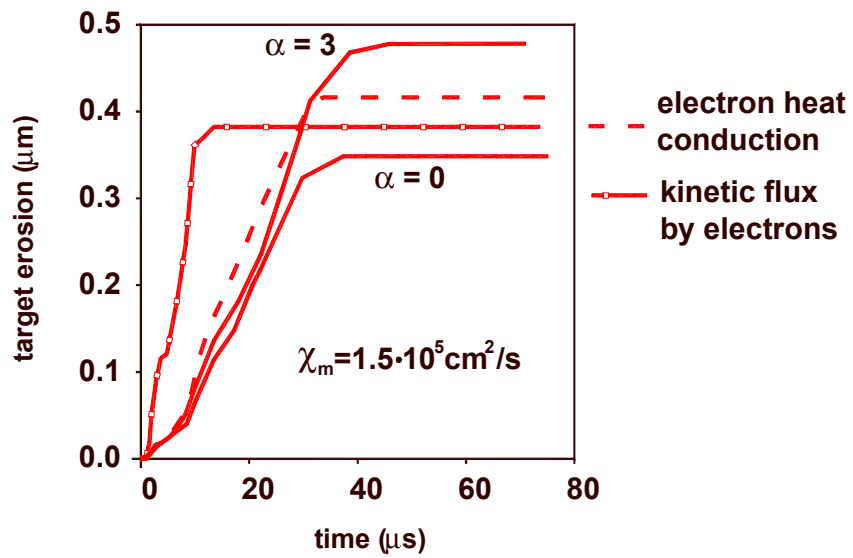


Fig. 6. Erosion rate for a perpendicular graphite target under the MK-200 UG conditions for 4 different values of the thermal energy transport to the target.

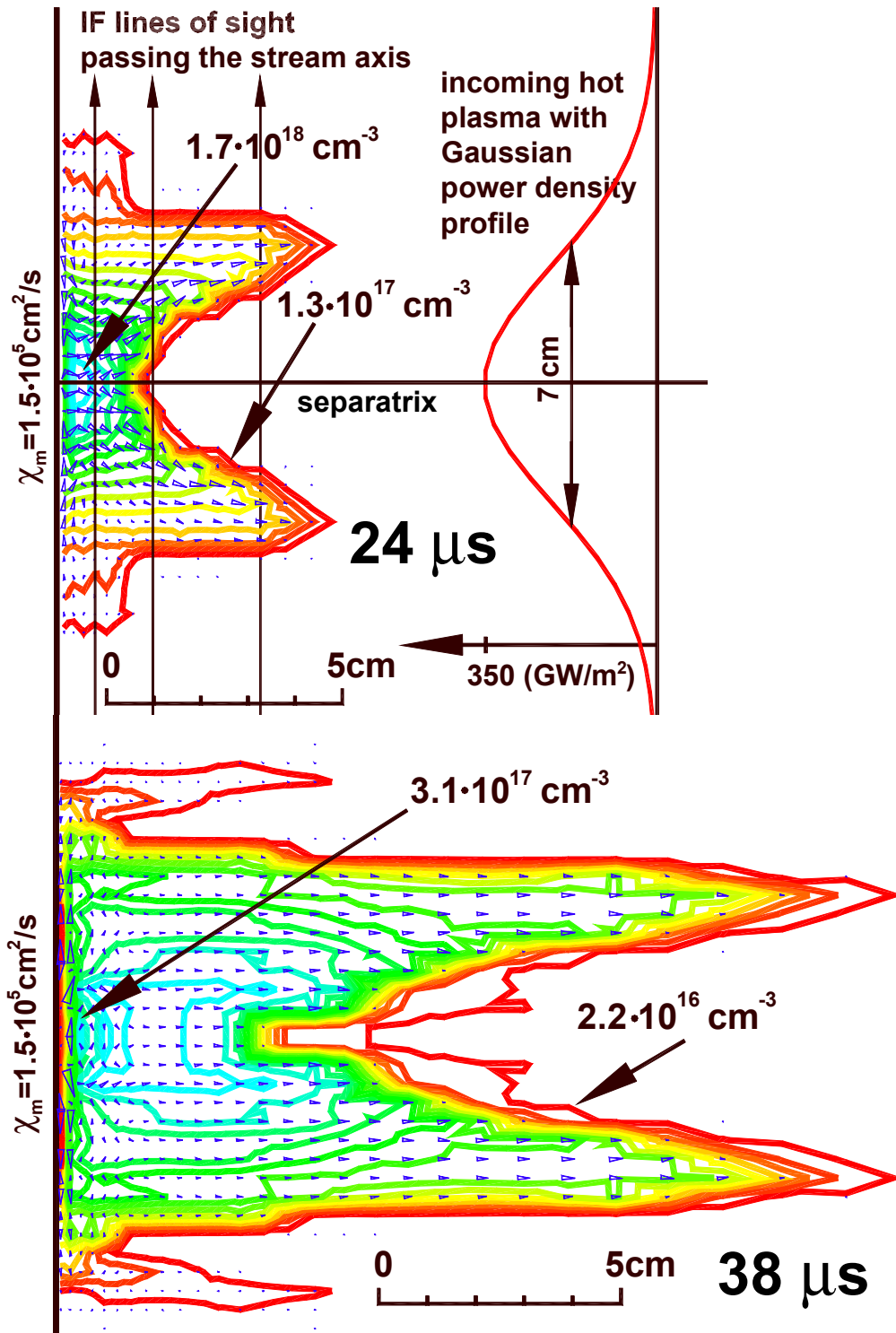


Fig.7. Calculated plasma flow pattern and electron density distributions in a cold and dense carbon plasma shield with temperatures below 3 eV at 24 μs and 38 μs for $\chi_m = 1.5 \cdot 10^5 \text{ cm}^2/\text{s}$ for a perpendicular graphite target for classical diffusion under MK-200 UG conditions.

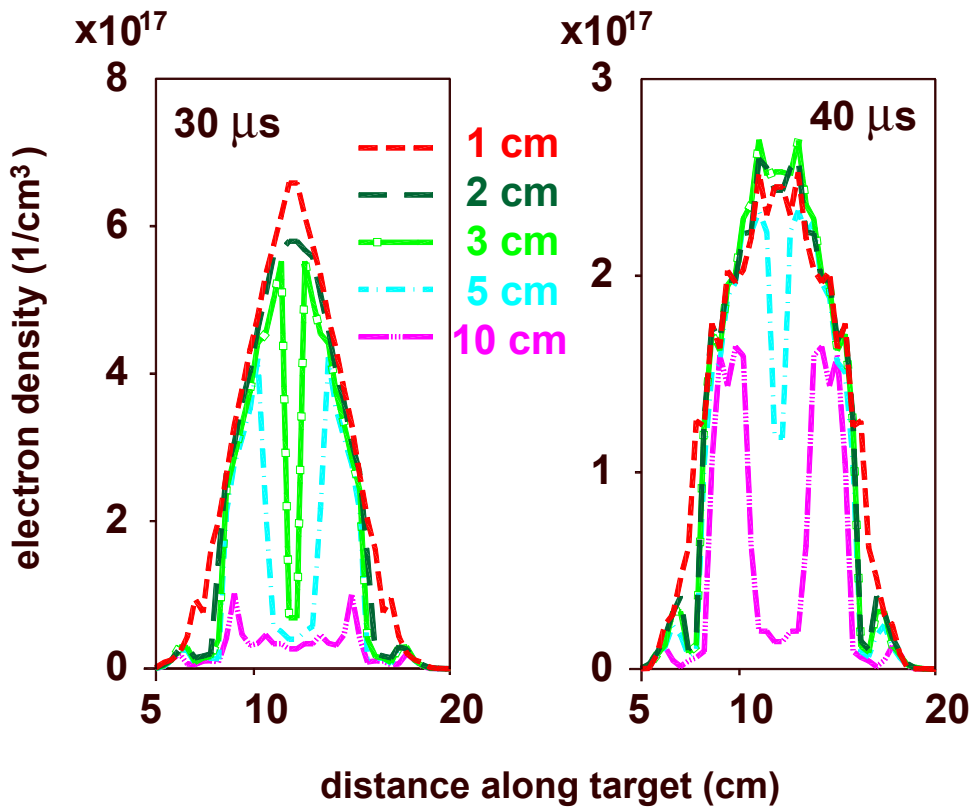


Fig. 8. Calculated profiles of electron density in a carbon plasma shield along the IF lines of sight at 30 μs and 40 μs at different distances from the target as indicated in the figure at the MK-200 UG facility.

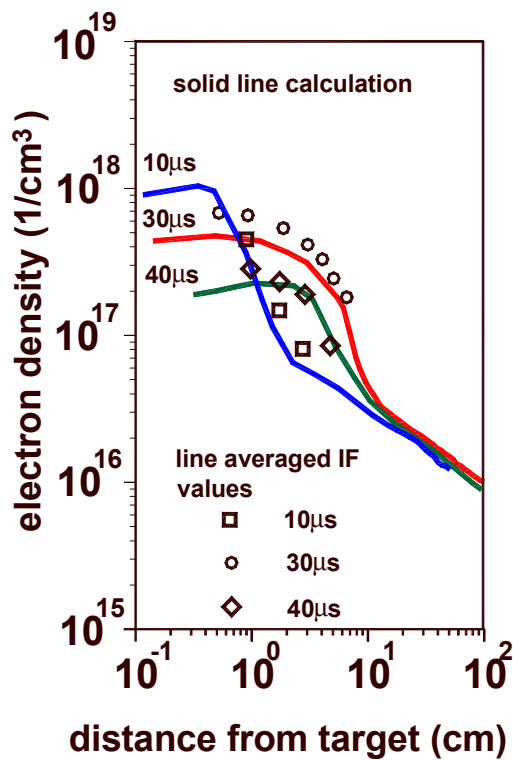


Fig. 9. Comparison of measured and calculated line averaged electron density distributions in a carbon plasma shield along the separatrix at different times for a perpendicular graphite target at the MK-200 UG facility.

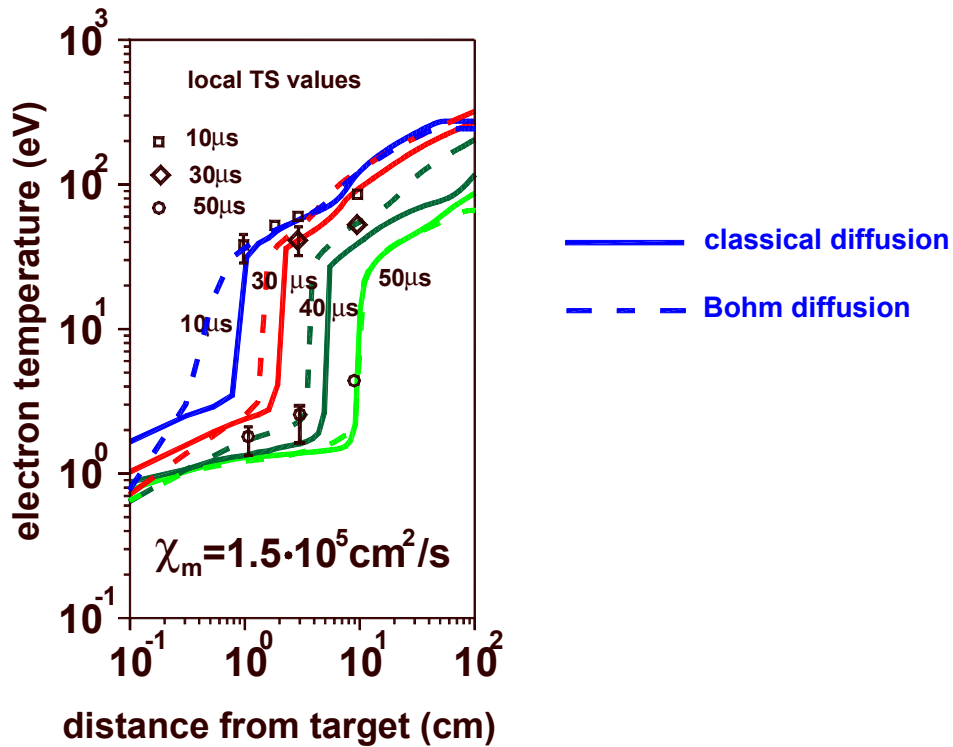


Fig. 10. Comparison of measured and calculated local electron temperature profiles in a carbon plasma shield along the separatrix for a perpendicular graphite target at the MK-200 UG facility.

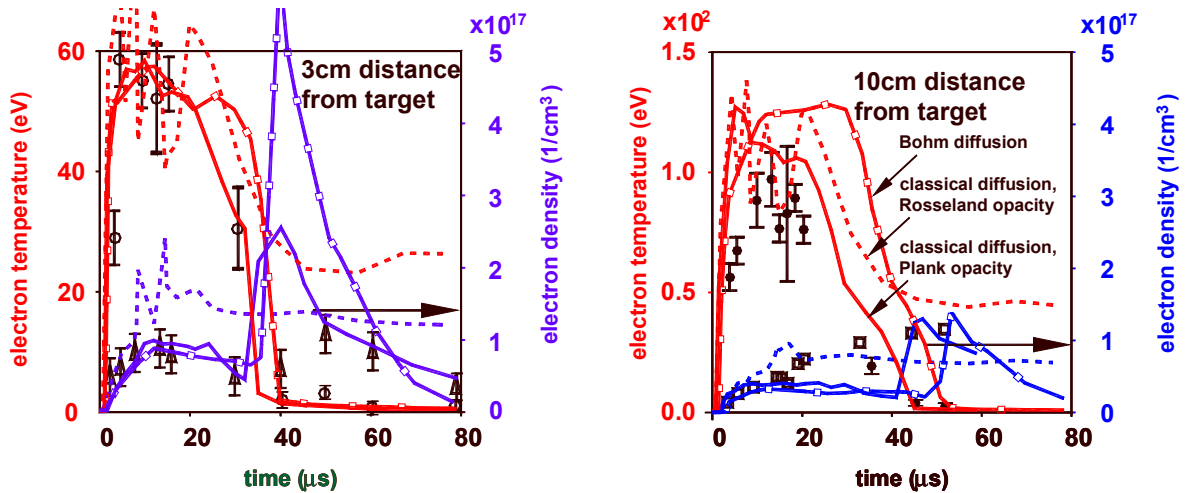


Fig. 11. Comparison of calculated and measured evolution of electron density and temperature in a carbon plasma shield at the separatrix, at 3 cm and 10 cm distance from the target for a perpendicular graphite target at the MK-200 UG facility. Calculations were performed for 69 group Planck and 24 group Rosseland opacities. For Planck opacities classical and Bohm diffusion were used.

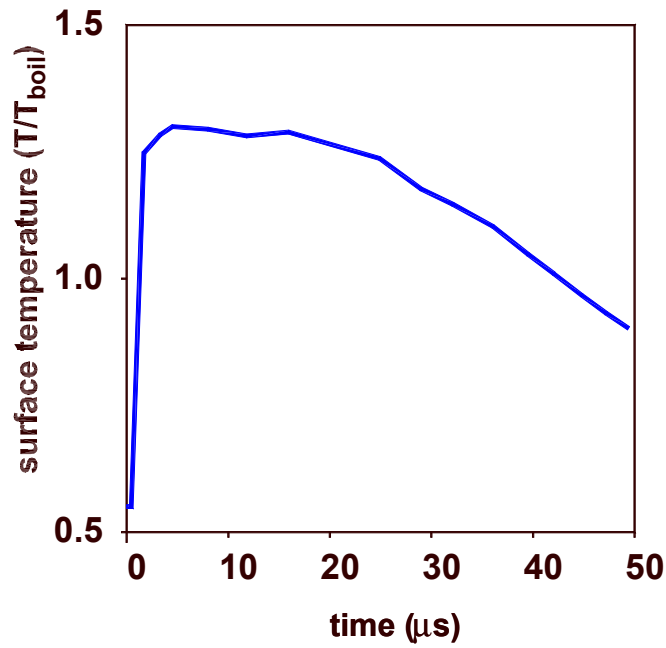


Fig.12. Calculated time dependent surface temperature of the graphite target under the experimental conditions of the MK-200 UG facility.

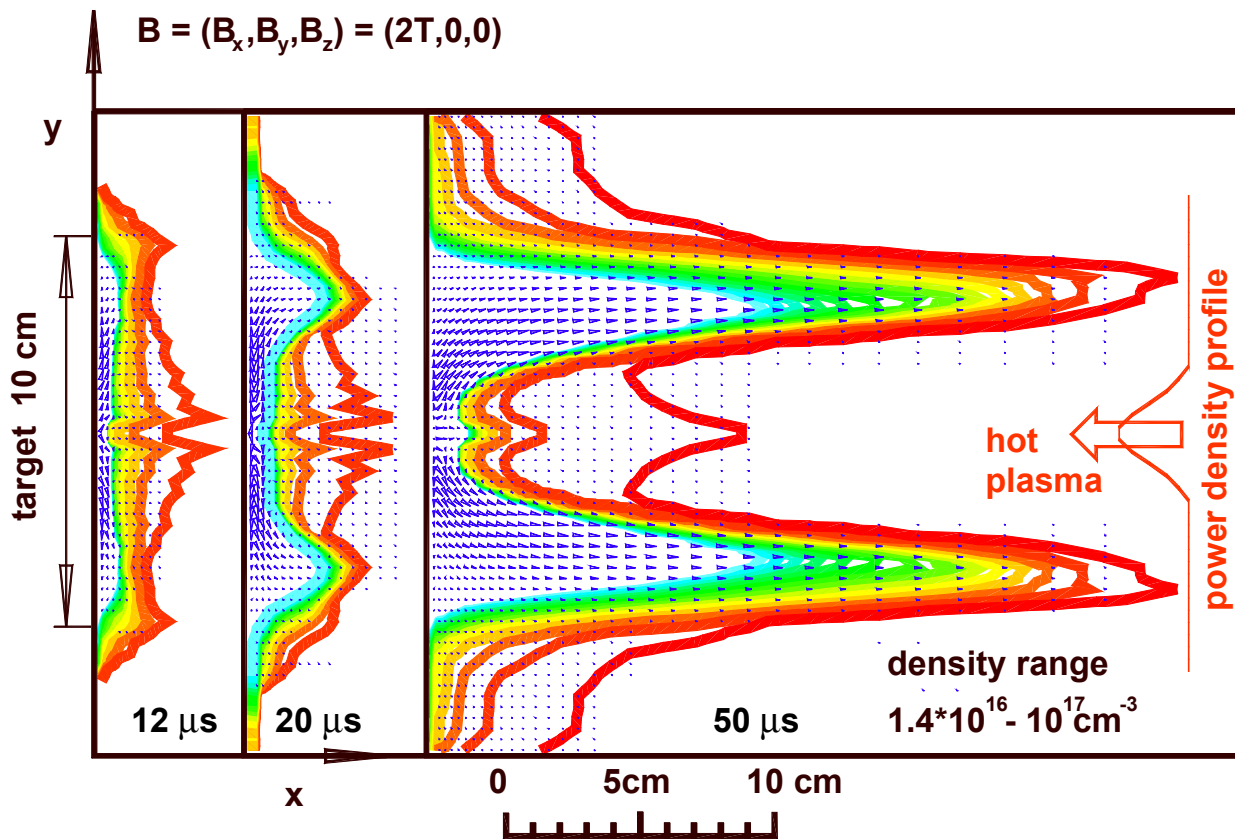


Fig.13. Contour plots of calculated density and plasma flow (arrows) in an quartz plasma shield for perpendicular quartz target at the MK-200 UG facility. Gaussian power density profile with peak value of 350 GW/m^2 . Guiding magnetic field is 2T.

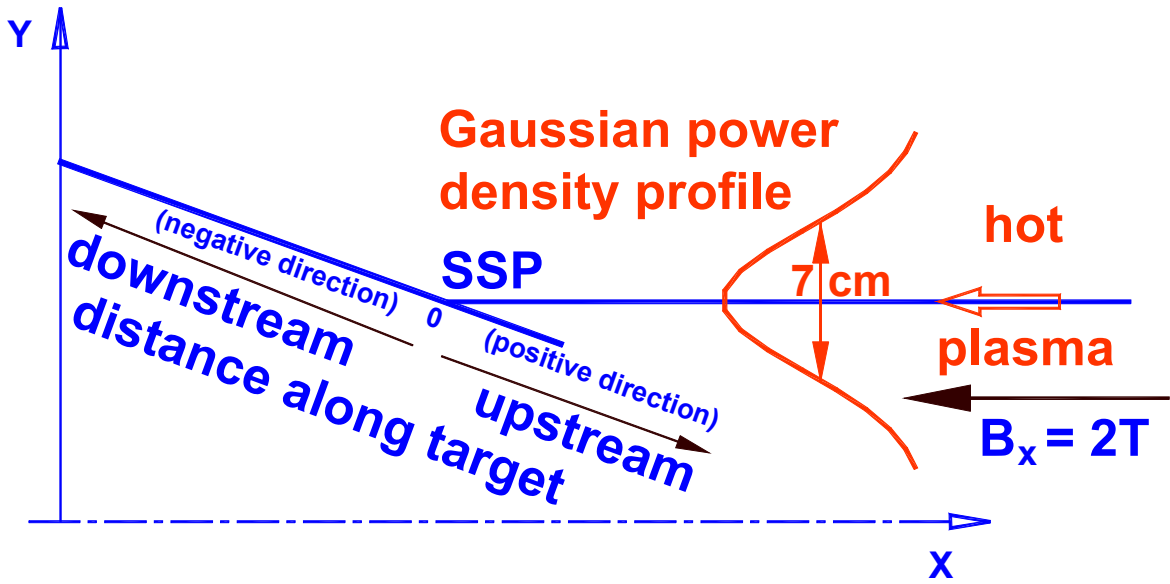


Fig. 14. Experimental arrangement in the simulation experiments at the MK-200 UG plasma gun facility with vertical targets showing up- and downstream direction

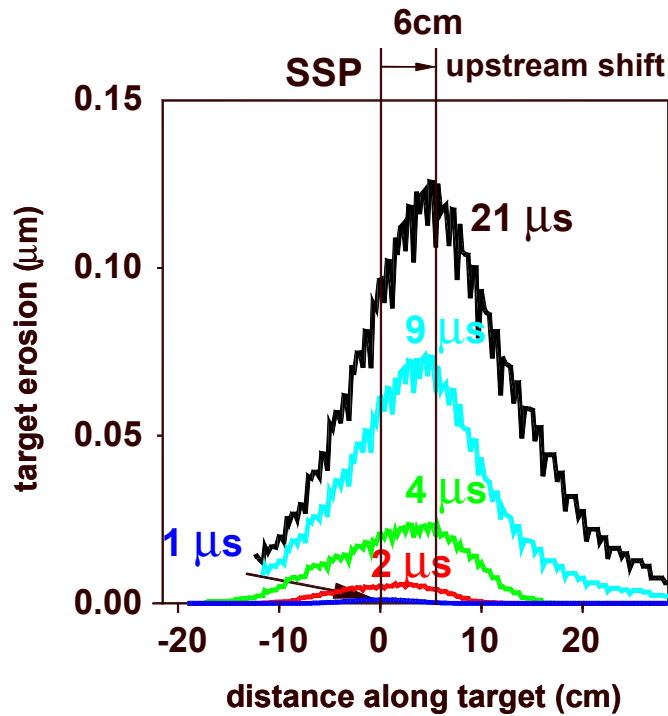


Fig. 15. Calculated erosion profiles for a vertical graphite target at the MK-200 UG facility at different times showing widening of the evaporation region and upstream shift of the profiles

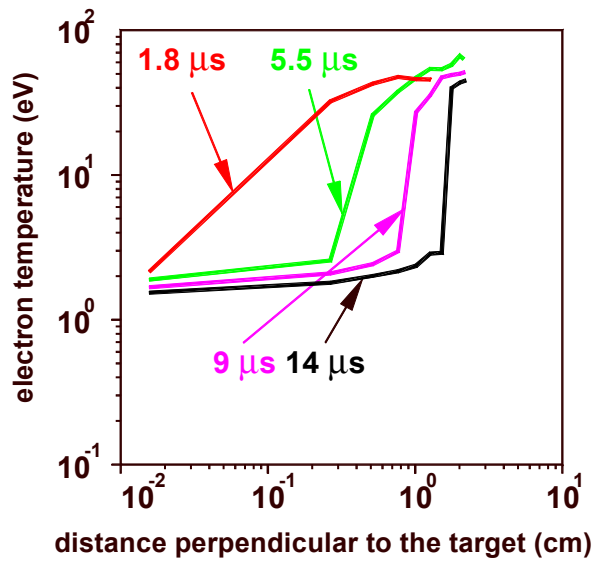


Fig. 16. Plasma temperature profiles perpendicular to the target surface starting at the SSP showing formation of the cold dense plasma layer at the MK-200 UG facility

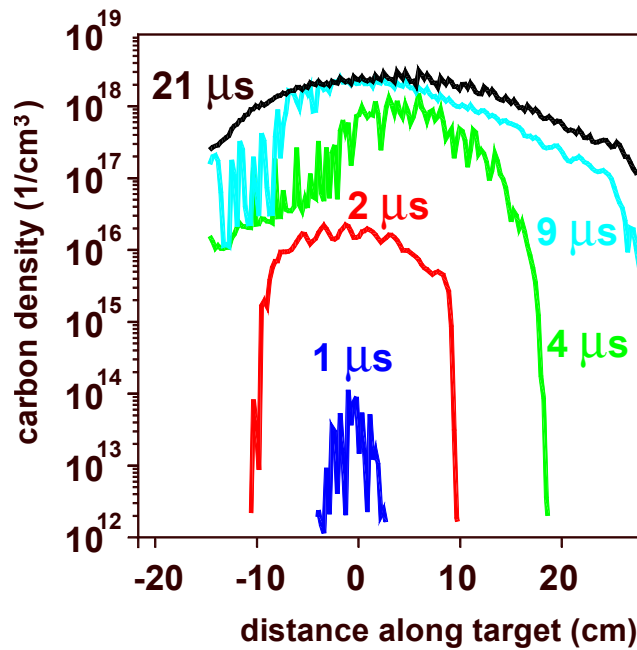


Fig. 17. Calculated profiles of carbon density at a direction perpendicular to the target at the SSP for a vertical graphite target at the MK-200 UK facility

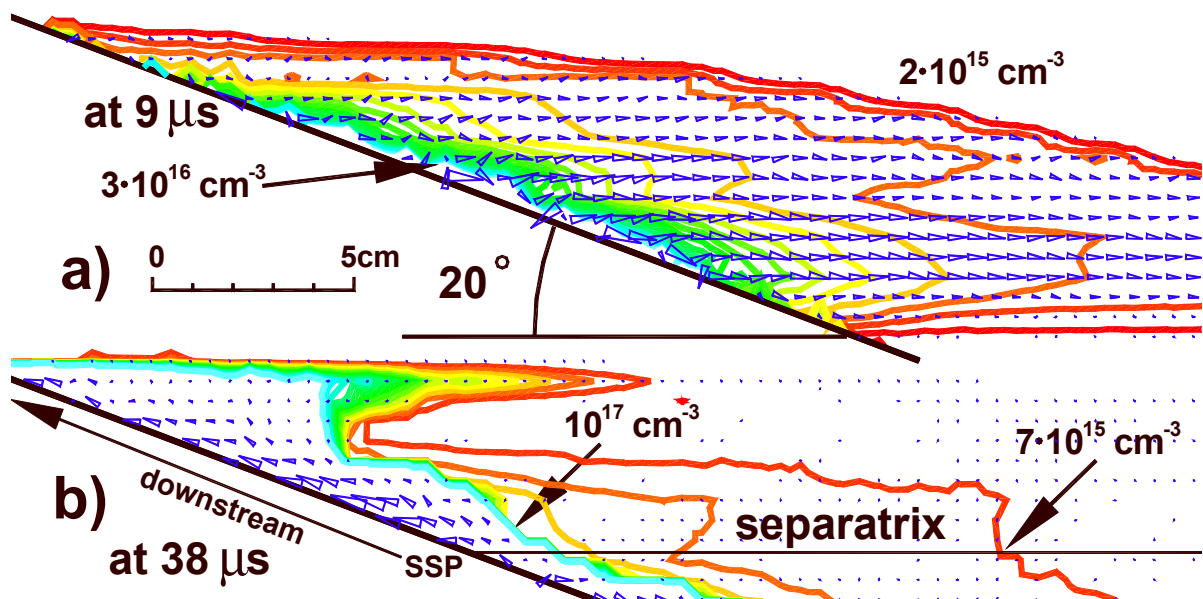


Fig. 18. Calculated plasma flow pattern (arrows show $n_c v$) and distributions of carbon density in a carbon plasma shield at the MK-200 UG facility at two time moments for a vertical graphite target and classical diffusion

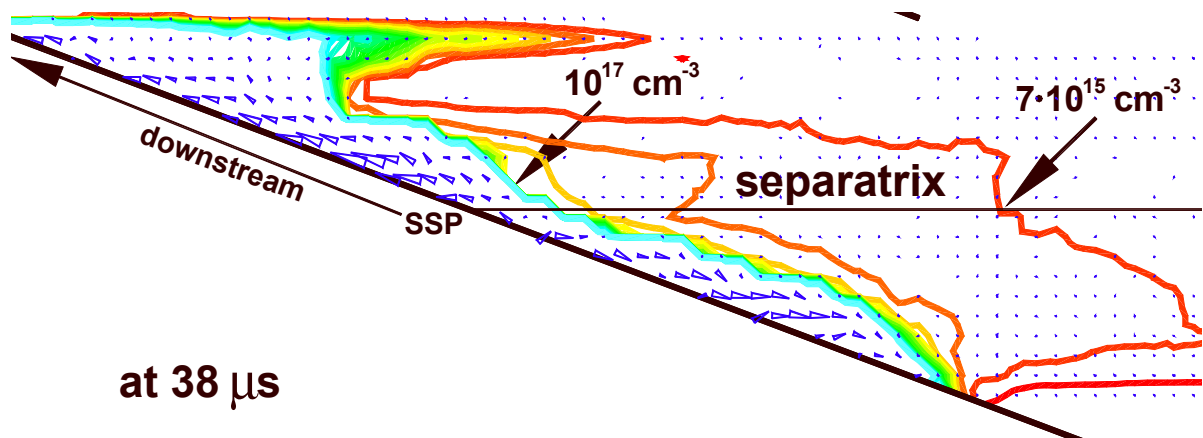


Fig. 19. Density contours and flow pattern for carbon plasma shield for a vertical graphite target showing the whole target with down- and upstream flow of plasma.

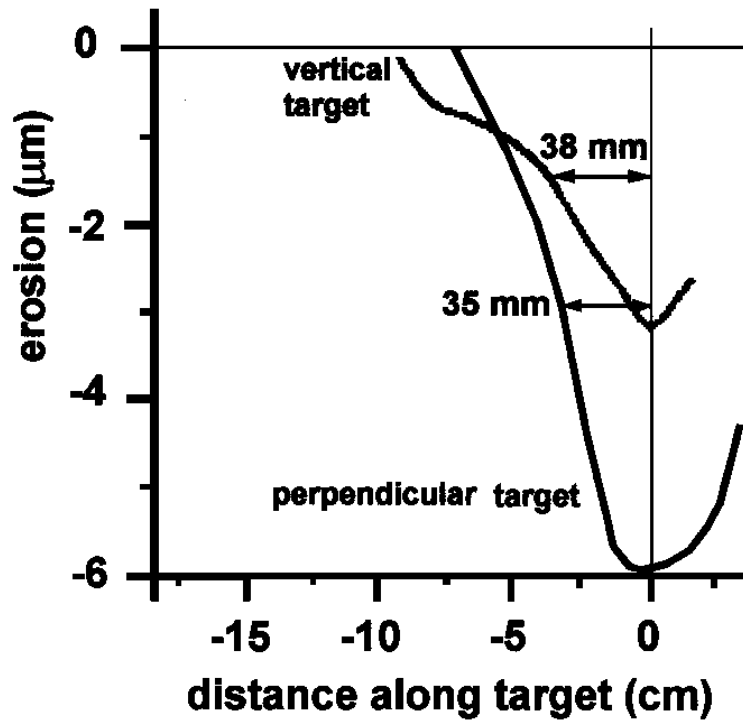


Fig. 20a. Comparison of erosion profiles measured at the MK-200 UG facility for a vertical target and a target with surface perpendicular to the impacting hot plasma after 15 shots

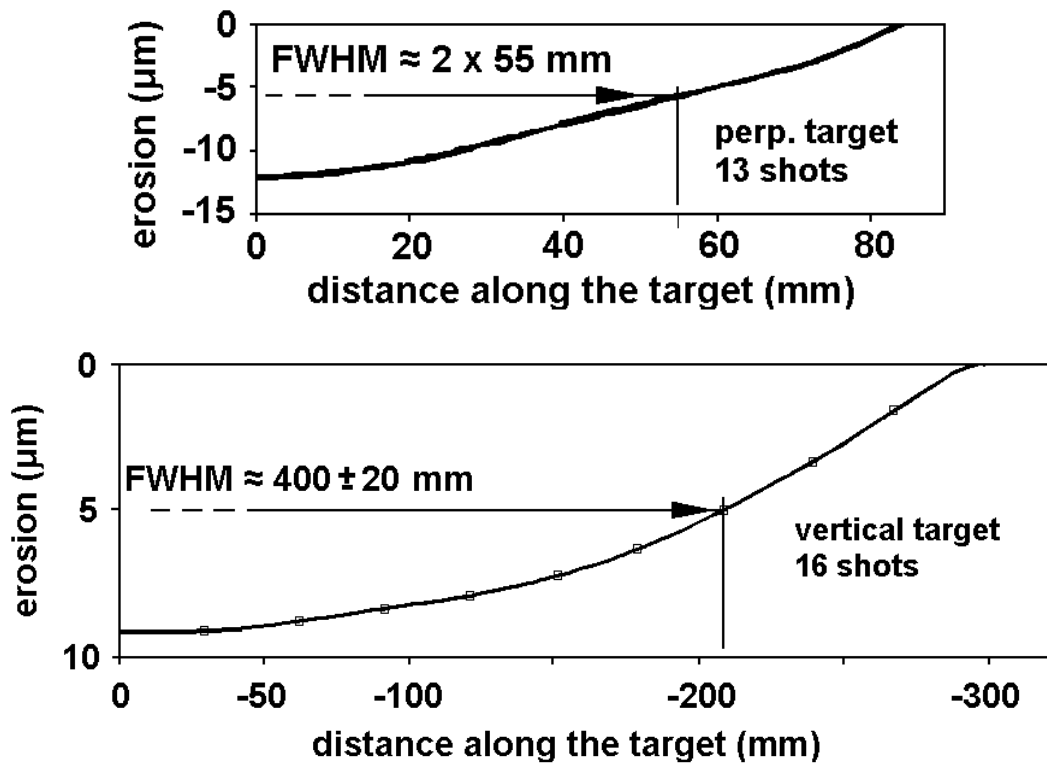


Fig. 20b. Erosion profile for quartz

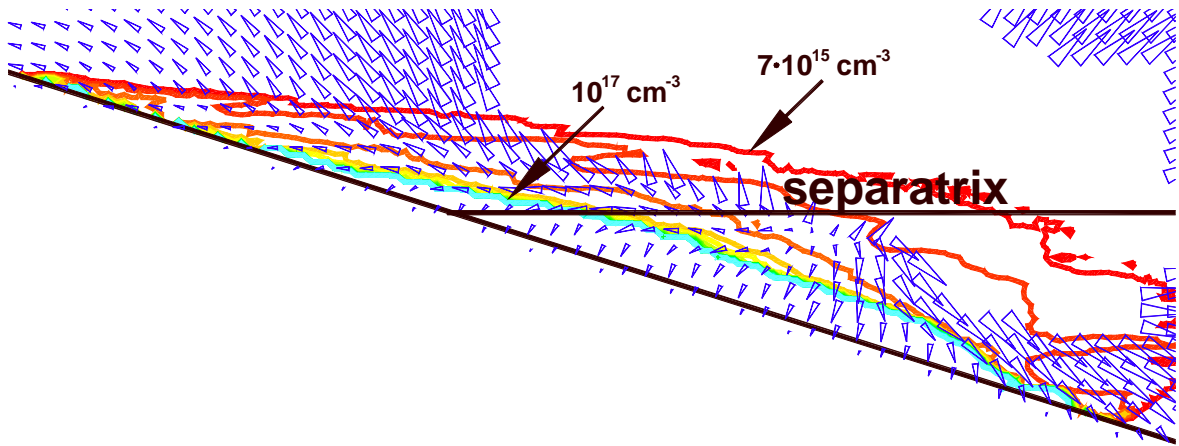


Fig. 21. Carbon density contours and angular dependence of radiation flux. The radiative target heat load originates from a radiating bubble which moves upstream with ongoing times.

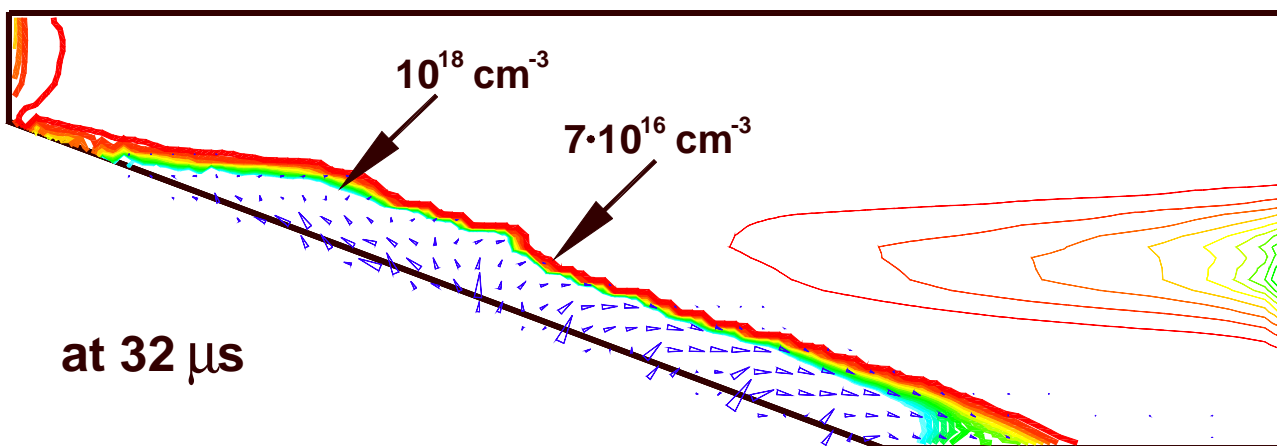
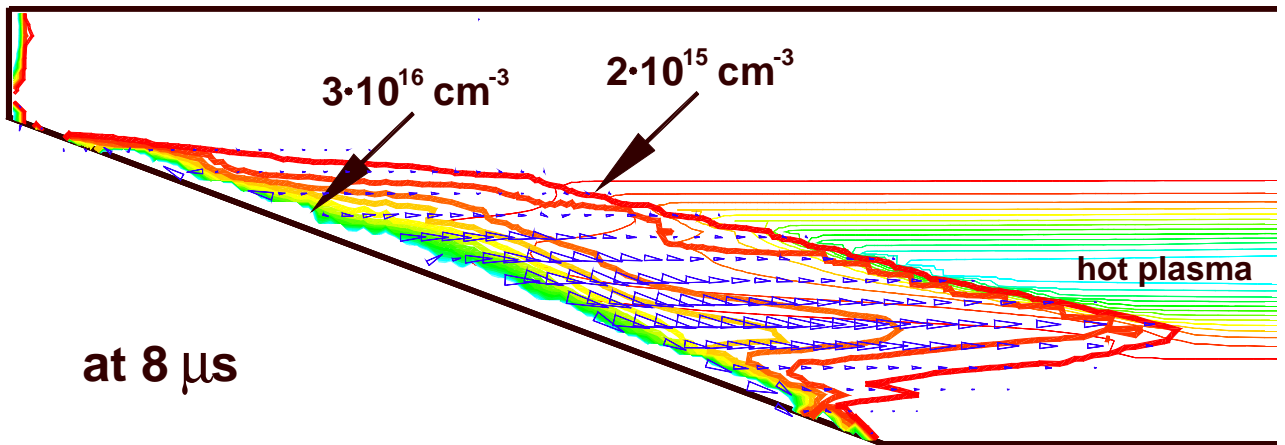


Fig. 22. Calculated plasma flow pattern (arrows) and distributions of quartz density in a quartz plasma shield at two time moments for the MK-200 UG facility.

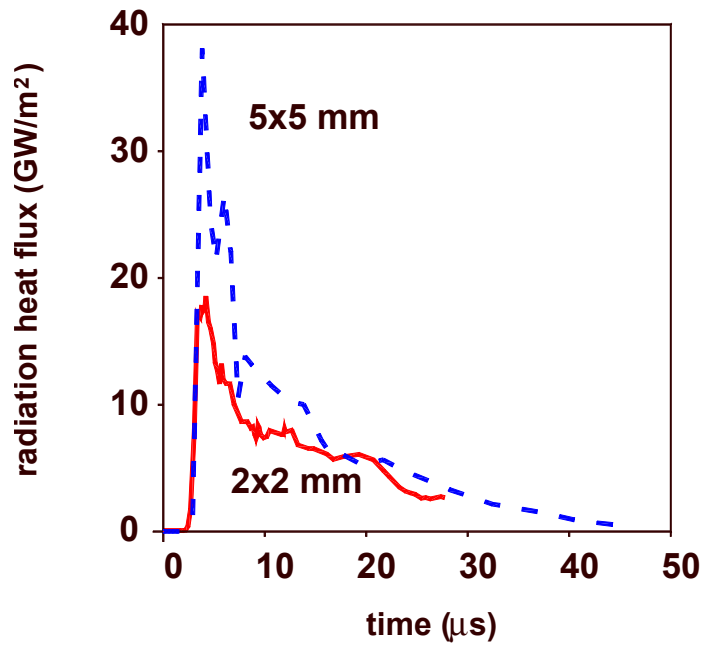


Fig. 23. Comparison of radiative target heat loads for vertical graphite target for 2x2 and 5x5 mm² meshes.

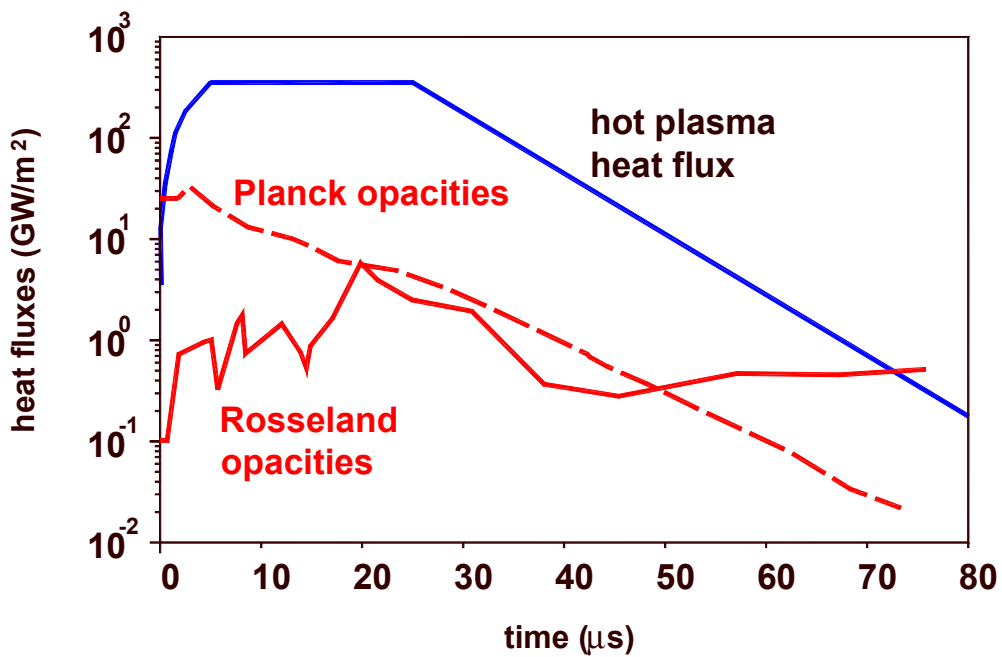


Fig. 24. Comparison of the time evolution of the peak target radiative heat load with 24 Rosseland and 69 Planck opacity groups and of the impacting hot plasma.

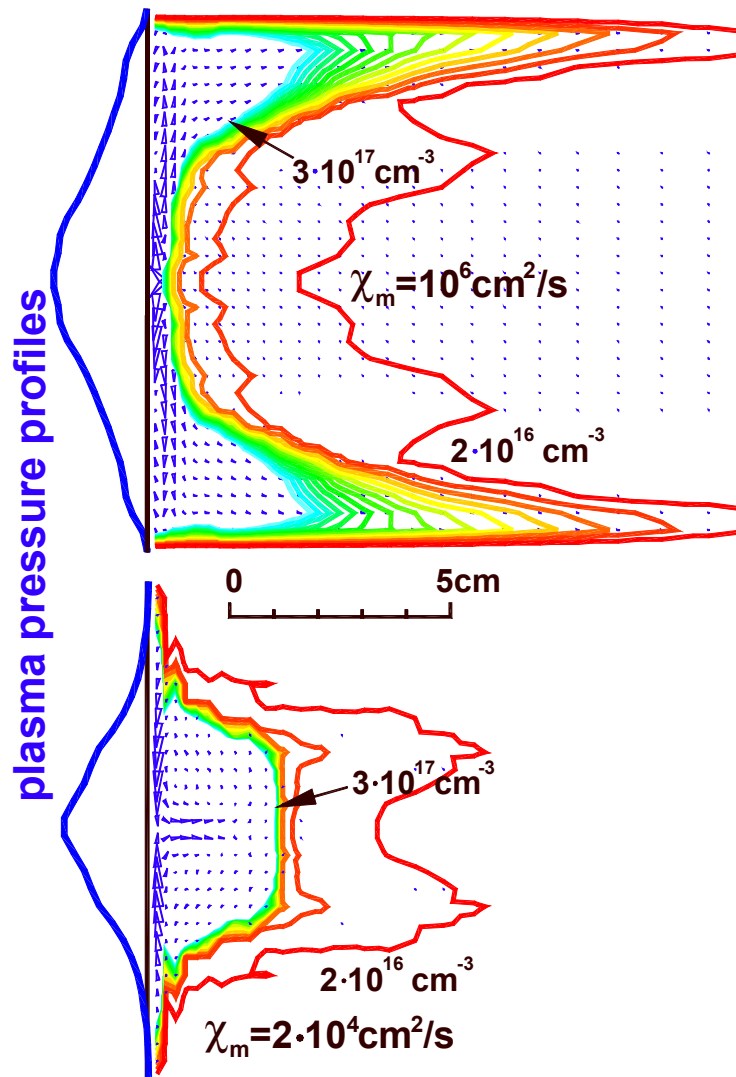


Fig.25. Flow pattern of cold plasma and electron density distributions in a carbon plasma shield at the MK-200 UG facility for classical diffusion at 30 μs for different values of the magnetic field diffusion coefficient χ_m of the target.

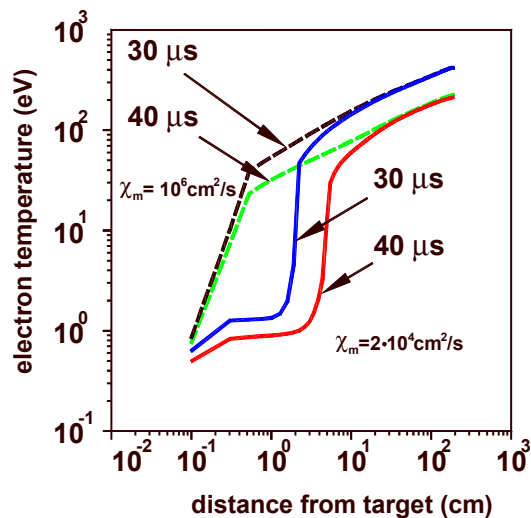


Fig. 26. Calculated electron temperature profiles along the separatrix for the two different plasma flow regimes with $\chi_m = 2 \cdot 10^4$ and $\chi_m = 10^6 \text{ cm}^2/\text{s}$ at the MK-200 UG facility.

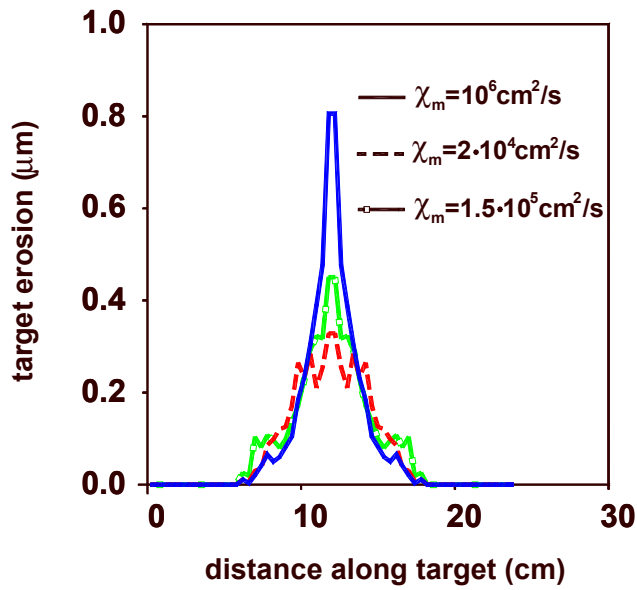


Fig.27. Calculated erosion profiles for a perpendicular graphite target for 3 different values of the magnetic field diffusion coefficient χ_m of the target at the MK-200 UG facility.

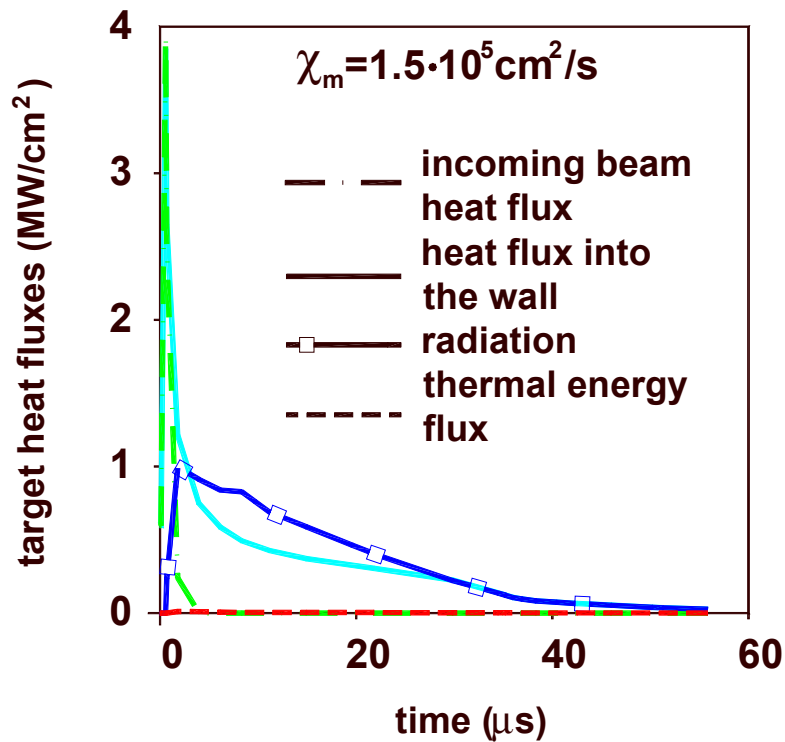


Fig. 28. Calculated target heat fluxes for a perpendicular graphite target at the separatrix strike point at the MK-200 UG facility.

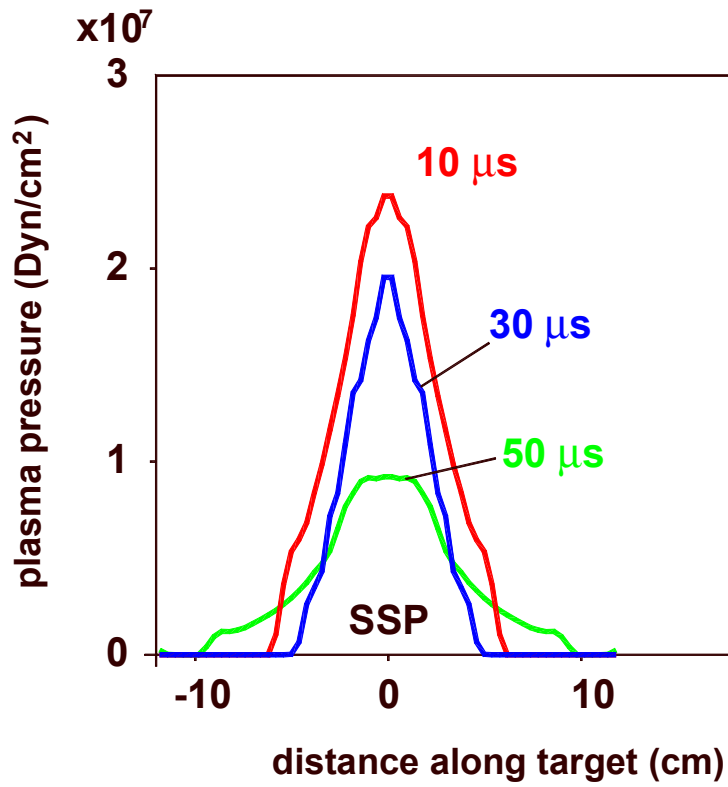


Fig. 29. Plasma shield pressure close to the target.

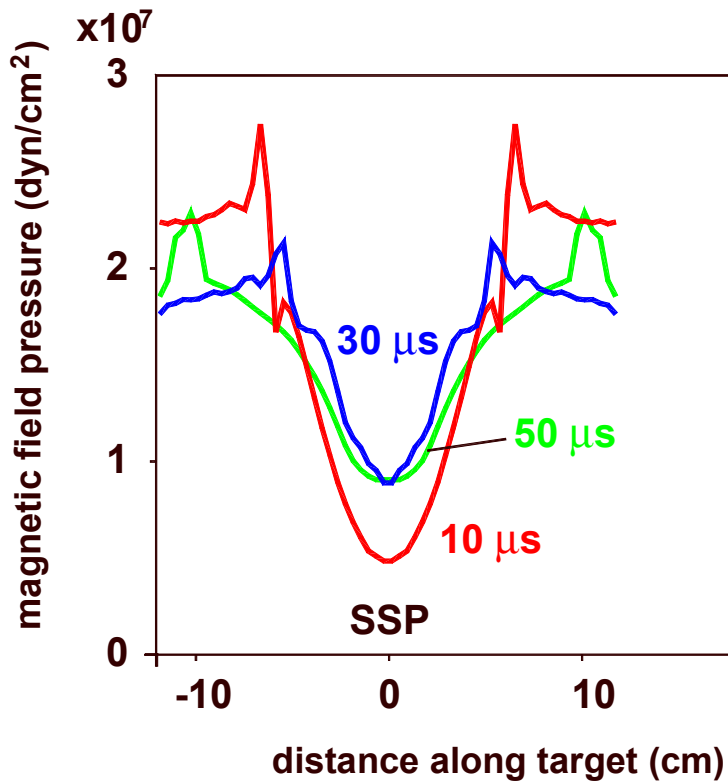


Fig. 30. Time evolution of the pressure of the poloidal magnetic field B_x .

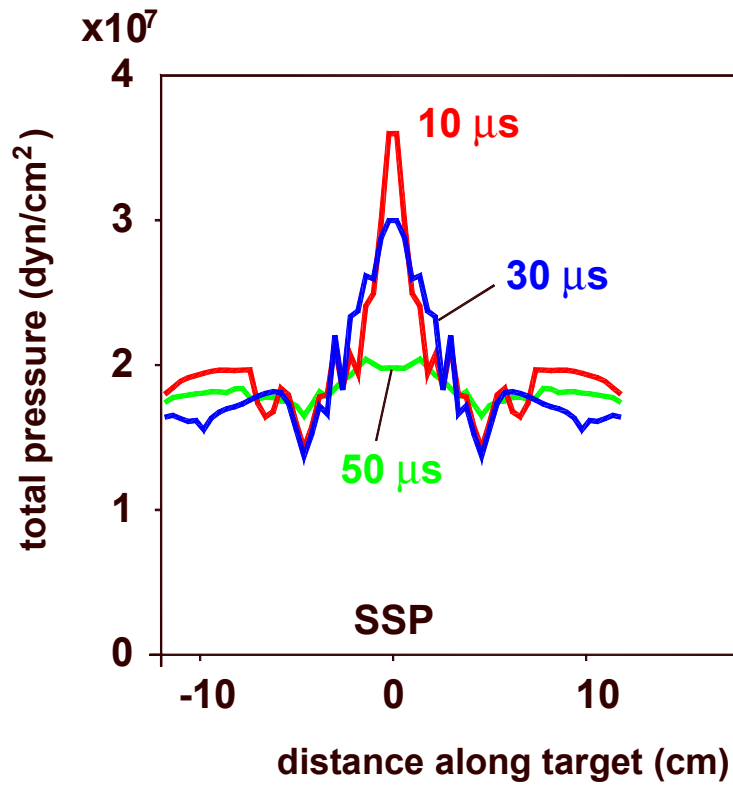


Fig. 31. Time evolution of the total pressure.

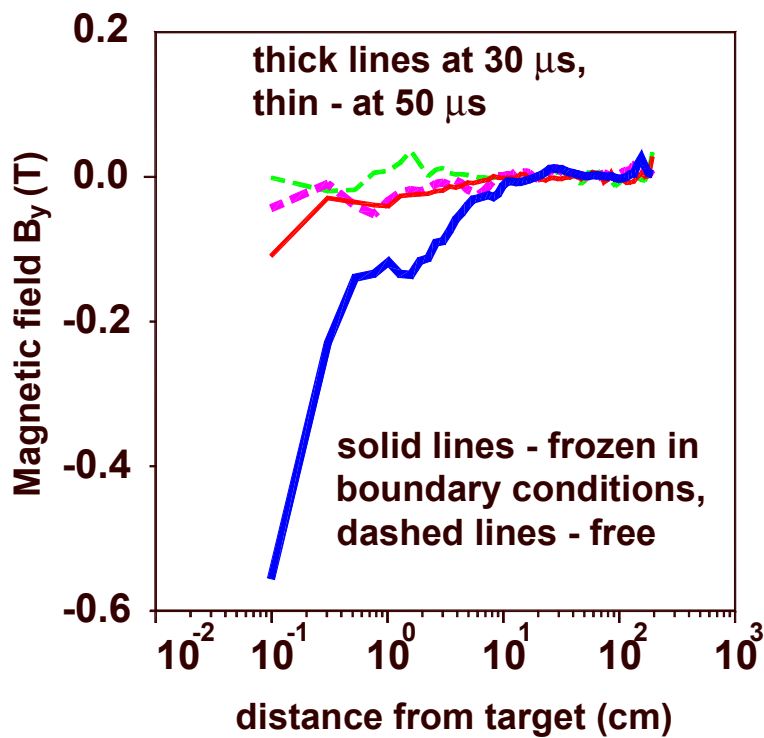


Fig.32. B_y component of magnetic field below the separatrix for the 2 different boundary conditions.

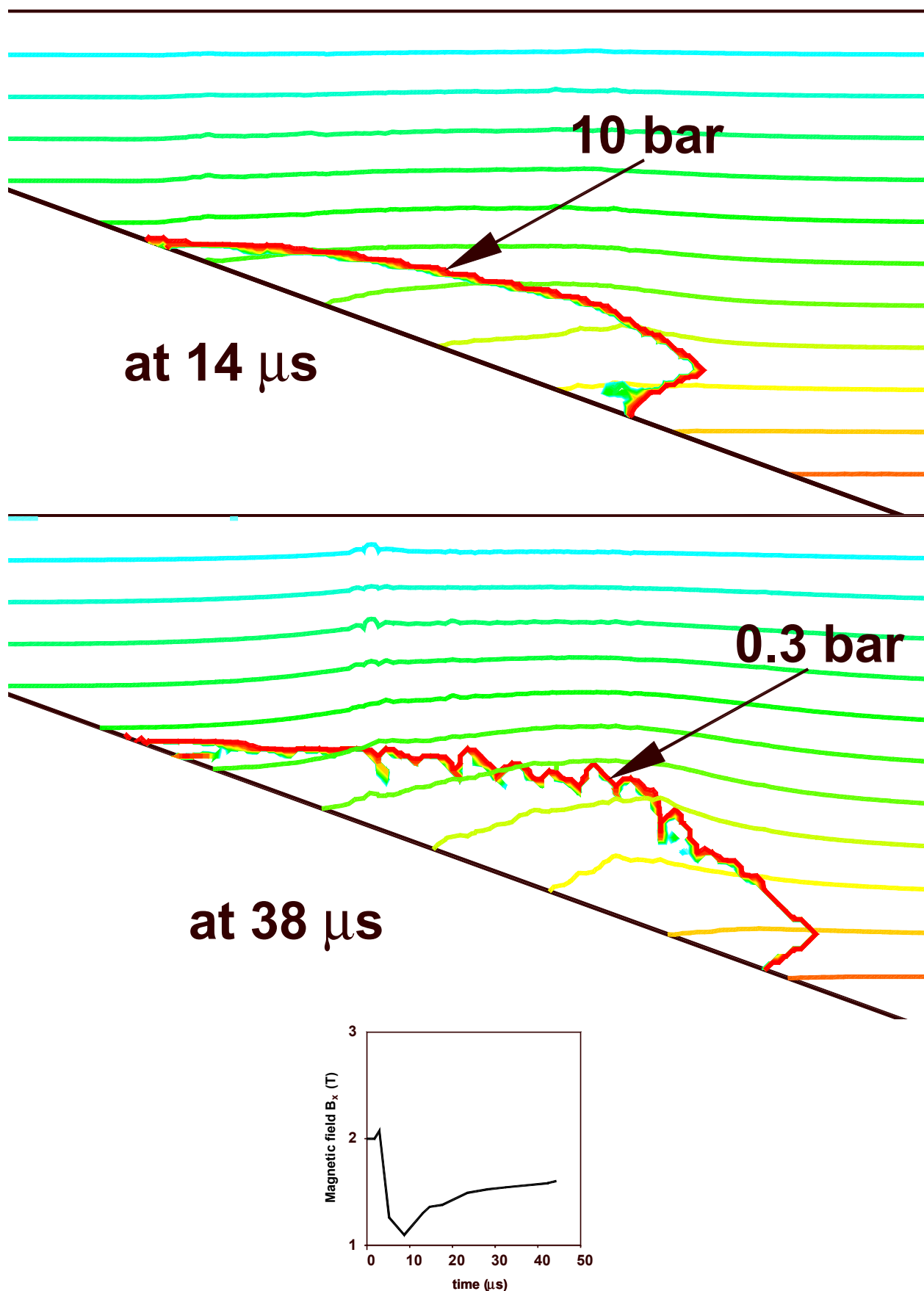


Fig. 33. Time evolution of the poloidal magnetic field $B_x(t)$ with $B_x(0)=2\text{T}$ in the carbon plasma shield of a vertical target for the conditions of the MK-200 UG facility. The plasma shield is indicated as pressure contour.

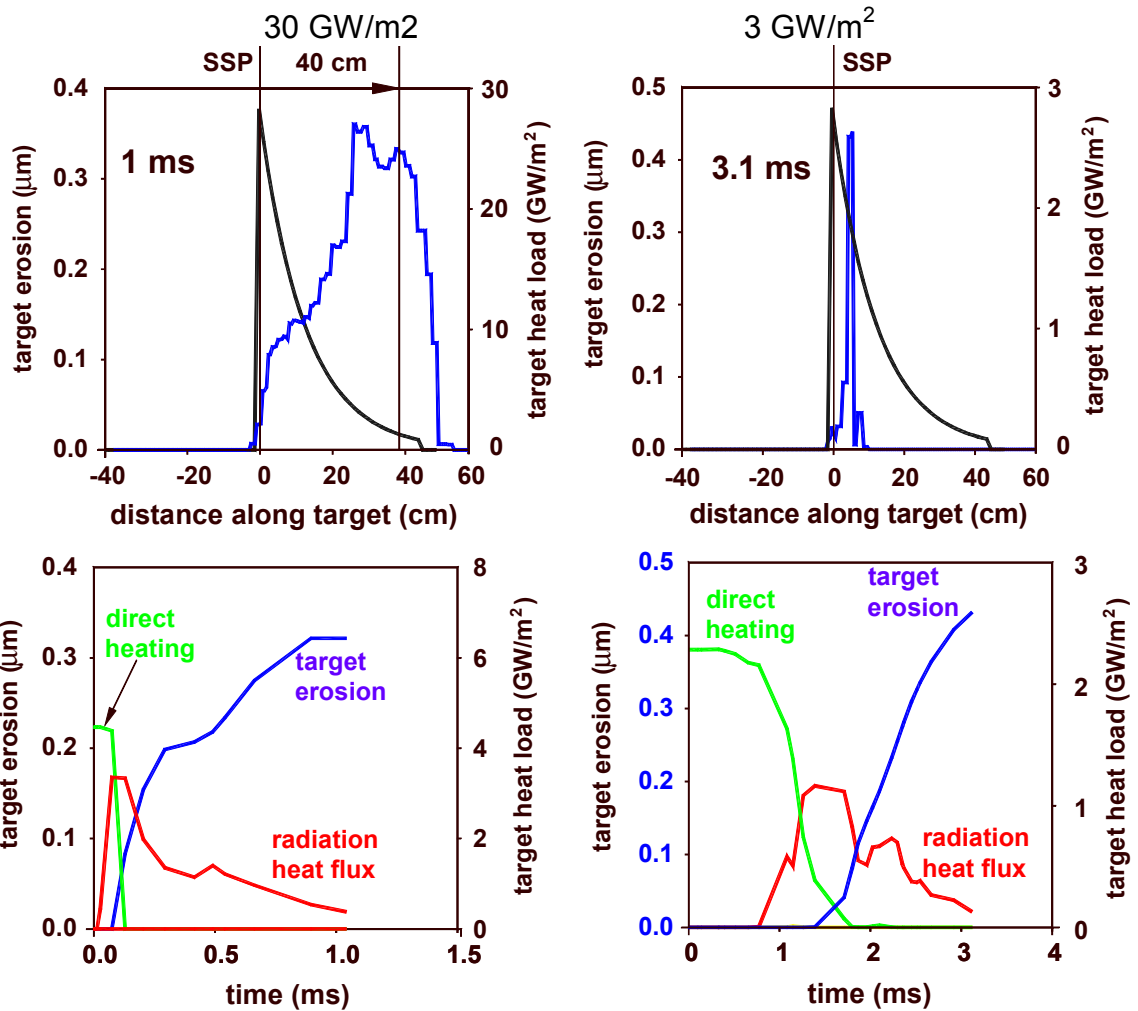


Fig.34. Erosion and time evolution of target heat loads for ITER-FEAT vertical tungsten targets for downstream SSP for the 2 different target heat loads 3 and 30 GW/m²

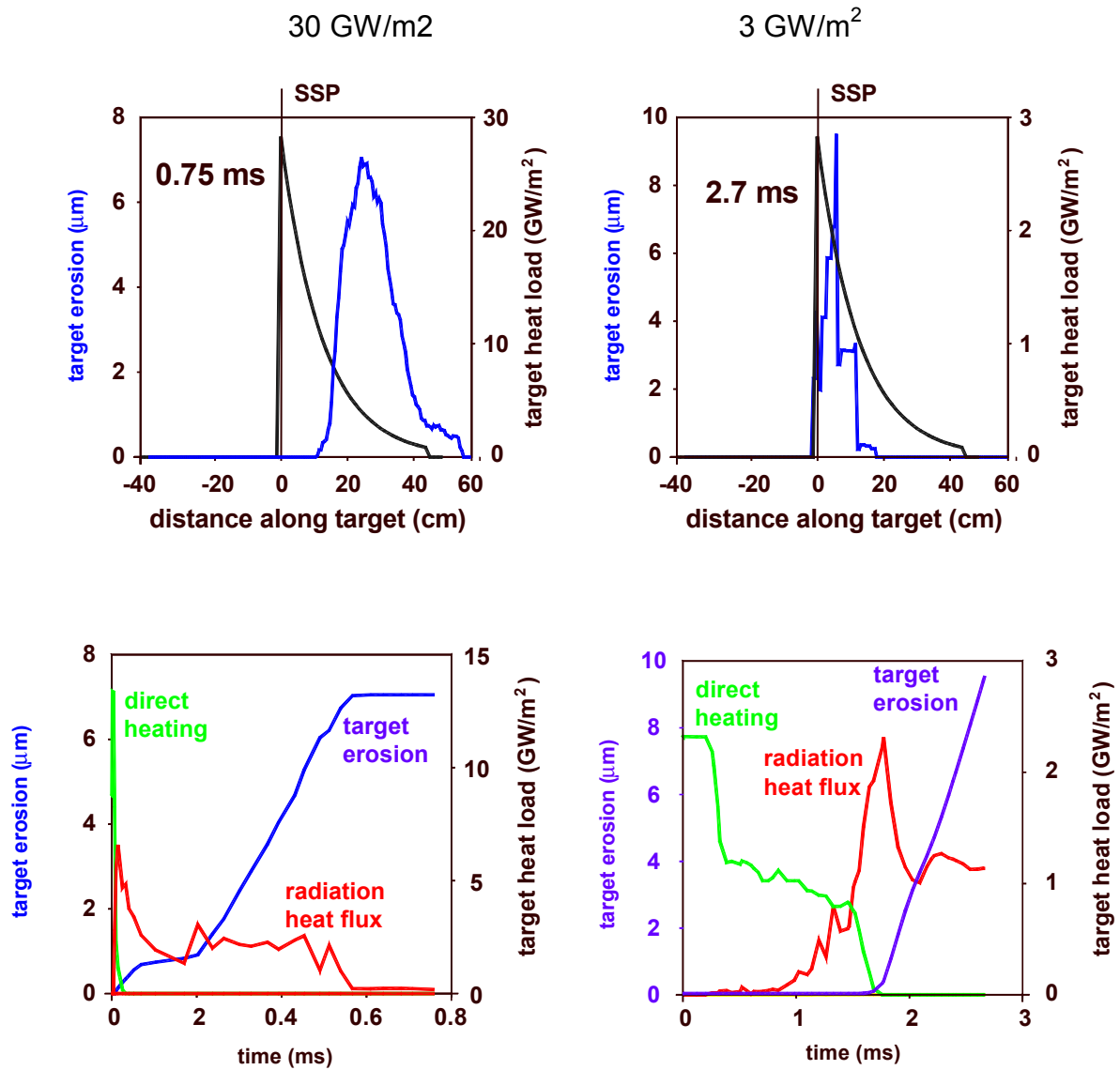


Fig. 35. Erosion and time evolution of target heat loads for ITER FEAT vertical graphite targets for downstream SSP.

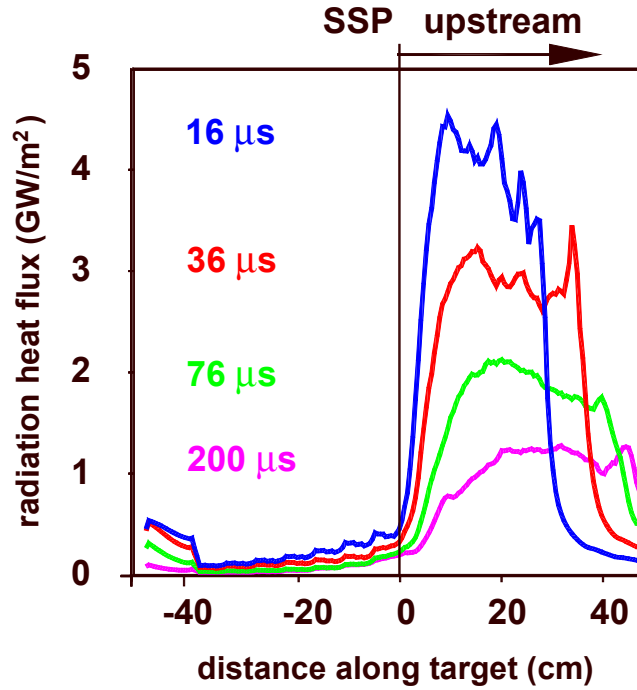


Fig. 36. Radiative target heat load profiles and time dependent upstream shift of the radiation profiles for vertical tungsten target for downstream SSP and ITER FEAT conditions with peak target heat load of 30 GW/m^2 .

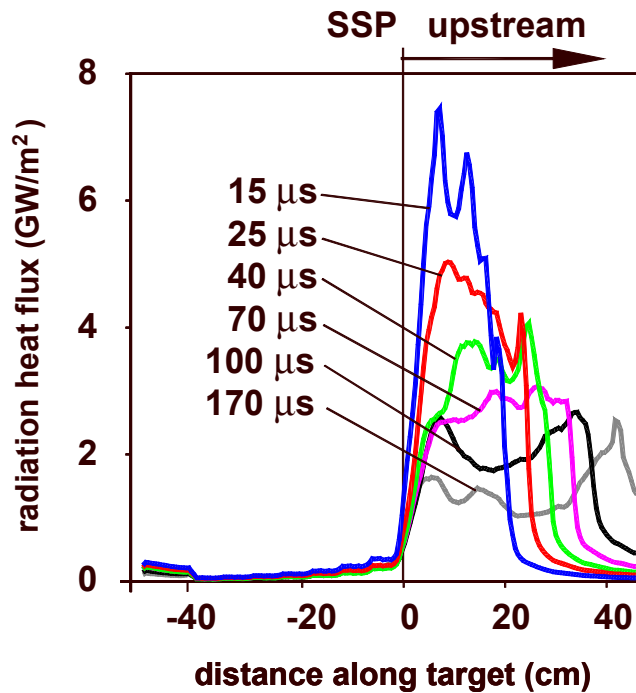


Fig. 37. Radiative target heat load profiles and time dependent upstream shift of the radiation profiles for vertical graphite target for downstream SSP and ITER FEAT conditions with peak target heat load of 30 GW/m^2 .

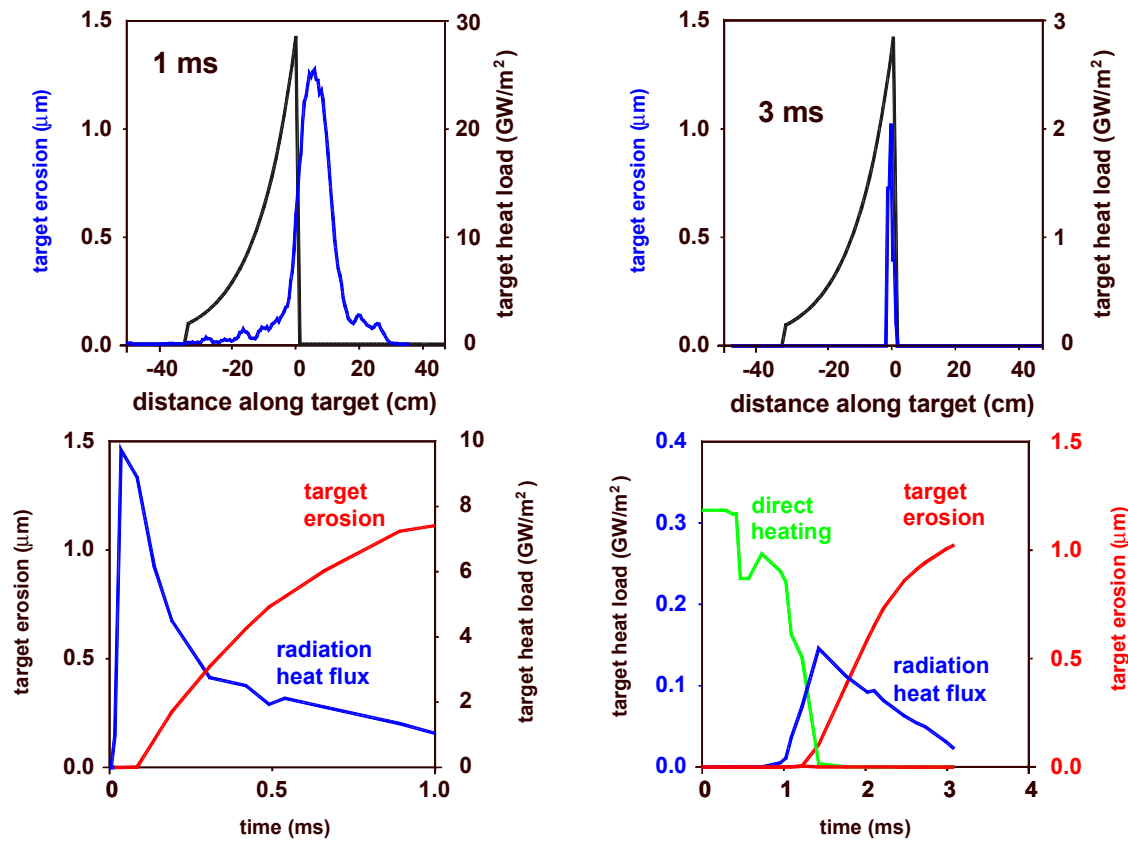


Fig. 38. Erosion and time evolution of target heat fluxes for a vertical tungsten dome target (upstream SSP) for the two different target heat loads 3 and 30 GW/m².

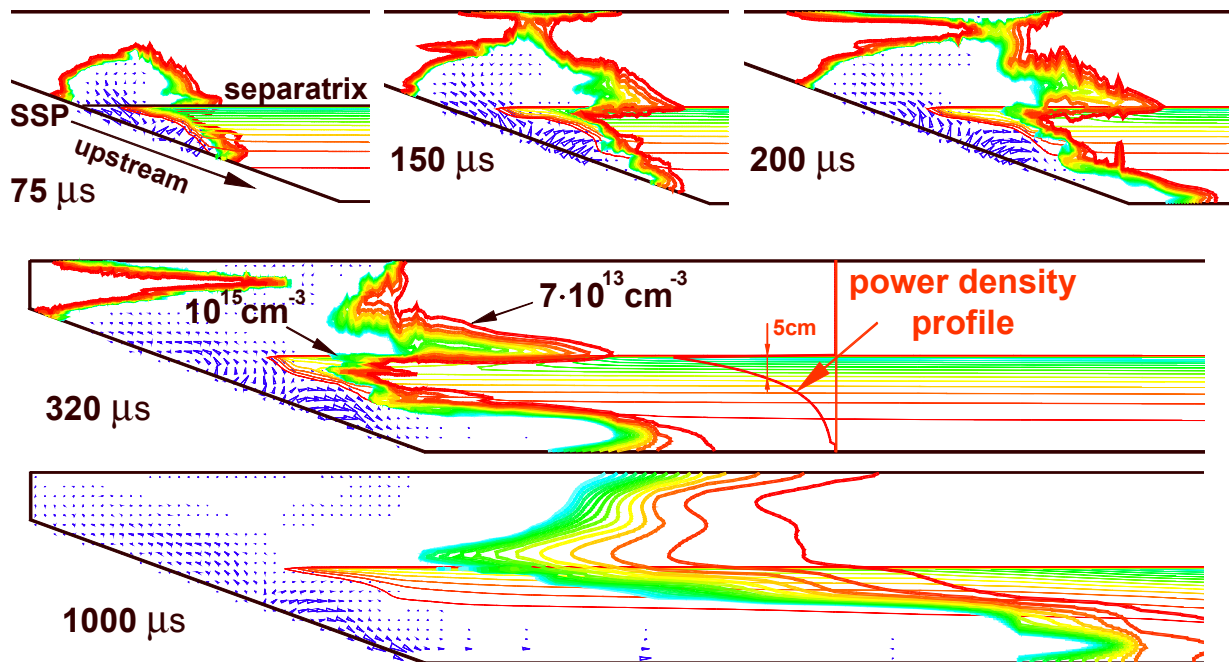


Fig. 39. Time evolution of carbon plasma shield from vertical graphite target with downstream separatrix. Shown are plasma density contours, particle fluxes (nv) and incoming power density profile. Peak target heat load is 30 GW/m².

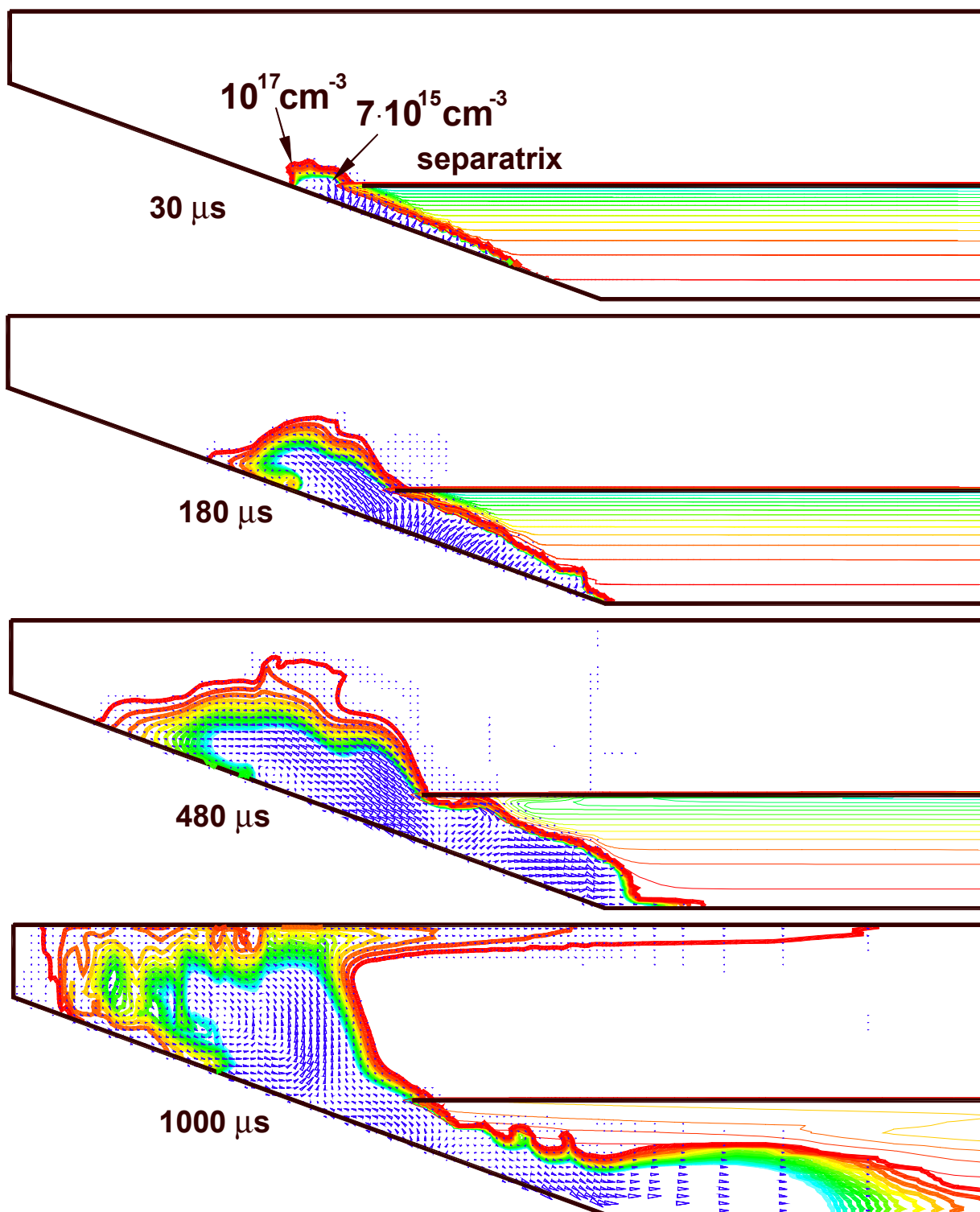


Fig. 40. Time evolution of tungsten plasma shield from vertical tungsten target with downstream separatrix. Peak target heat load is 30 GW/m^2 . The plasma flow pattern is rather comparable to that one for graphite.

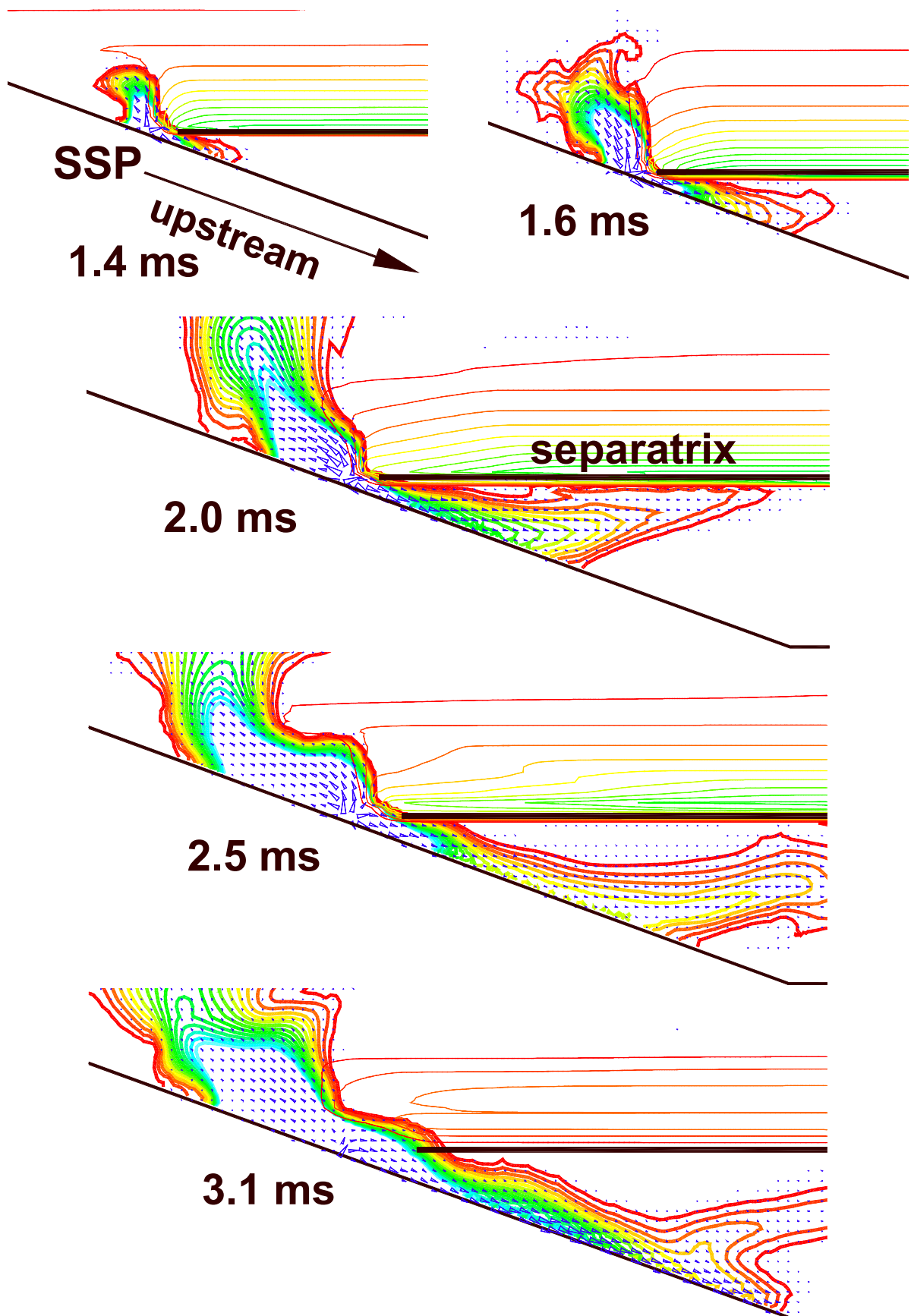


Fig. 41. Time evolution of tungsten plasma shield from vertical tungsten dome target with separatrix upstream. Peak target heat load is 3 GW/m^2 . Evaporation starts after about 1.4 ms. Initial target temperature is 1000 K.

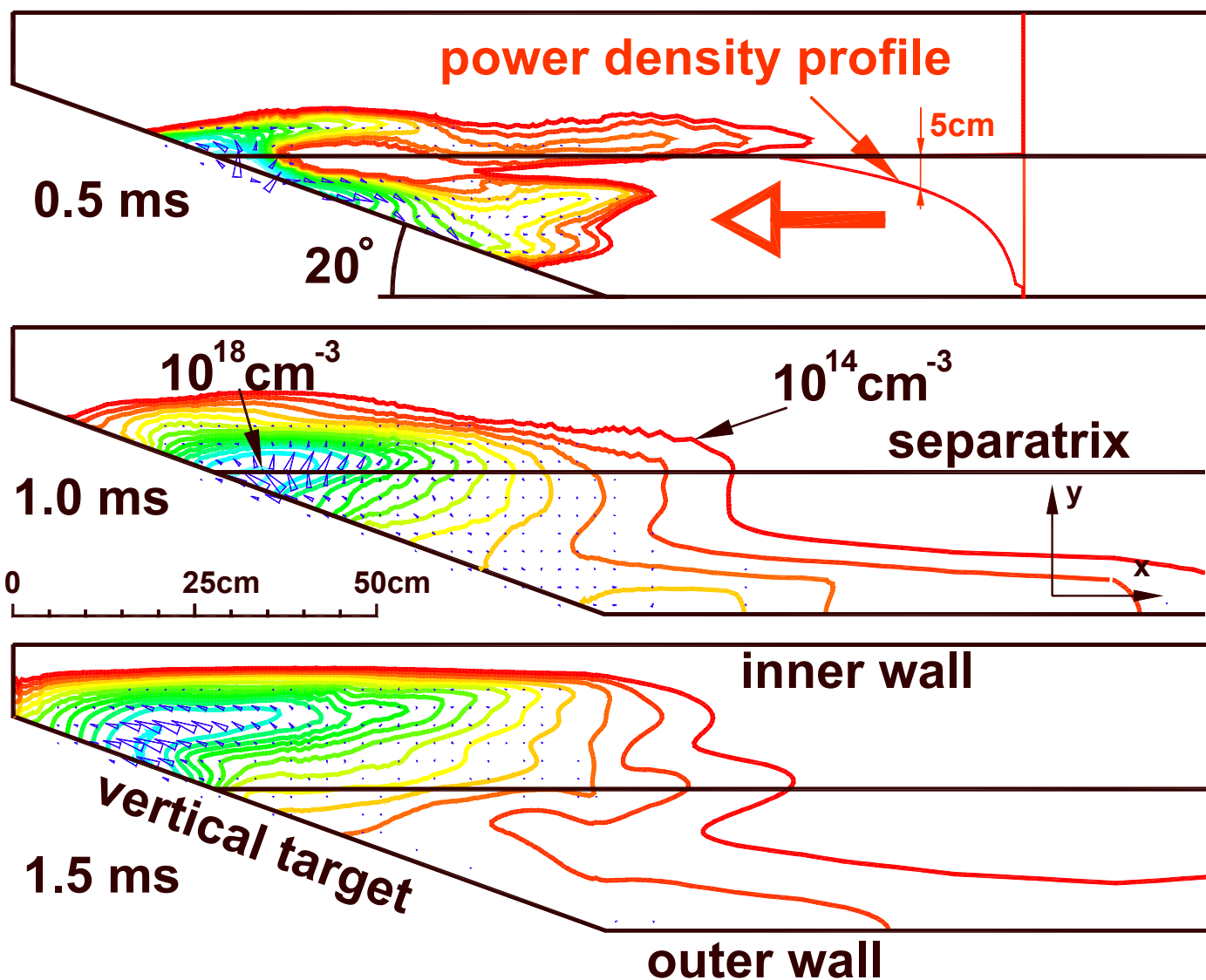


Fig. 42. Impurity production from heating of graphite hot spots during an ELM with energy of 0.5 MJ/m^2 and a time duration of 0.5 ms and evolution of carbon densities in the range from 10^{14} to 10^{18} cm^{-3} in the plasma shield and of the plasma flow pattern after end of heating.

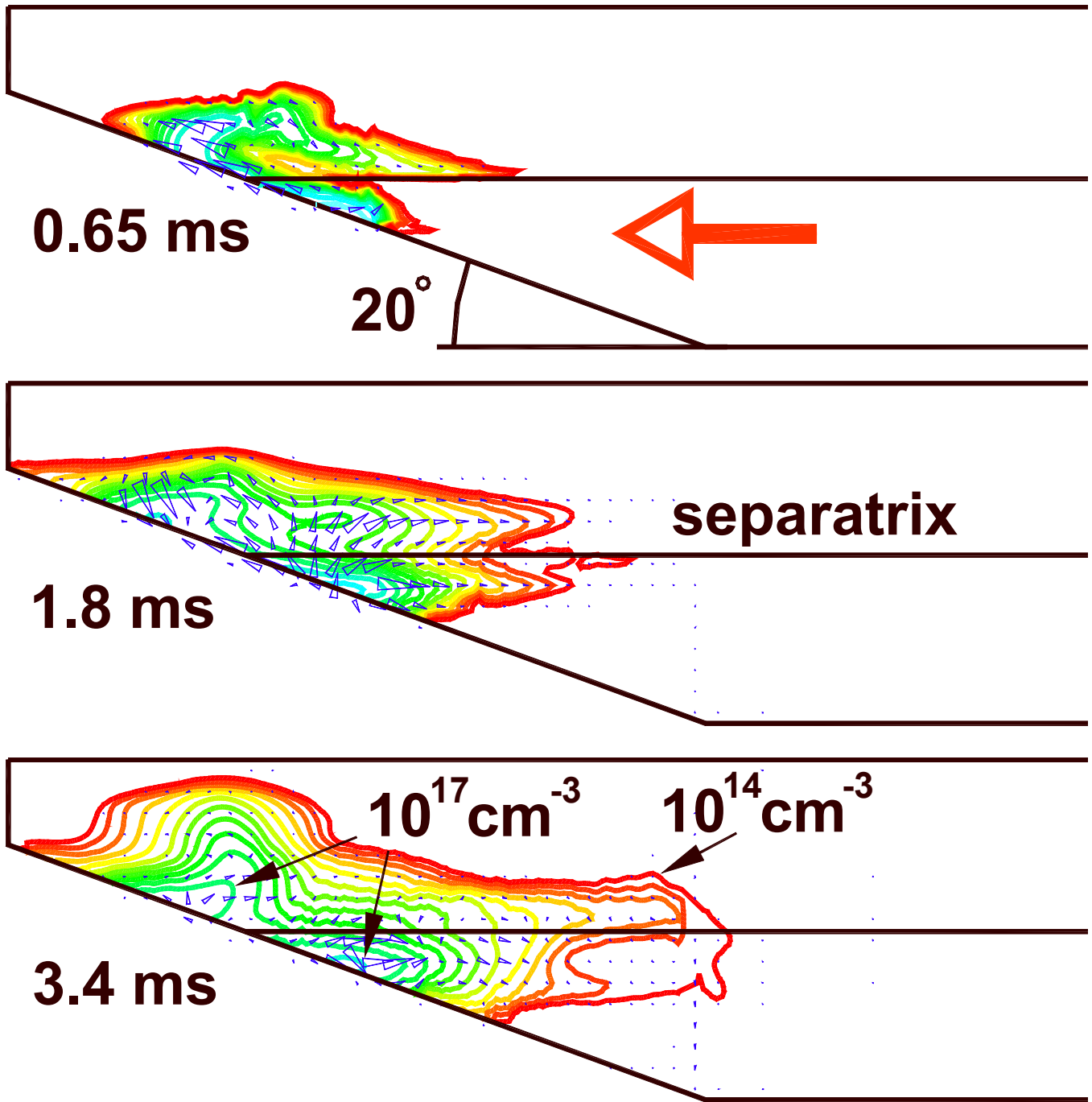


Fig. 43. Impurity production from heating of tungsten hot spots during the same ELM as of Fig. 42 and evolution of tungsten densities and flow pattern in the plasma shield after end of heating.

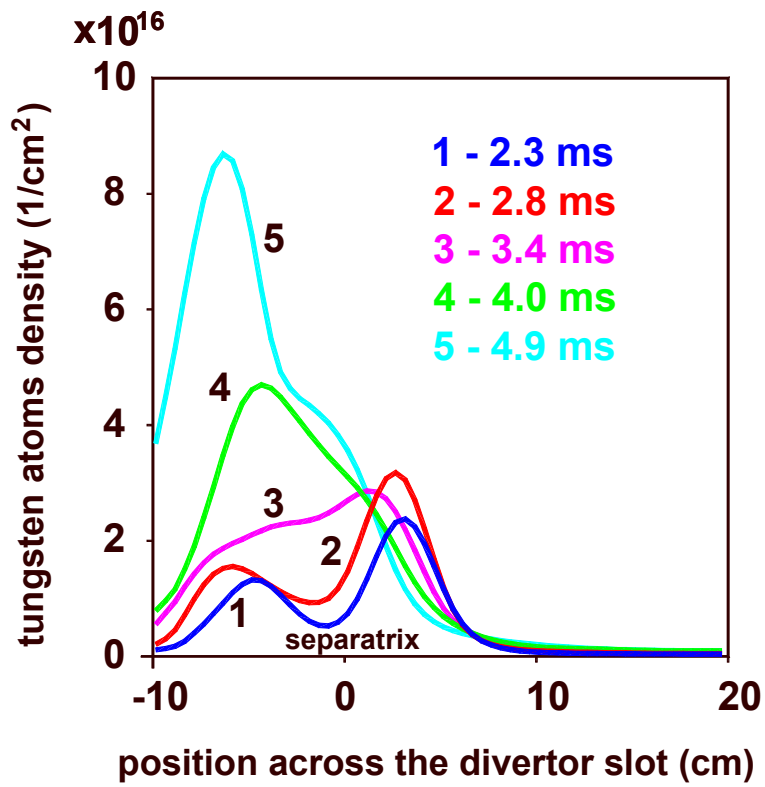


Fig. 44. Time evolution of the total number of tungsten atoms across a divertor leg within a 0.5 to 1.2 m distance from the separatrix strike point per 1cm of toroidal length. The outer wall is at -20cm.

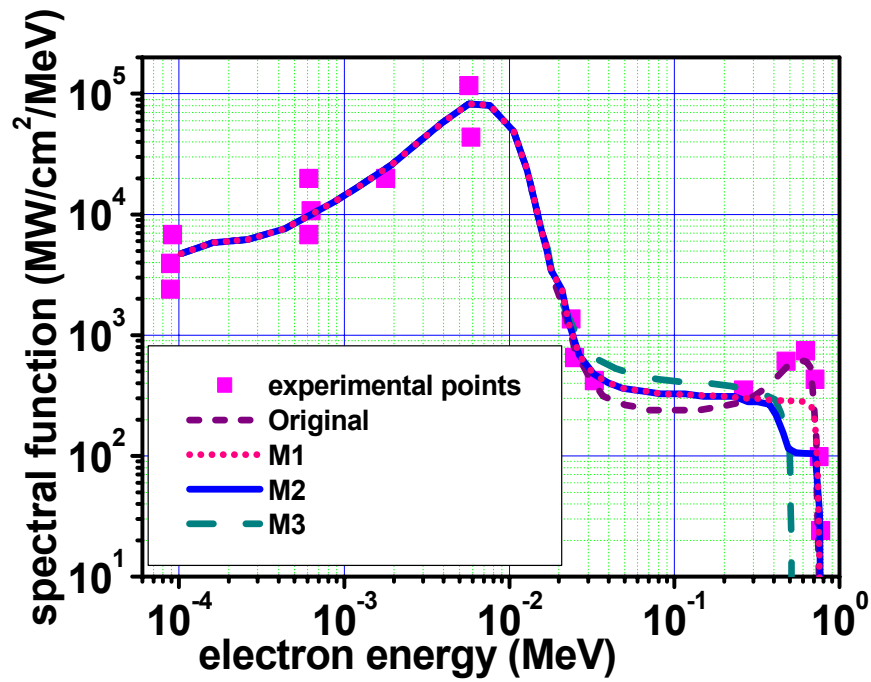


Fig. 45a. Flux spectrum of the GOL-3 electron beam showing experimental points together with 4 different spectral functions used in the numerical analysis

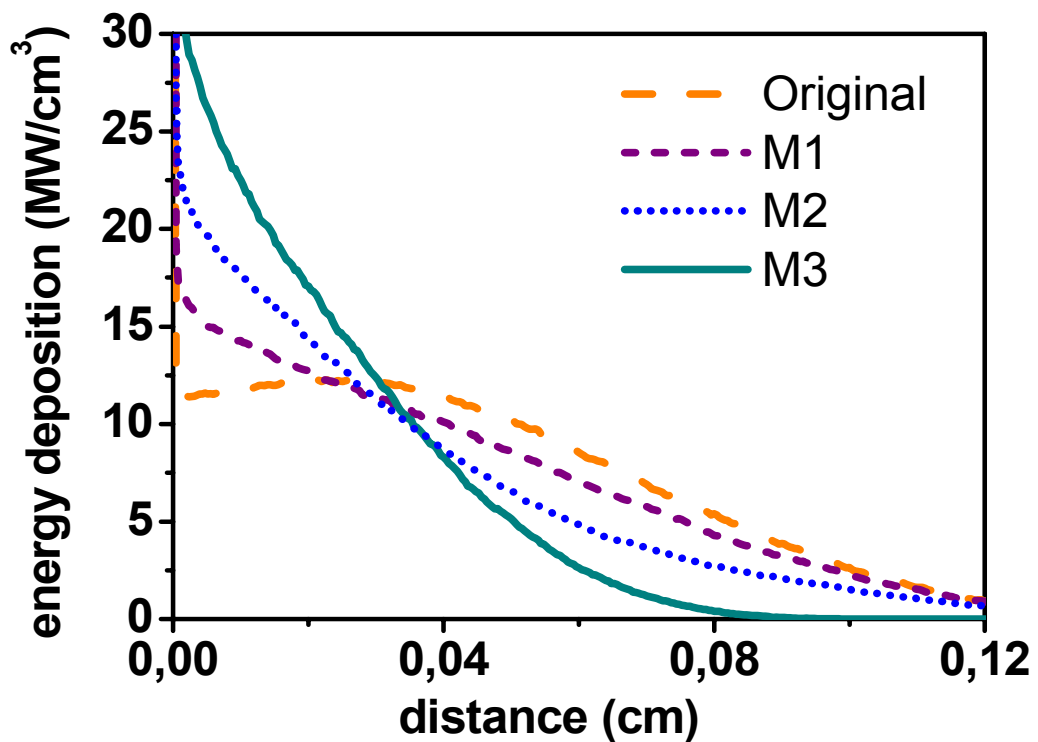


Fig. 45b. Energy deposition into graphite calculated by 3-D Monte Carlo for the 4 spectral functions from Fig. 45a. The curves are normalized to 10 GW/m^2

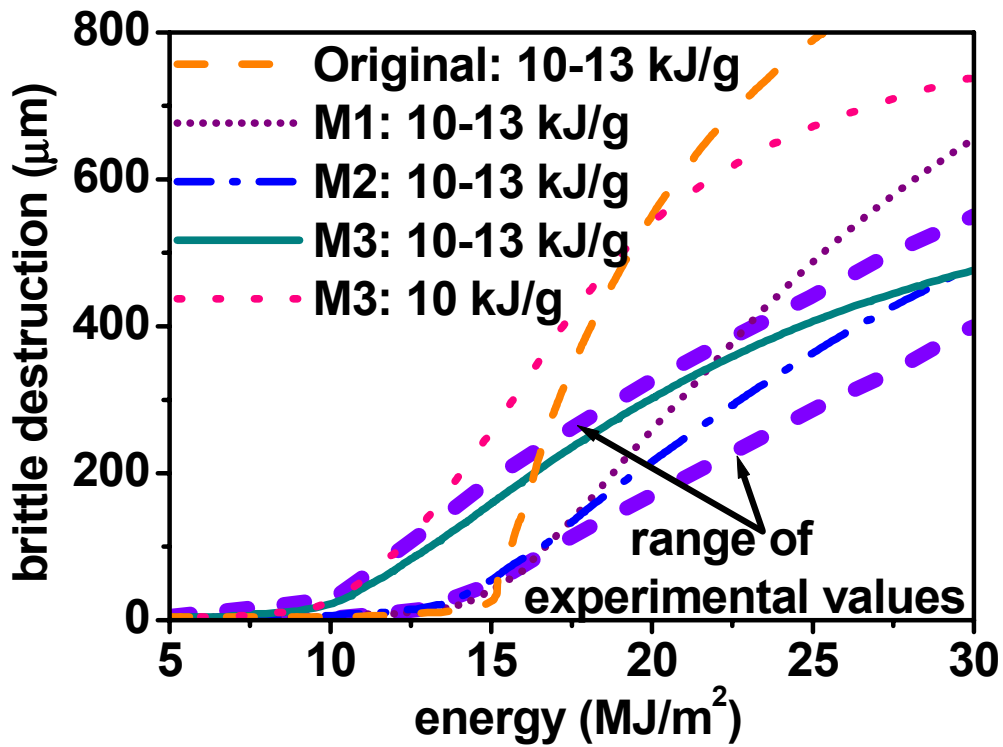


Fig. 46. Comparison of erosion calculated for the different energy deposition profiles of Fig. 1b with the experimental erosion values

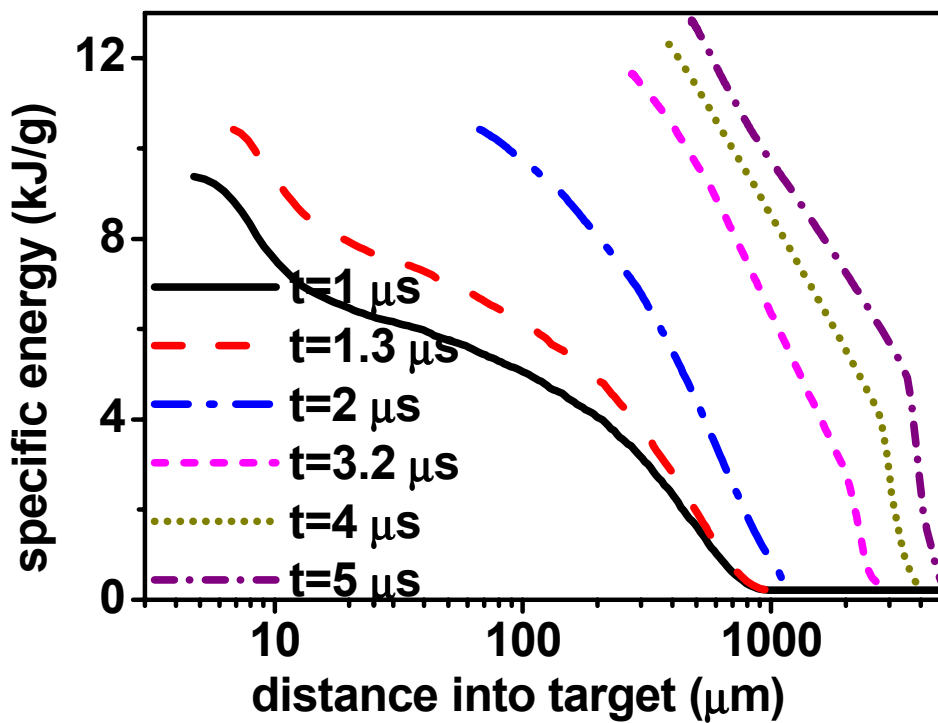


Fig. 47. Typical profiles of deposited energy in the bulk graphite using the spectral flux profile M3 and a damage threshold value from 10 to 13 kJ/g

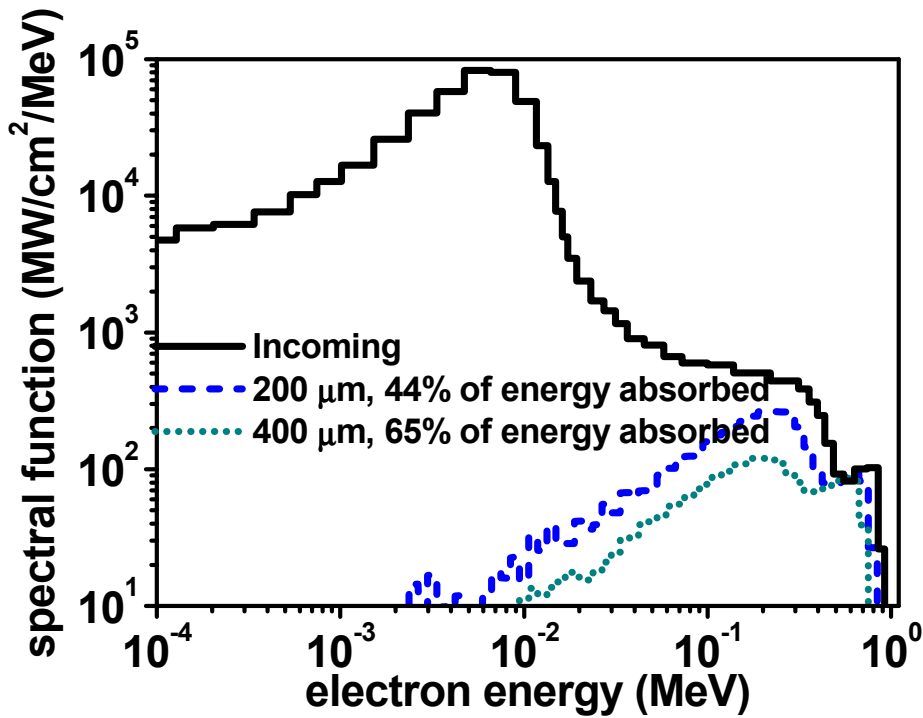


Fig. 48. Flux distribution of incoming electrons and of electrons transmitted through 2 layers of graphite of different thickness

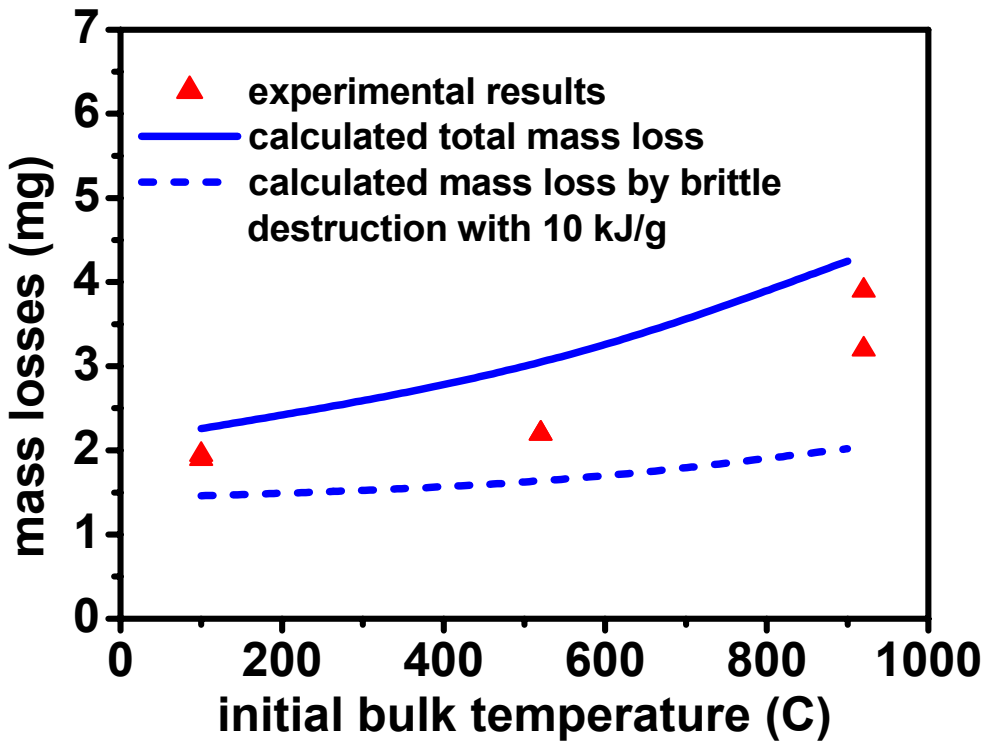


Fig. 49a. Comparison of measured and calculated temperature dependence of total mass loss for CFC graphite for JEBIS conditions with 70 keV e-beam with perpendicular impact, pulse duration 2 ms, absorbed heat flux 1.8 GW/m².

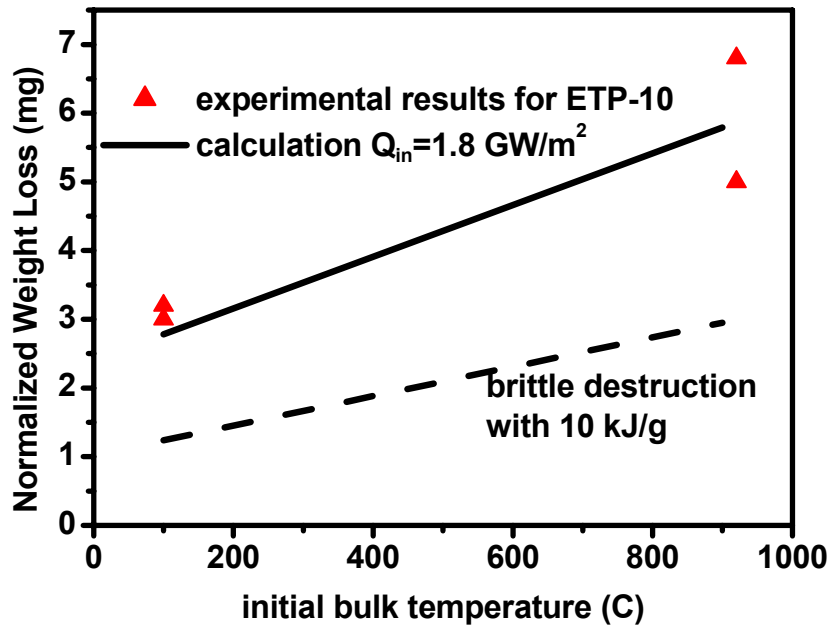


Fig. 49b. Comparison of measured and calculated temperature dependence of total mass loss for ETP-10 fine grain graphite for JEBIS conditions with 70 keV e-beam pulse duration 2ms, absorbed heat flux 1.8 GW/m^2

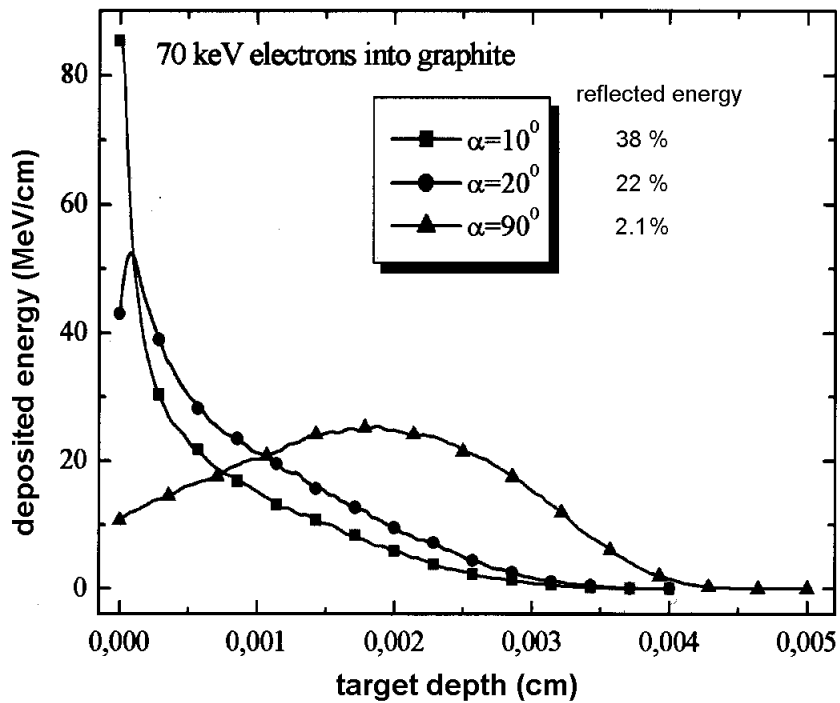


Fig.50 Energy deposition by monoenergetic electrons of energy of 70 keV into graphite with α the impact angle

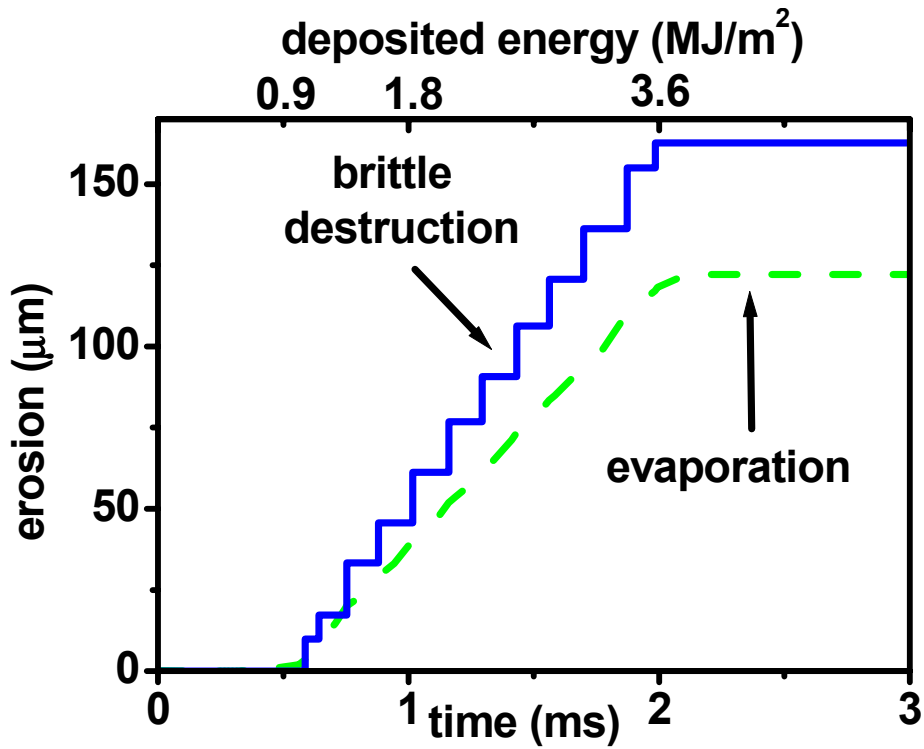


Fig. 51. Calculated erosion rates by evaporation and brittle destruction for JEBIS conditions for fine grain graphite. Initial temperature of the sample is 1200 K.

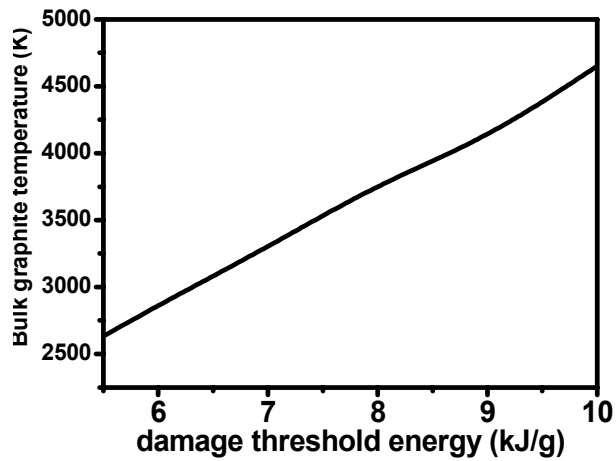


Fig.52. Damage threshold energy and related bulk graphite temperature.

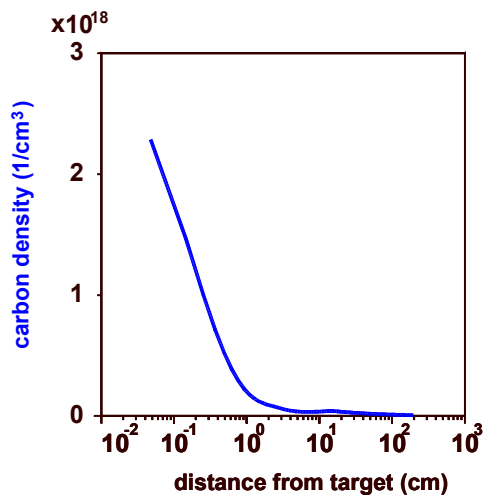
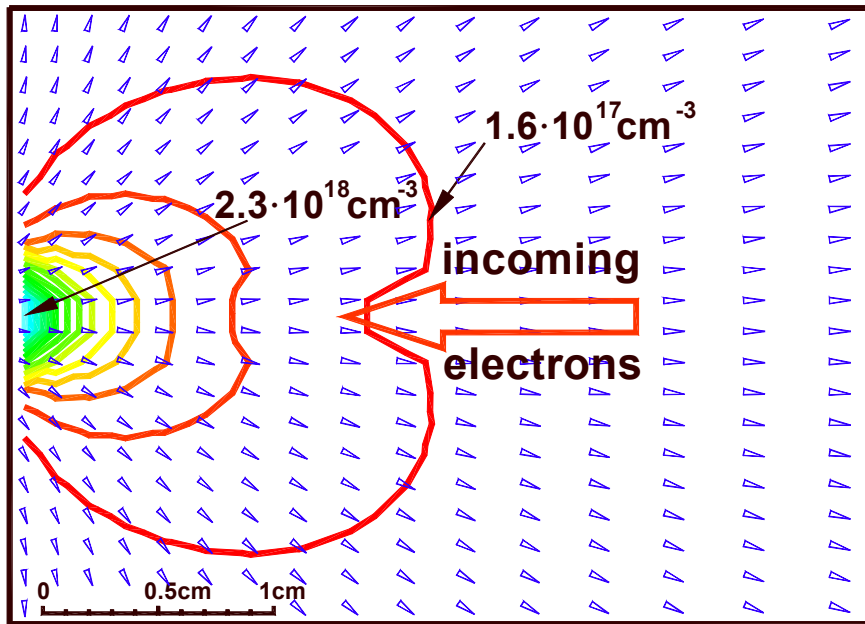


Fig. 53. Expansion of the ablated material into vacuum. The arrows indicate the particle flow Γ with $\Gamma = N_c v$, the lines show carbon density contours for indicated densities.

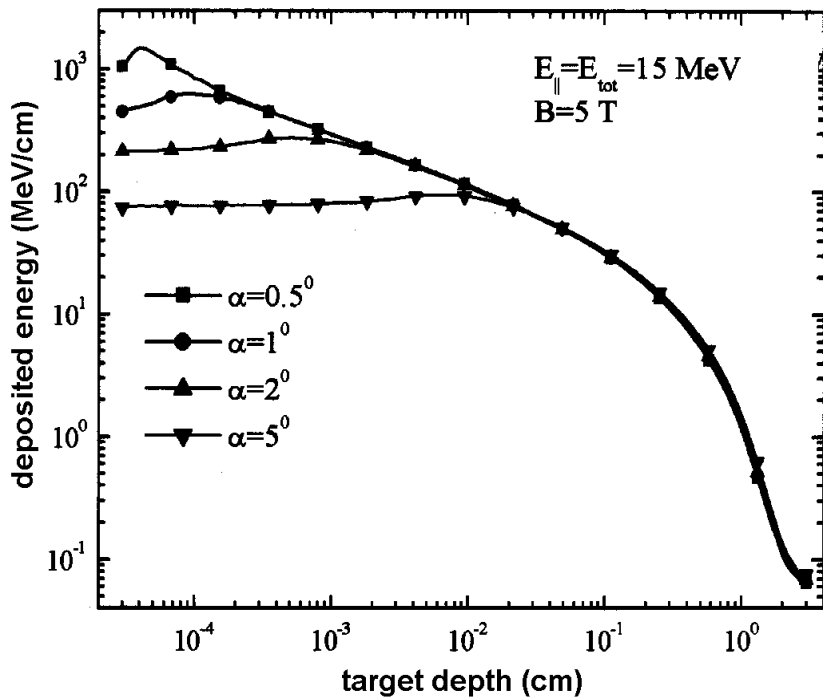


Fig. 54. Energy deposition profiles for 15 MeV electrons into graphite for different angles of the magnetic field lines with the target surface

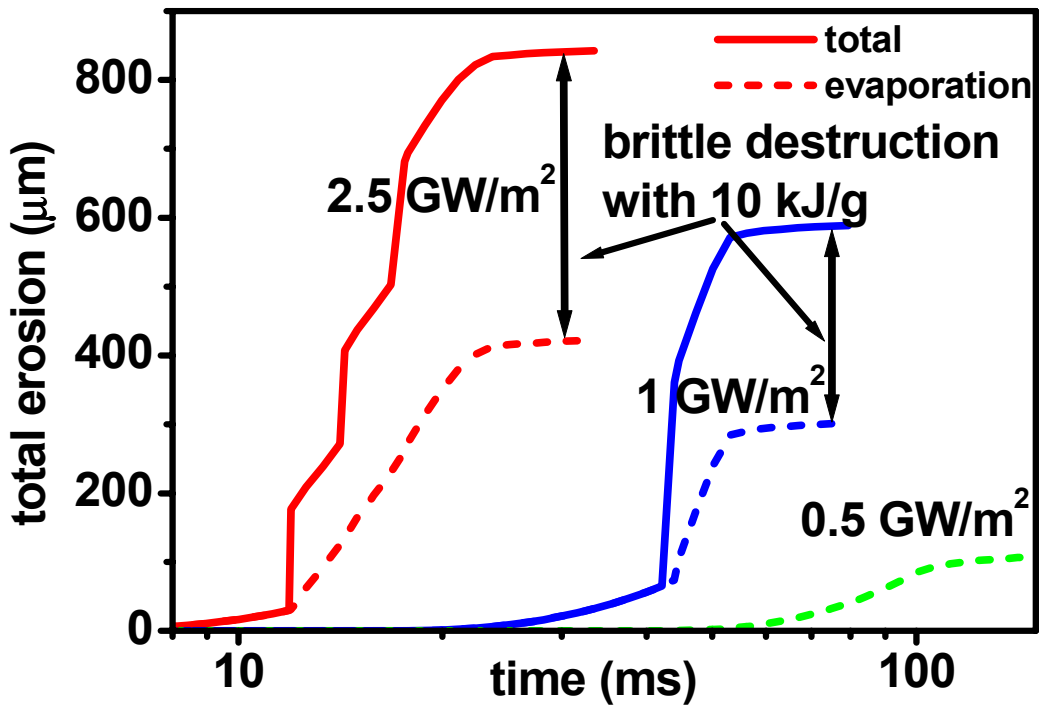


Fig.55a. Total erosion and evaporation of CFC graphite for 15 MeV runaway electrons with 50 MJ/m^2 . The inclination angle of the hot electrons is 1° .

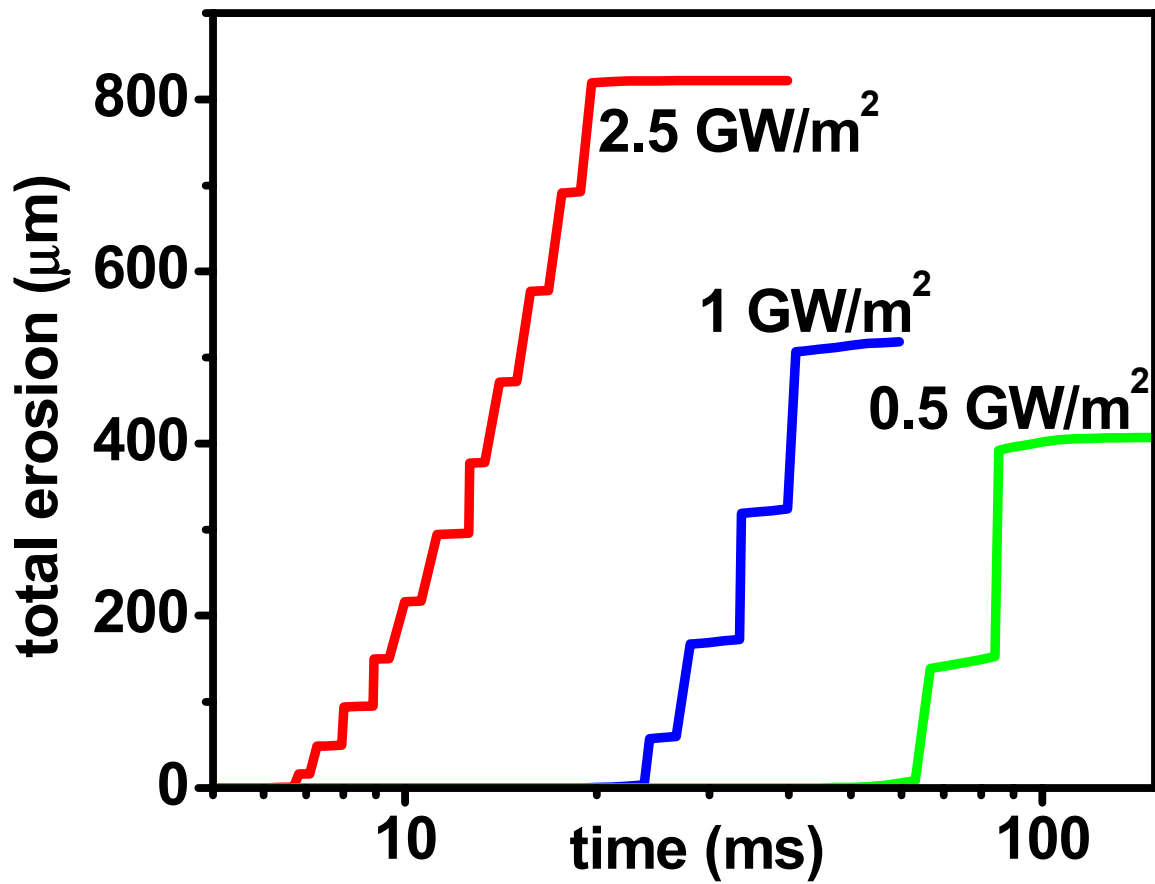


Fig.55b. Brittle destruction with 8 kJ/g for 15 MeV runaway electrons with 50 MJ/m². The inclination angle of the hot electrons is 1°. Evaporation accounts for 10 μm only.

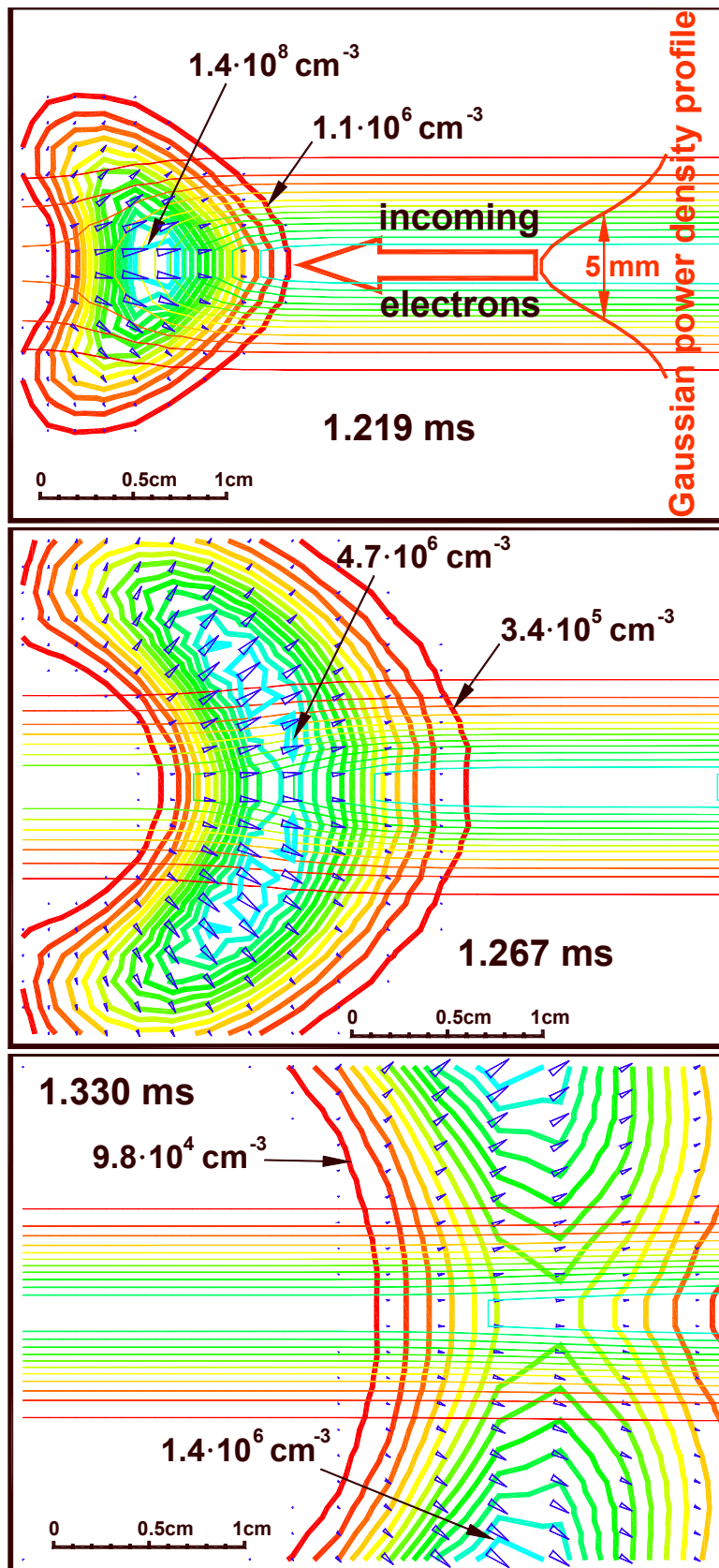


Fig.56. Expansion of the cloud of dust particles for JEBIS conditions at 3 different times after a brittle destruction event which occurs at 1.2 ms. Arrows show the dust particle flux. The thick solid lines are the density contours of the dust particle. The thin lines are the contours of the deposited energy. The vertical carbon target is at the left. Electrons are coming horizontally from the right.

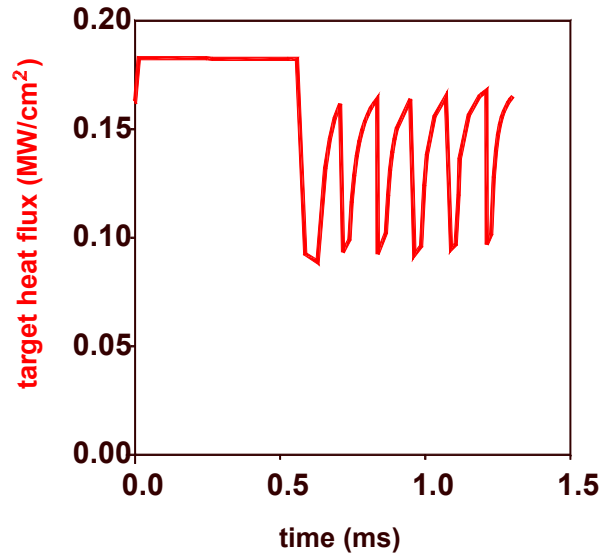


Fig.57. Energy deposition into the target for JEBIS conditions showing target screening by the dust particles after onset of brittle destruction and time duration of target shielding by the dust cloud.

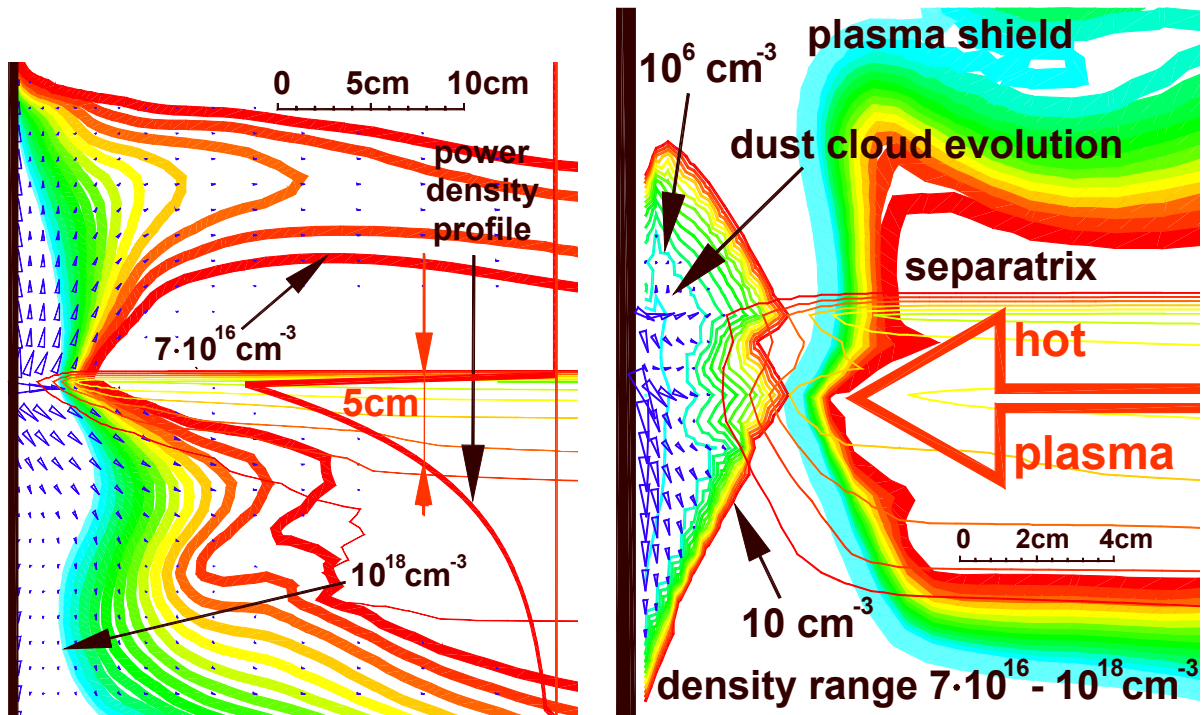


Fig.58. Density contours and plasma flow pattern for a perpendicular (horizontal) graphite target at 0.4 ms. Peak target heat load is 100 GW/m².

Fig.59. Motion pattern and densities in the dust cloud and in the plasma shield at 0.4 ms.

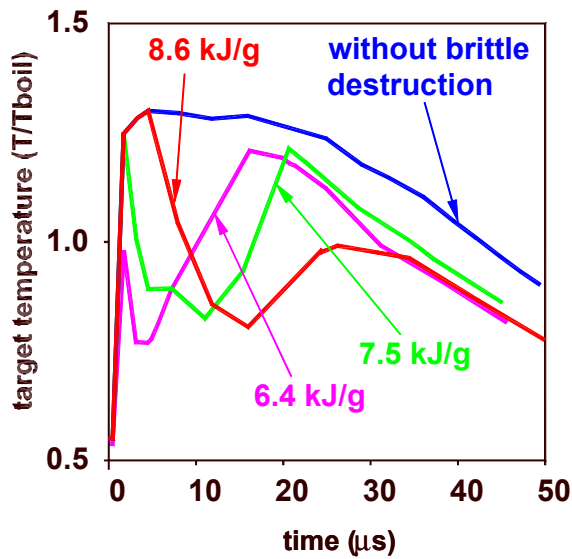


Fig.60. Target surface temperature evolution with brittle destruction showing the target screening effect for a perpendicular target for the MK-200 UG condition. Decreasing damage threshold values as indicated at the curves describe increase of brittle destruction

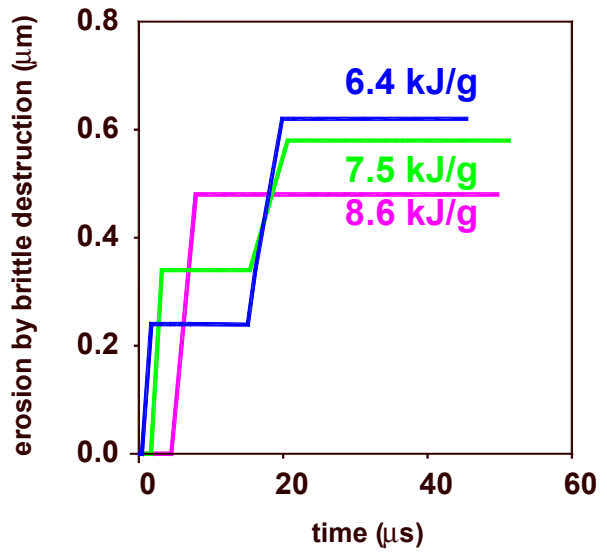


Fig. 61. Erosion by brittle destruction for different threshold values.

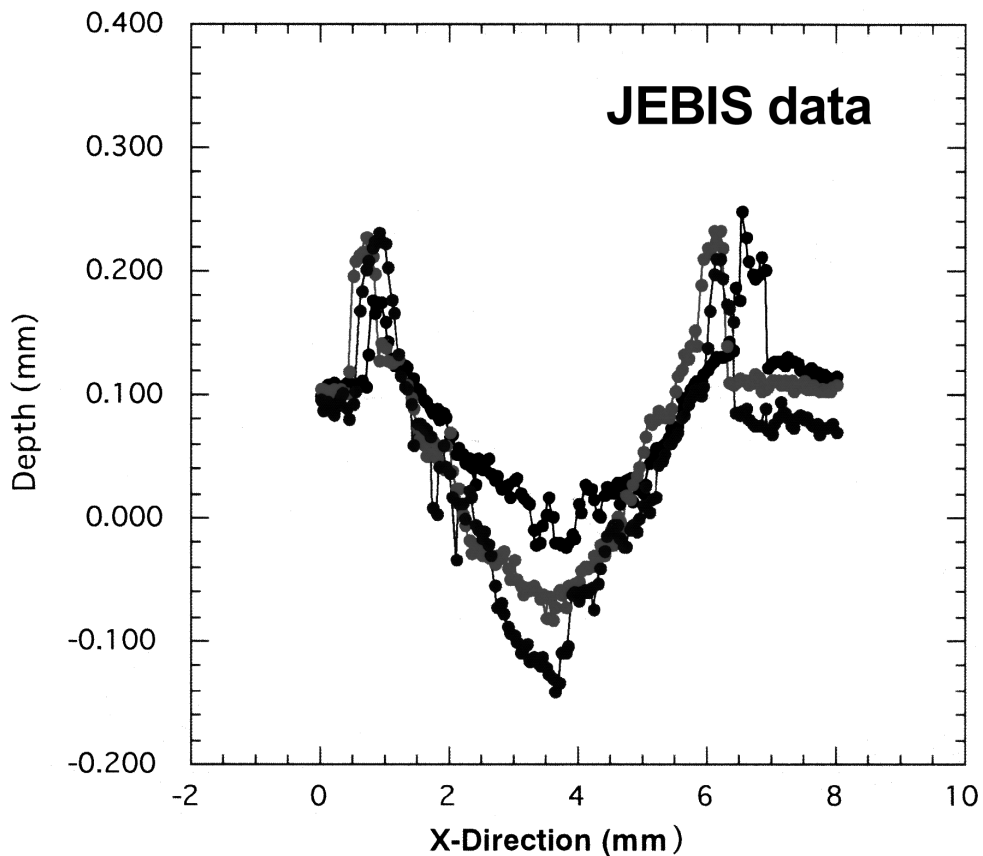


Fig. 62. Typical melt layer erosion profiles of tungsten targets under e-beam irradiation with 70 keV at JEBIS with perpendicular impact. The absorbed energy is 2.3 MJ/m^2 the time duration of the pulse is 1.8 ms. The initial temperature of the sample is 1000 K.

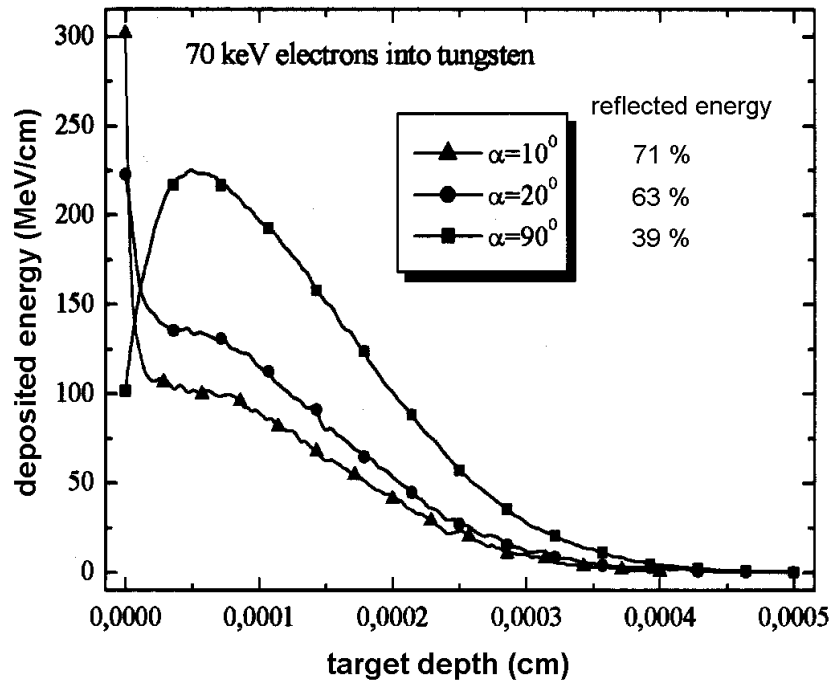


Fig.63. Energy deposition by monoenergetic electrons of energy 70 keV into tungsten with α the impact angle

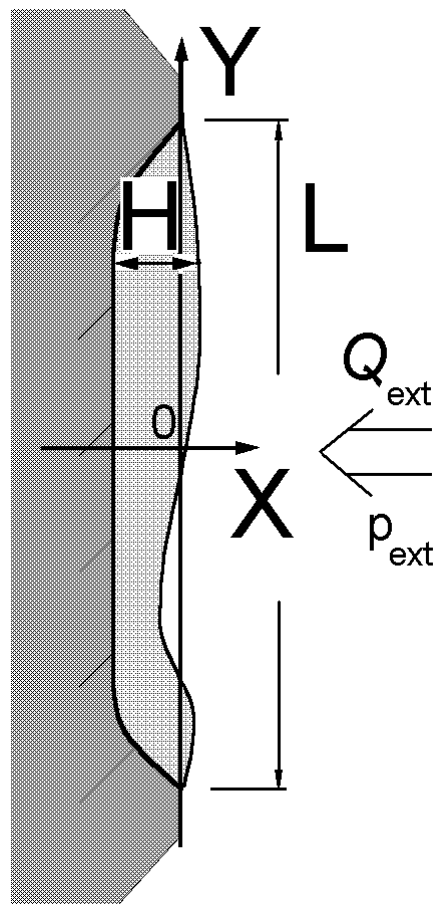


Fig. 64. Melt layer and melt motion schematically.

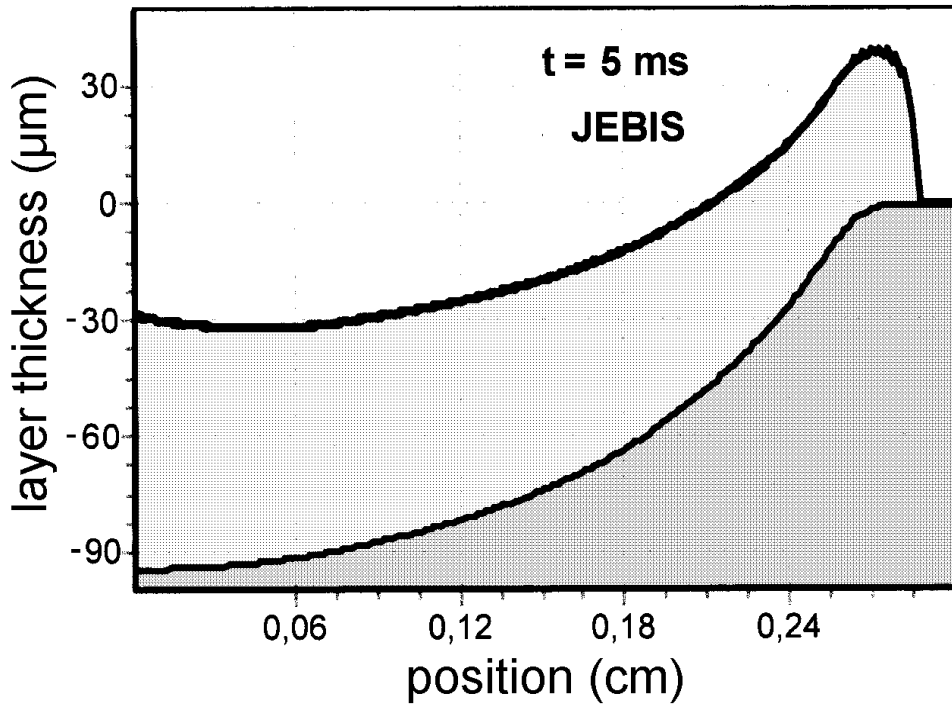


Fig. 65. Calculated melt layer erosion profile and thickness of the resolidified layer for a tungsten target at JEBIS. Initial target temperature is 1000K.

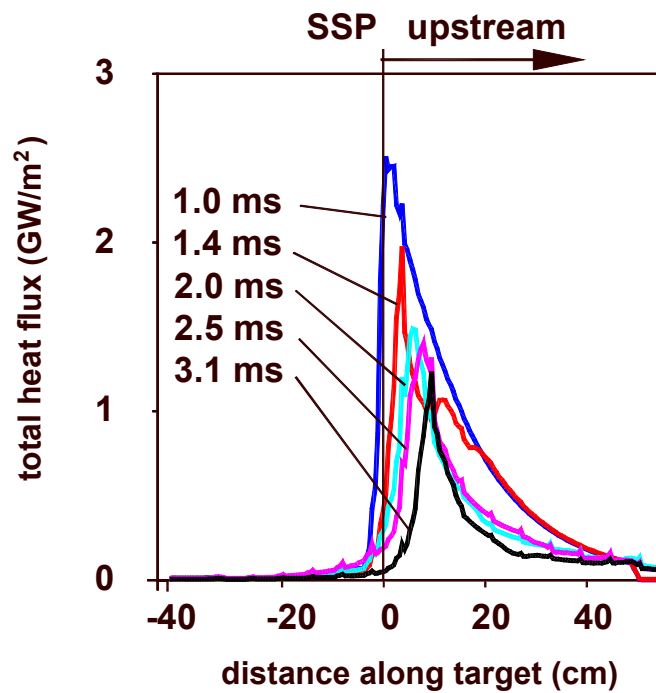


Fig. 66. Time dependent target heat load at a vertical tungsten target during a disruption with a target heat load of 3 GW/m² and a time duration of 3.1 ms.

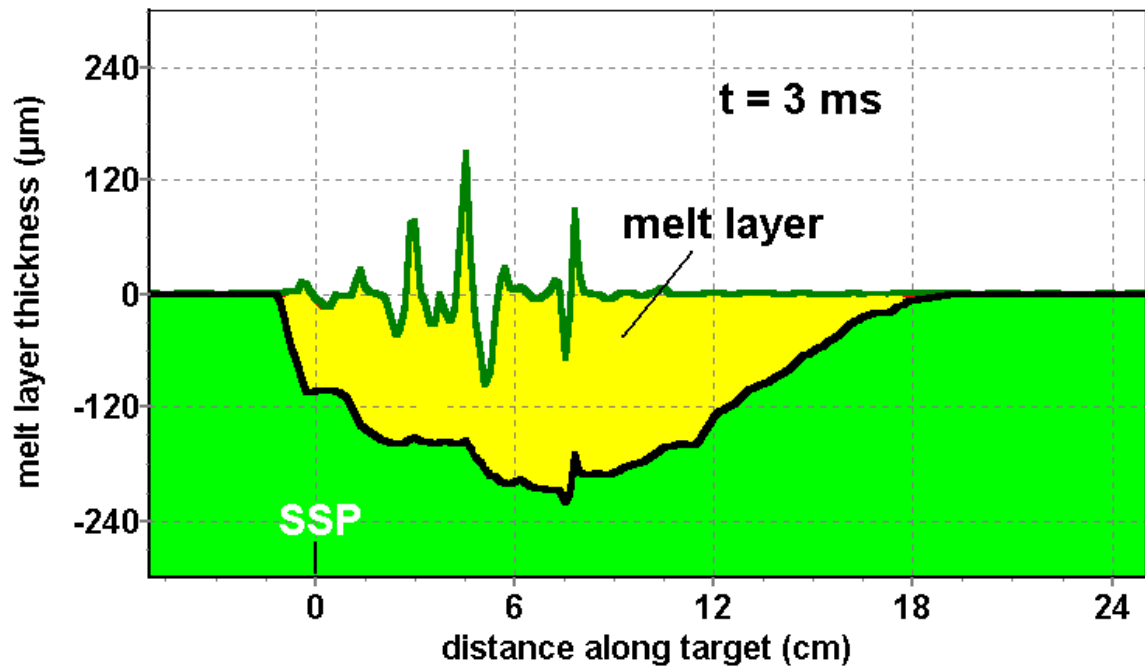


Fig. 67a. Calculated melt layer erosion profile for a tungsten vertical target for ITER-FEAT conditions for hot plasma impact with peak heat load of 3 GW/m² and 3 ms time duration at end of heating.

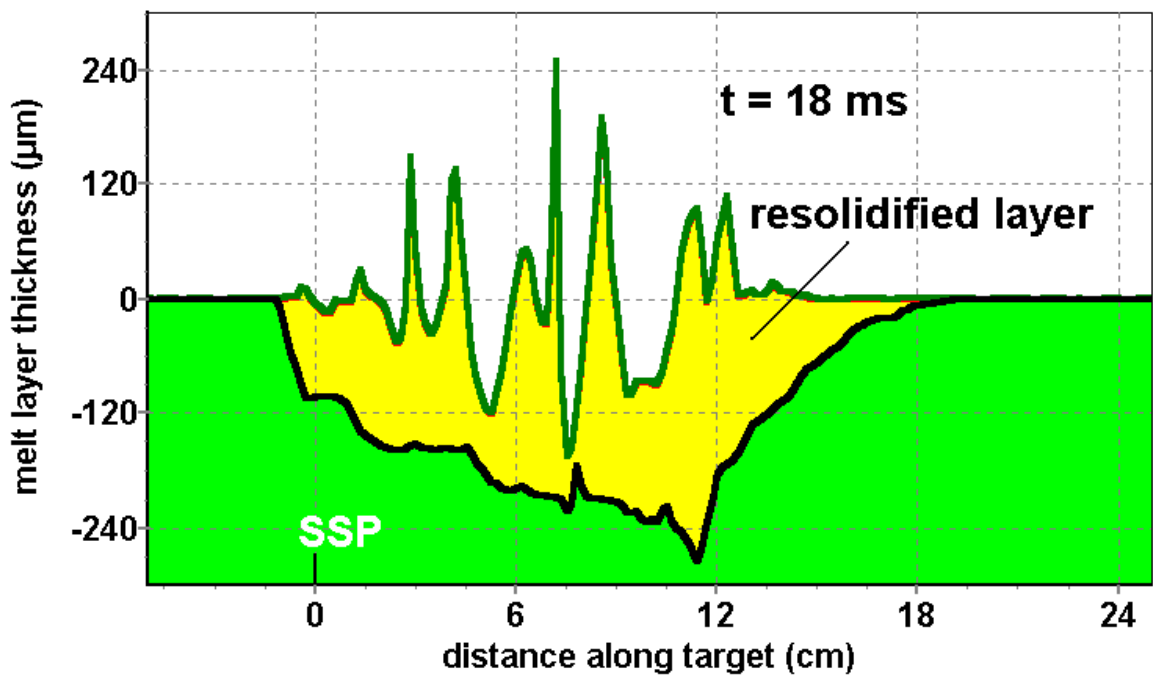


Fig. 67b. Calculated melt layer erosion profile and thickness of the resolidified layer after complete resolidification. The same conditions as in Fig. 67a.

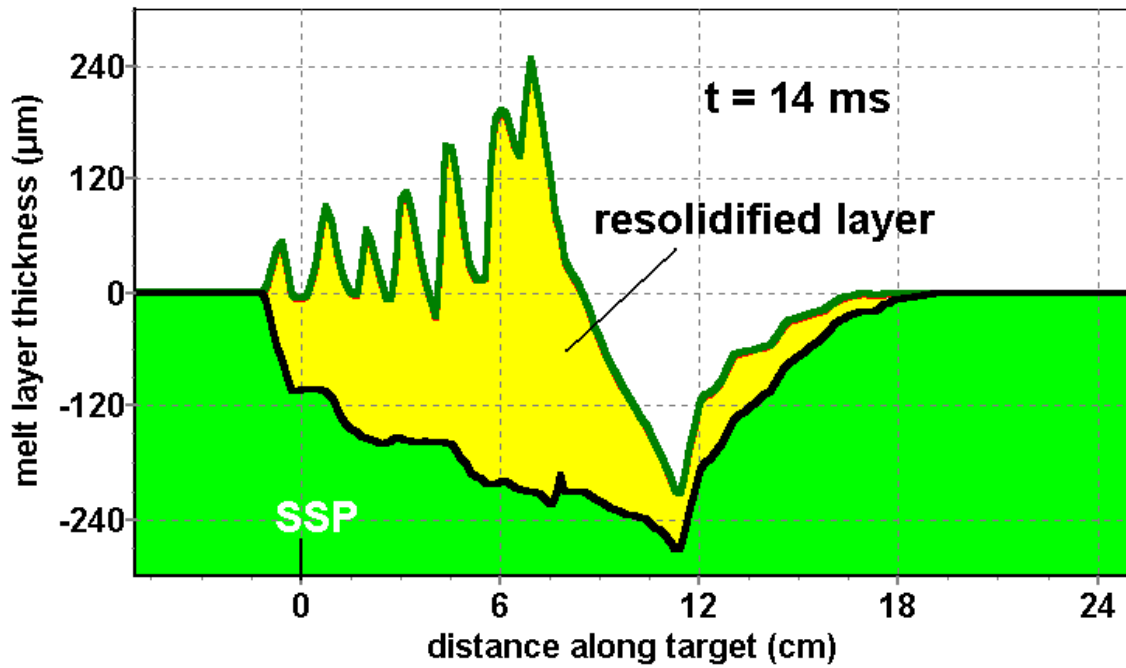


Fig. 67c. The same conditions as in Fig. 67a but with a target current density of 1 kA/cm^2 . The influence of the Lorentz force is demonstrated

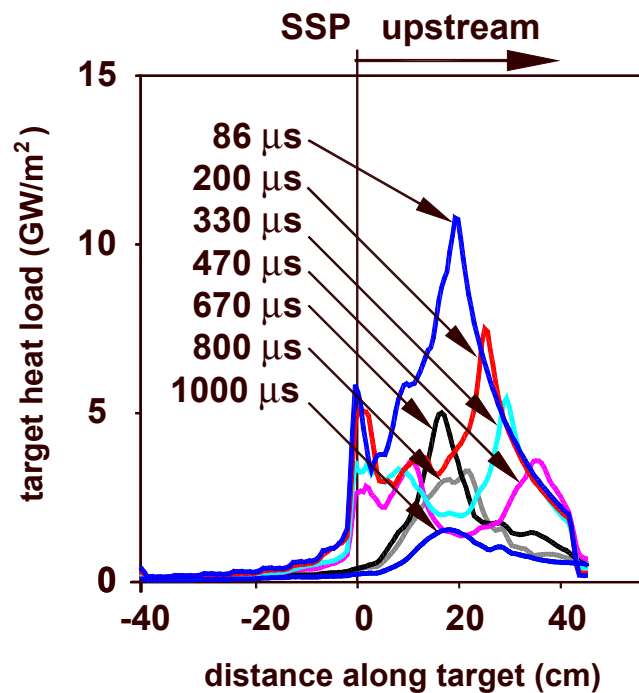


Fig. 68. Time dependent target heat load at a vertical tungsten target during a disruption with 30 MJ/m^2 and time duration of 1 ms.

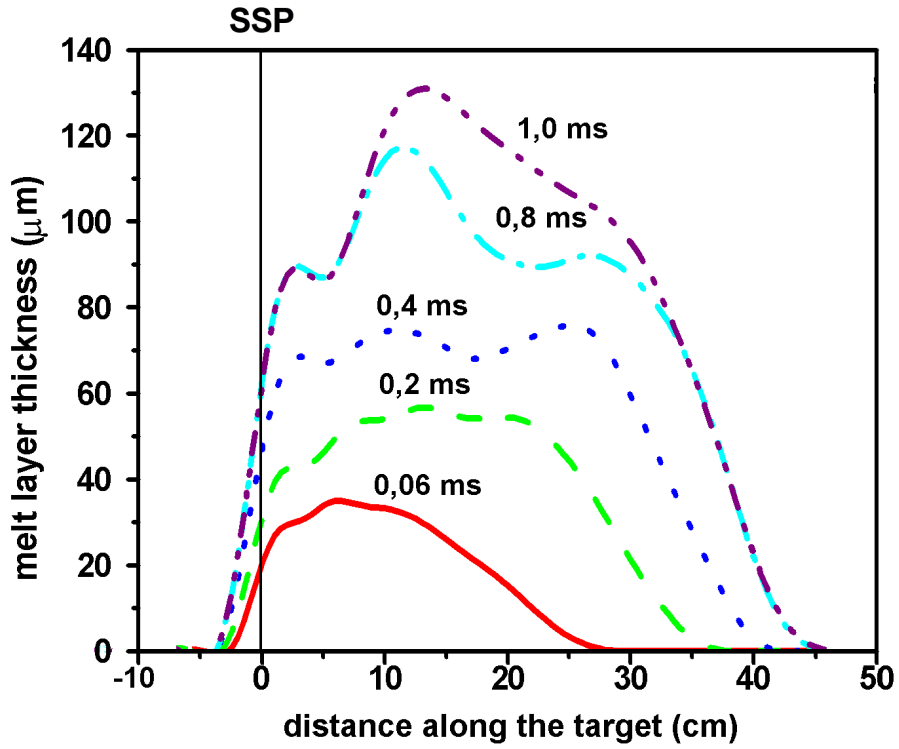


Fig. 69. Time dependent melt layer profiles at a vertical tungsten target. Target heat load is 30 GW/m^2 .

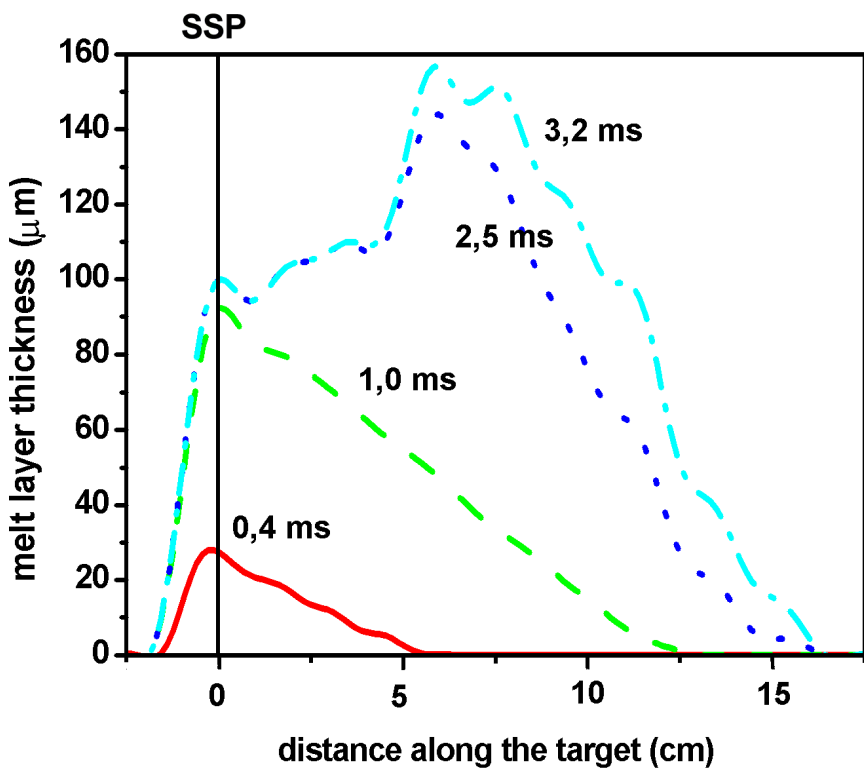


Fig. 70. Time dependent melt layer profiles at a vertical tungsten target. Target heat load is 3 GW/m^2 .

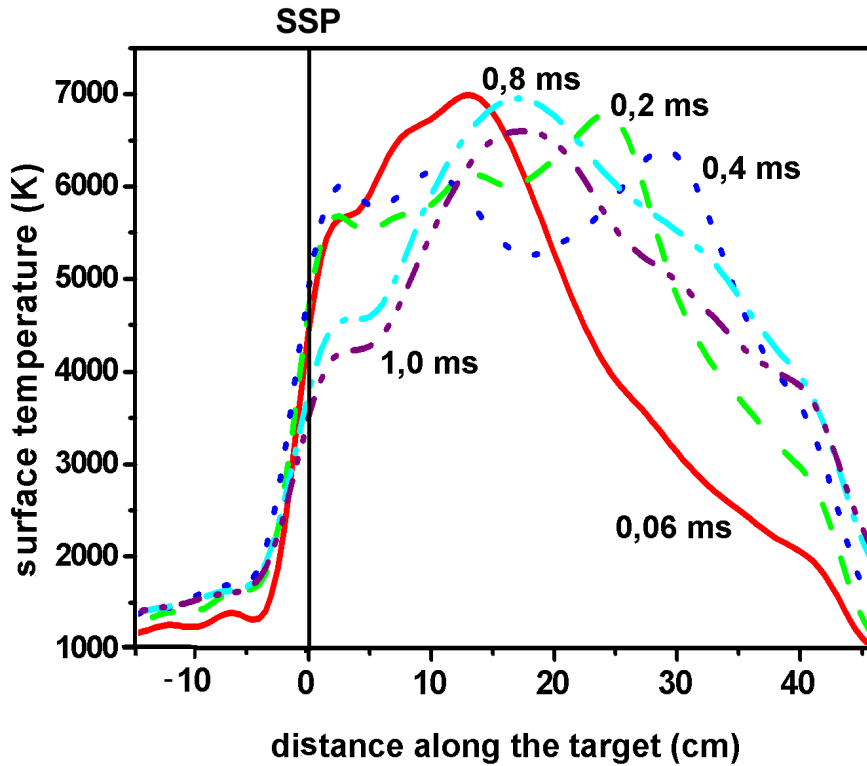


Fig.71. Time dependent surface temperature profiles at a vertical tungsten target. Target heat load is 30 GW/m^2 .

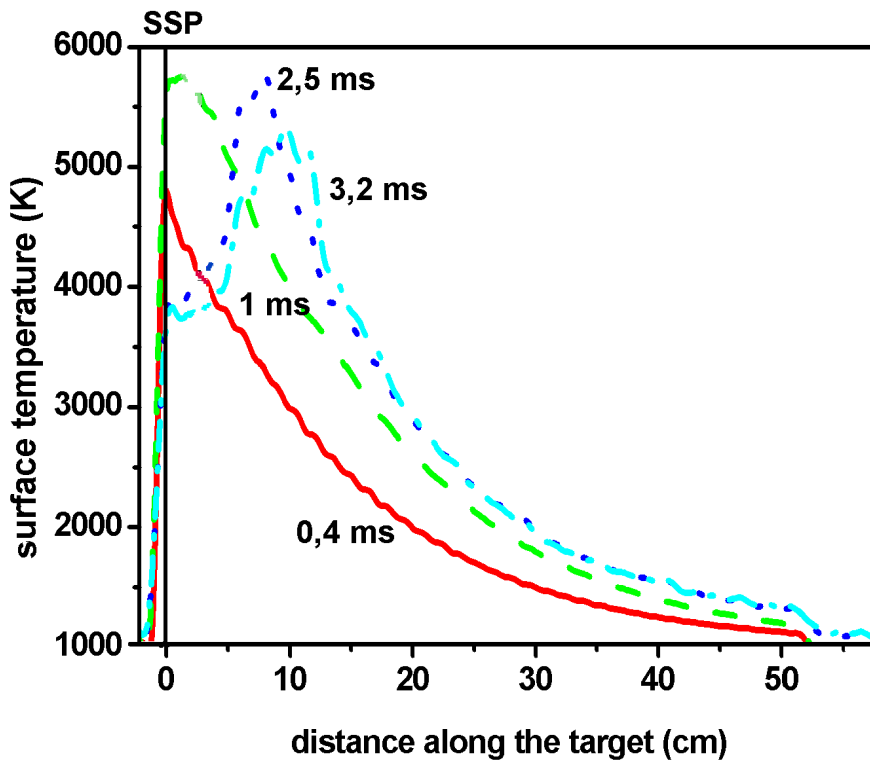


Fig. 72. Time dependent surface temperature profiles at a vertical tungsten target. Target heat load is 3 GW/m^2 .

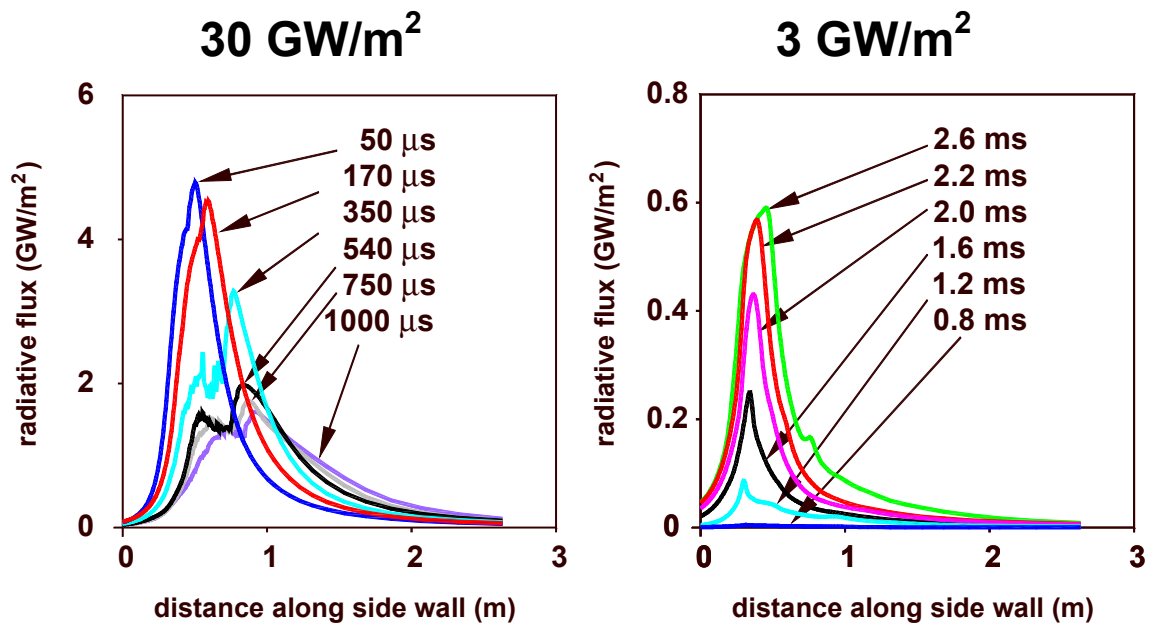


Fig. 73. Time dependent reradiation flux from carbon plasma shields to the inner side wall for a vertical graphite target and a separatrix – side wall distance of 40 cm.

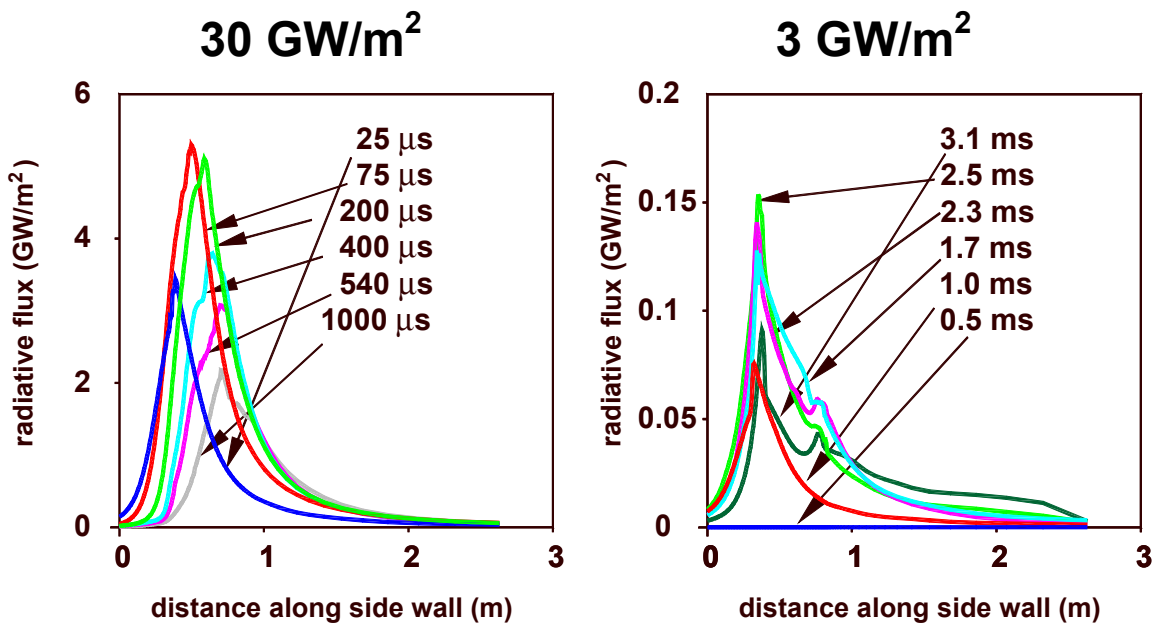


Fig. 74. Time dependent reradiation flux from tungsten plasma shields to the inner side wall for a vertical tungsten target and a separatrix – side wall distance of 40 cm.

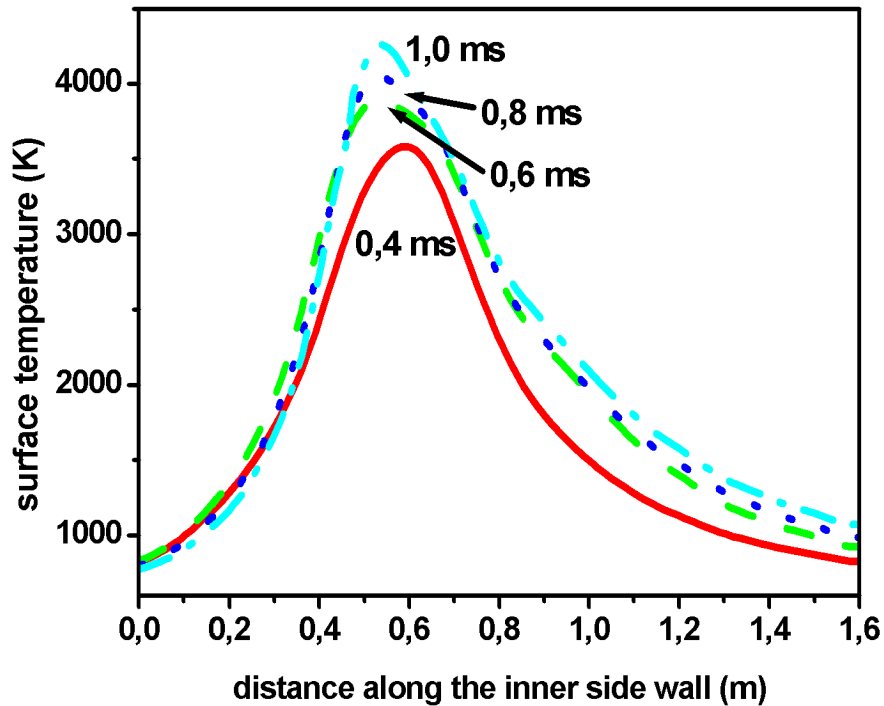


Fig. 75. Evolution of the surface temperature of tungsten inner side wall. Wall load from reradiation from a tungsten plasma shield with 30 GW/m^2 . The separatrix distance to the side wall is 0.24 m. The SSP is at the position $x=0.4\text{m}$ see Fig. 1.

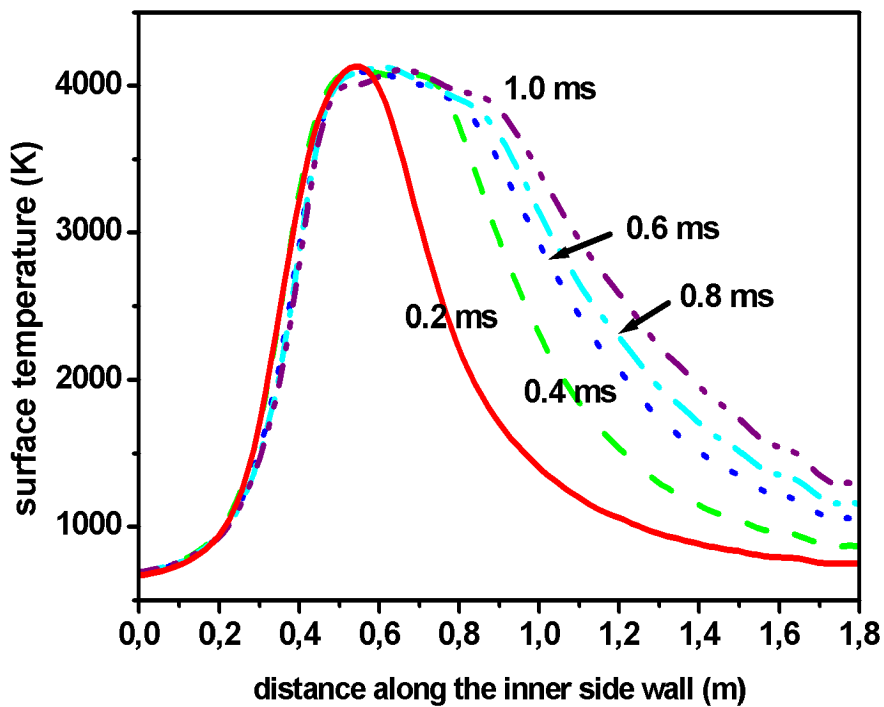


Fig. 76. Evolution of the surface temperature of carbon inner side wall. Wall load from reradiation from a carbon plasma shield with 30 GW/m^2 . The separatrix distance to the side wall is 0.24 m. The SSP is at the position $x=0.4\text{m}$.

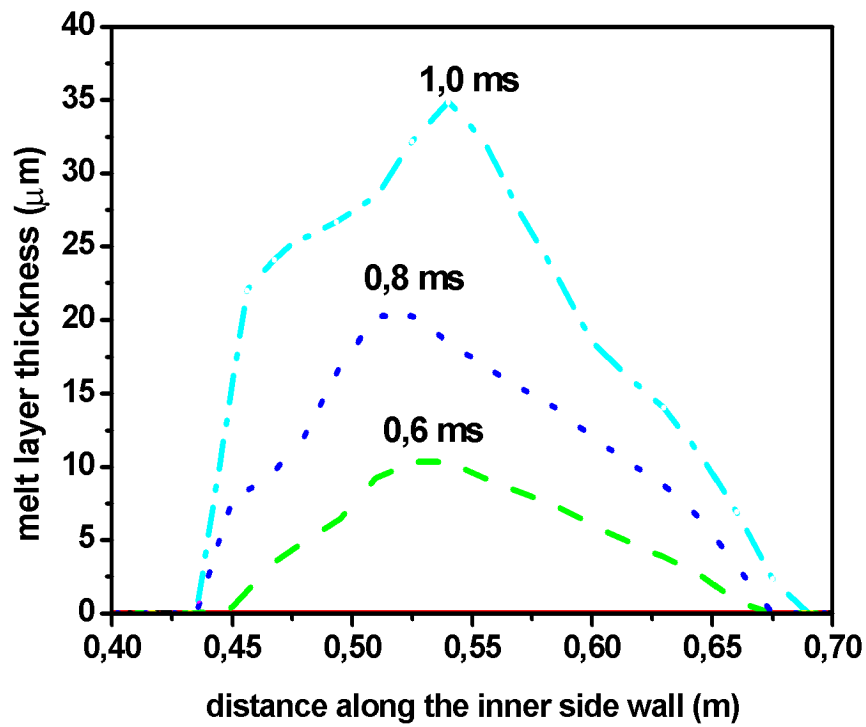


Fig. 77. Melt layer profiles at inner side wall. Wall load from reradiation from a tungsten plasma shield with 30 GW/m^2 .

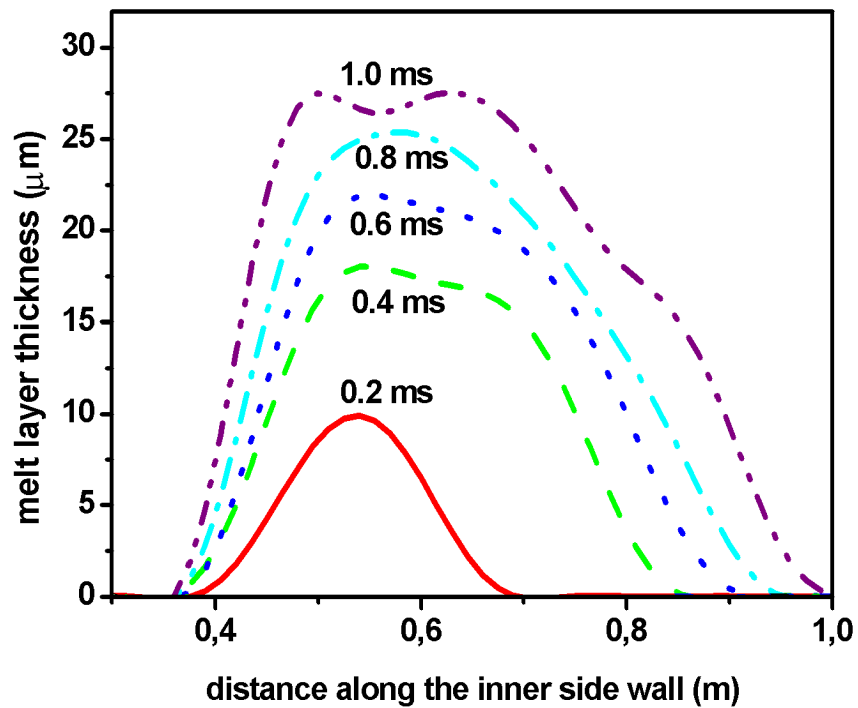


Fig. 78. Melt layer profiles at inner side wall. Wall load from reradiation from a carbon plasma shield with 30 GW/m^2 .

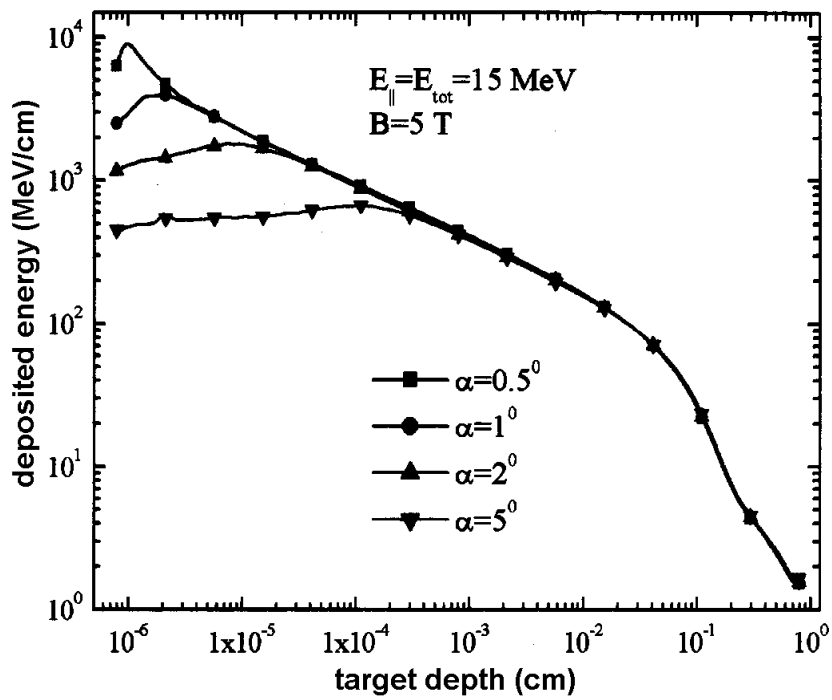


Fig. 79. Energy deposition profiles for 15 MeV electrons into tungsten. α the angle of magnetic field lines with the target surface

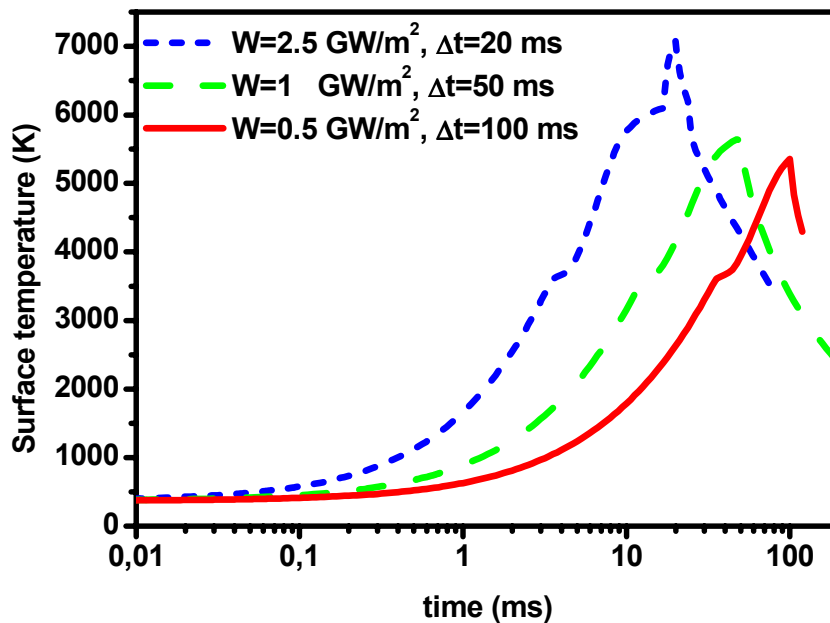


Fig. 80. Evolution of surface temperature for a tungsten target for 3 different heat loads of RAEs of energy deposition of 50 MJ/m^2 . Impact energy of the RAEs is 15 MeV, the impact angle is 1° and the initial temperature is 400K.

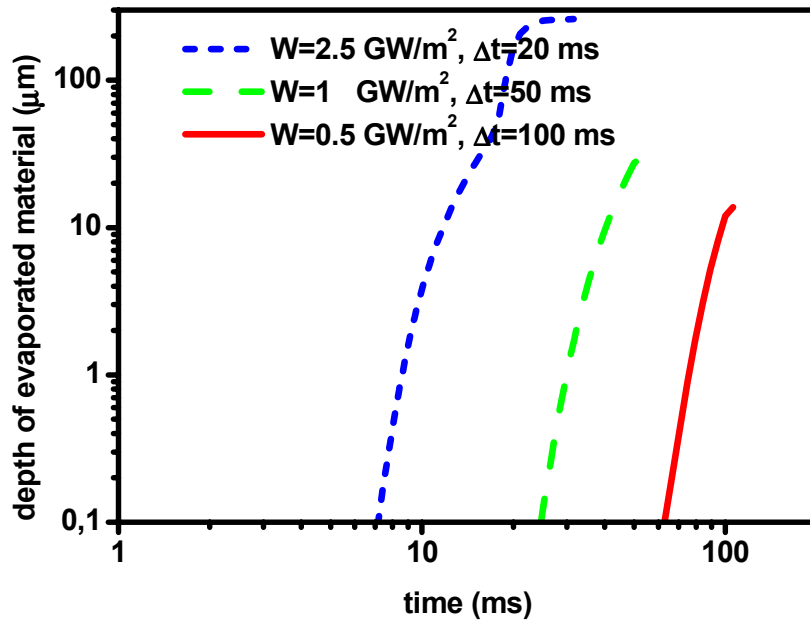


Fig. 81. Depth of evaporated tungsten for RAEs with 50 MJ/m^2 . The RAE impact energy is 15 MeV , the impact angle is 1° and the initial temperature is 400K .

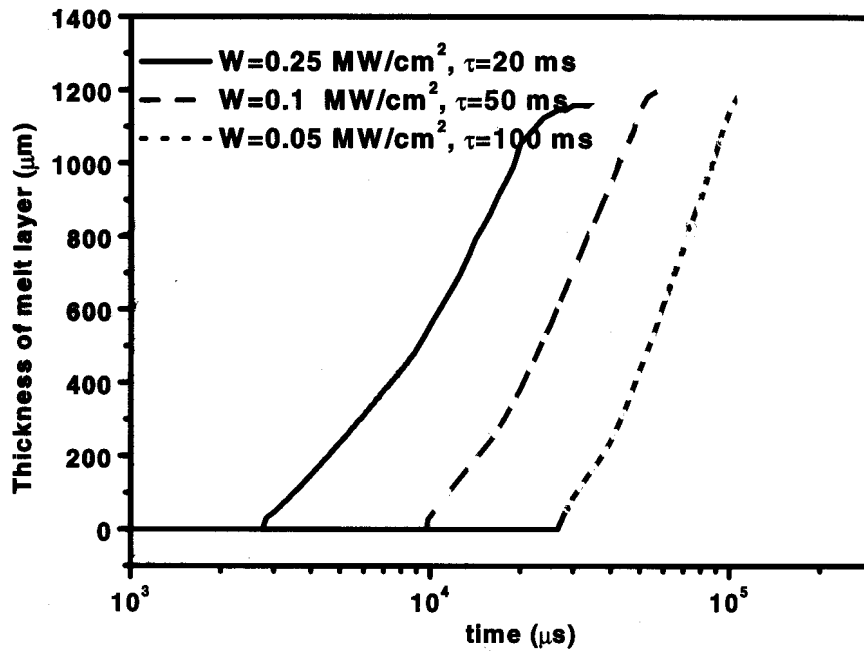


Fig. 82. Thickness of tungsten melt layer under RAE impact. The same conditions as under Fig. 81.

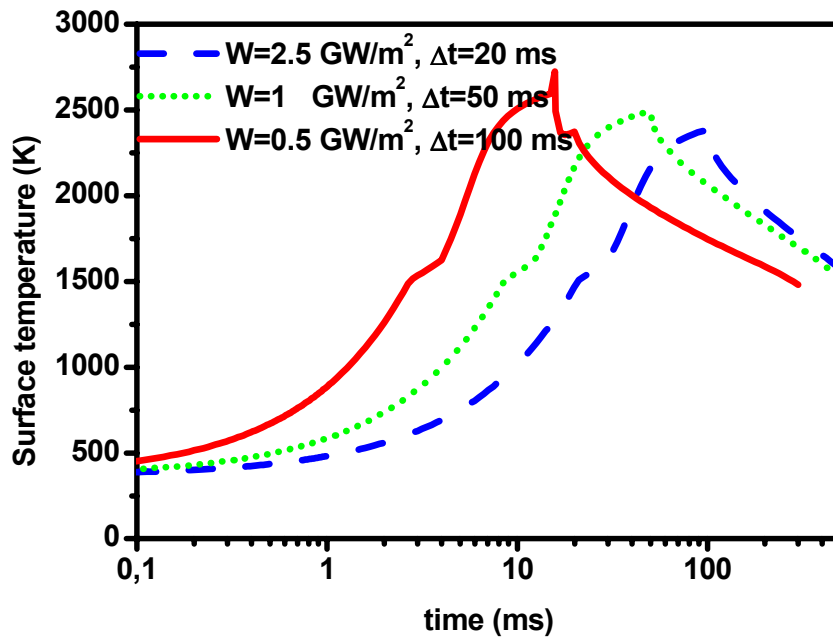


Fig. 83. Evolution of surface temperature for a beryllium target for 3 different heat loads of RAEs with 50 MJ/m^2 . The RAE impact energy is 15 MeV , the impact angle is 1° and the initial temperature is 400K .

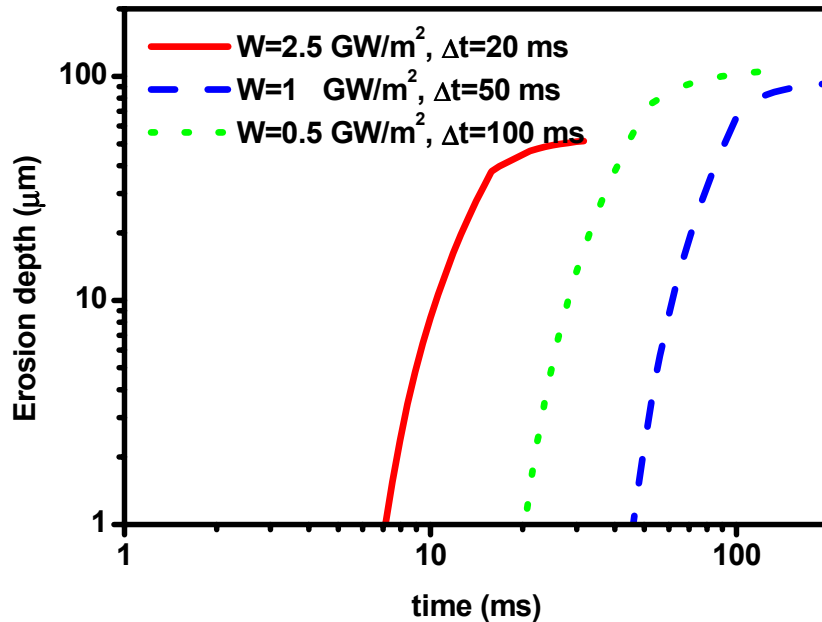


Fig. 84. Evaporation of beryllium under RAE impact with 50 MJ/m^2 . The RAE impact energy is 15 MeV , the impact angle is 1° and the initial temperature is 400K .

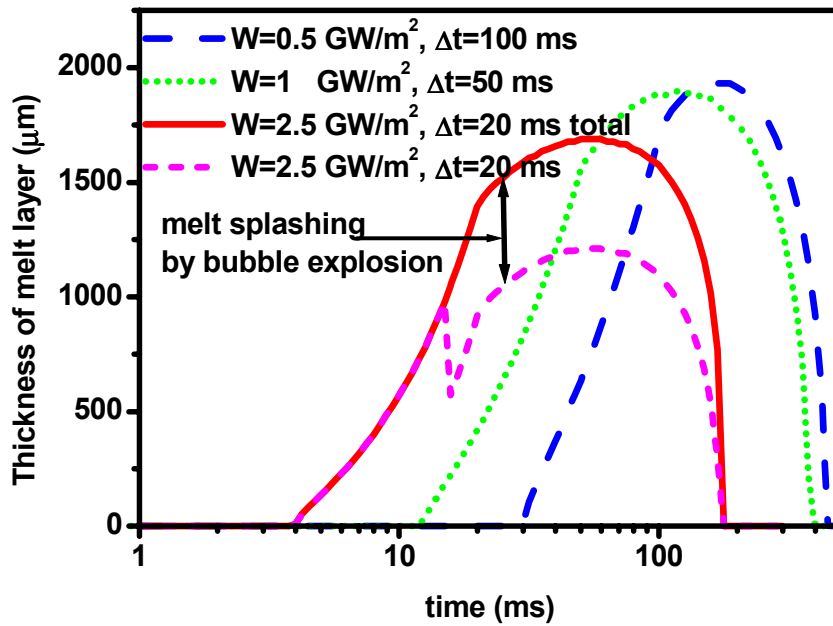


Fig. 85. Thickness of beryllium melt layer under RAE impact. The RAE impact energy is 15 MeV, the deposited energy is 50 MJ/m², the impact angle is 1° and the initial temperature is 400K

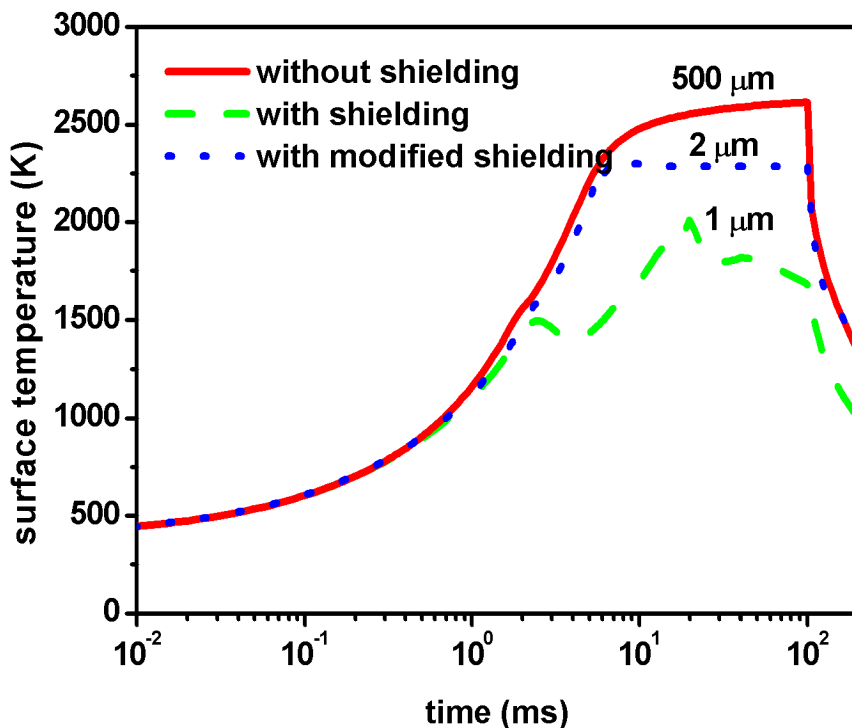


Fig. 86. Comparison of evolution of surface temperature of beryllium for a typical VDE event with 0.5 GW/m² and time duration of 100 ms. The number at the curves indicate the erosion by vaporization.

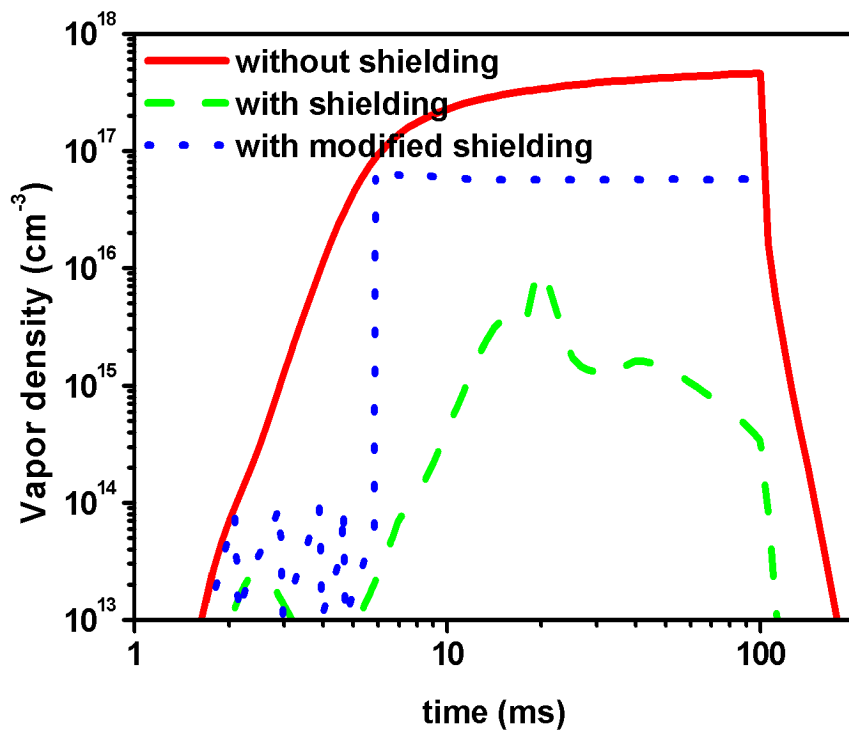


Fig. 87. Comparison of evolution of beryllium vapor density in front of the target without and with shielding. The same VDE event as given under Fig. 86 is used.

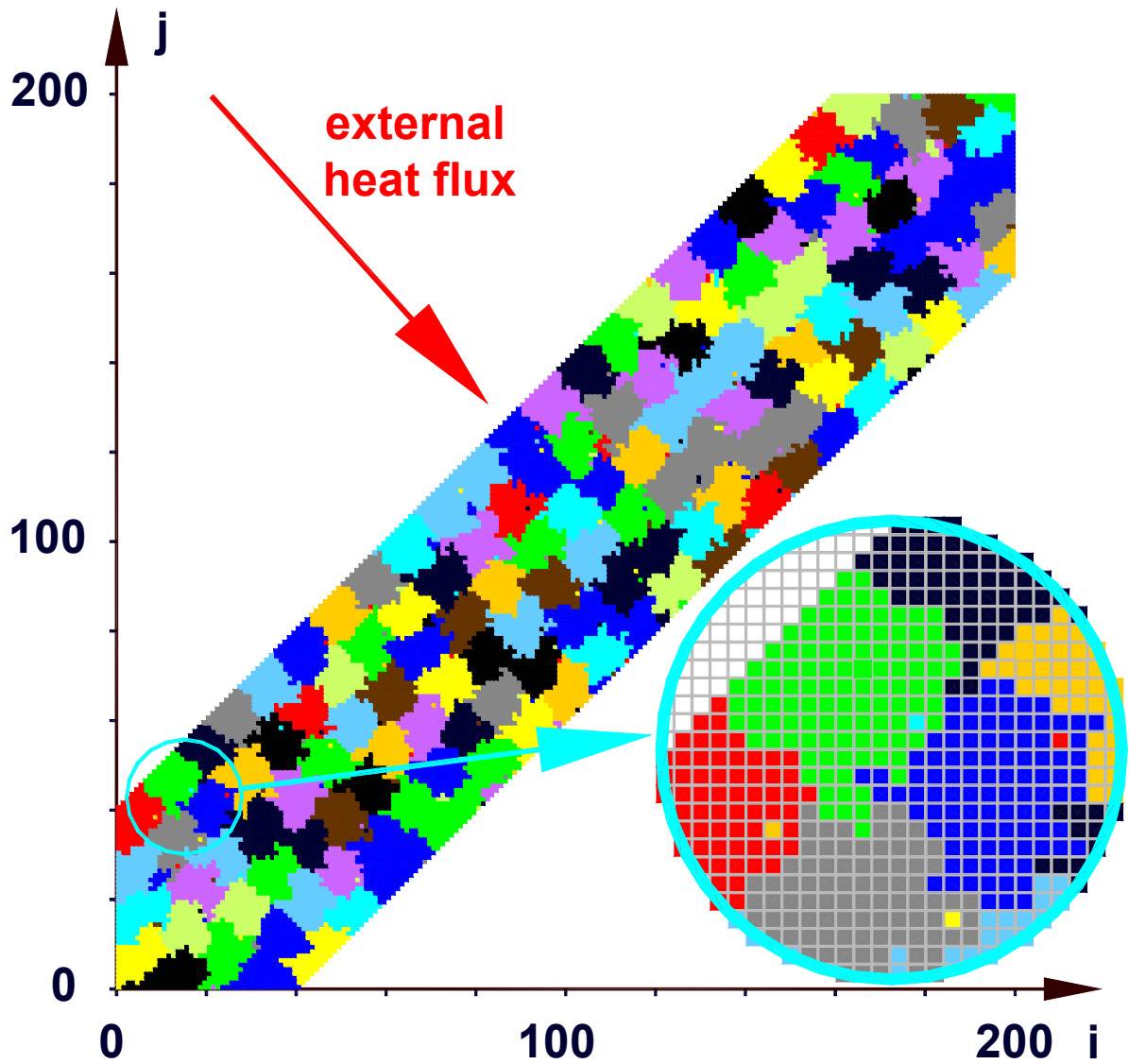


Fig.88. Rectangular lattice as used in the numerical simulation of graphite with a Gaussian distribution of the grain sizes. The mean grain consists of 55 cells of identical size a . The detailed description of the model is given in the appendix.

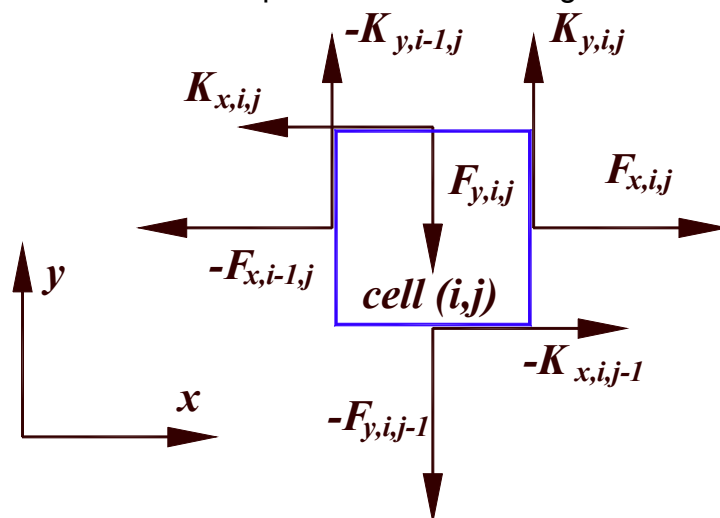


Fig. 89. Elastic forces acting on a cell with coordinates (i,j) from neighbouring cells.

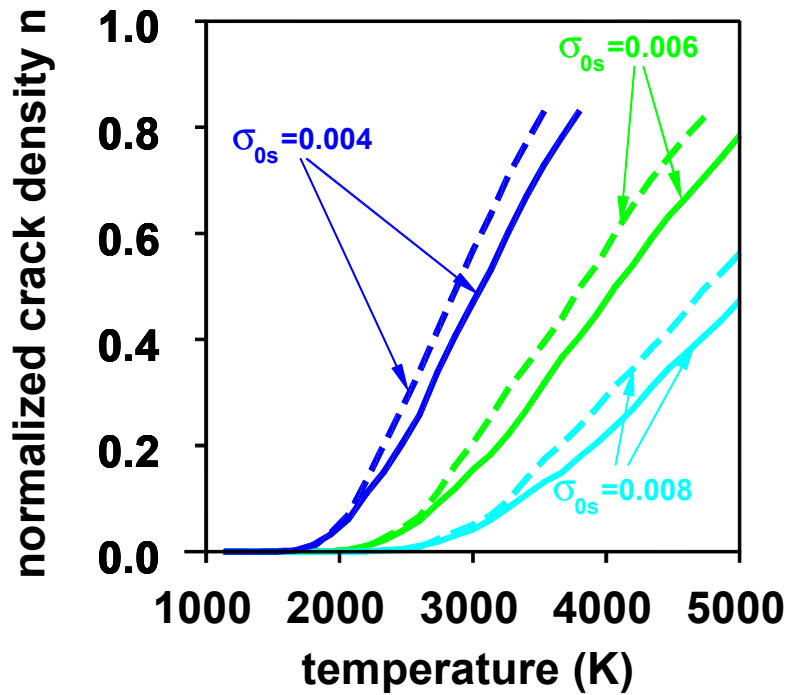


Fig. 90. Crack generation for different failure stress values for a uniformly heated graphite sample for two different lattices with the same mean grain size of $1.7\mu\text{m}^3$ but with 3 (solid curve) and 20 (dashed curve) cells per mean grain

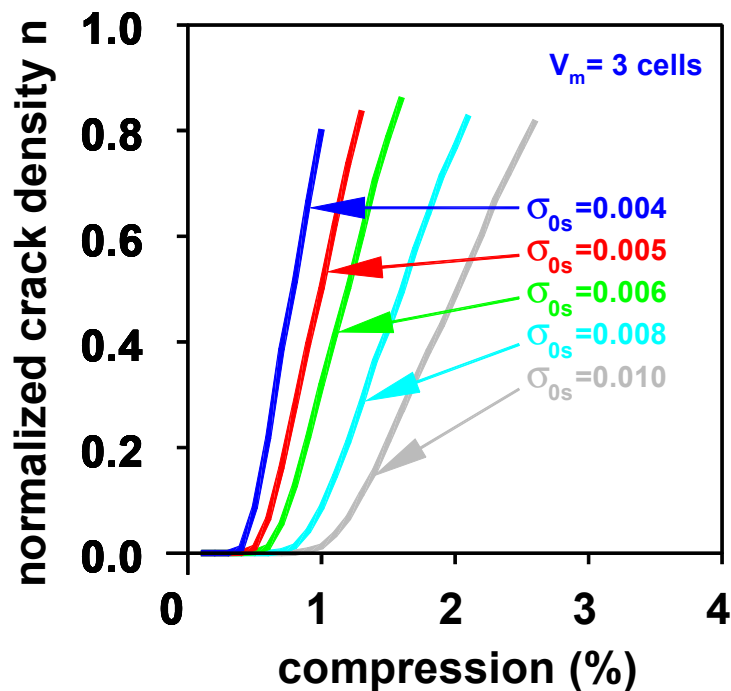


Fig. 91. Crack generation due to uniform compression of a graphite sample for different values of the failure stress for the surface bonds. Compression is given as $\Delta L/L$ with L the thickness of the sample. The mean grain consists of 3 cells

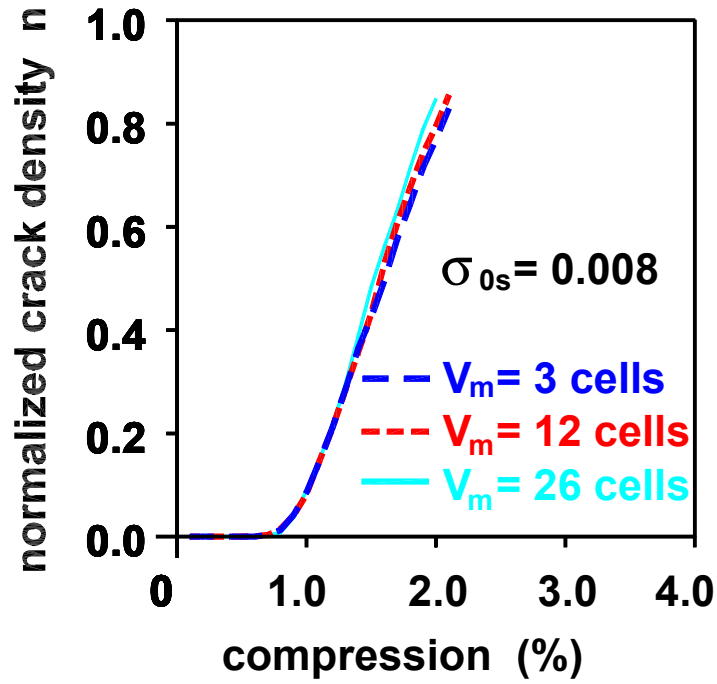


Fig. 92. Crack generation for uniform compression for a fixed failure stress value σ_{0s} of 0.005 and for 3 different mean grain sizes with 3, 12 and 26 cells. The cell size is $1 \mu\text{m}$ for the mean grain with 12 and 26 cells and $0.4 \mu\text{m}$ for that with 3 cells

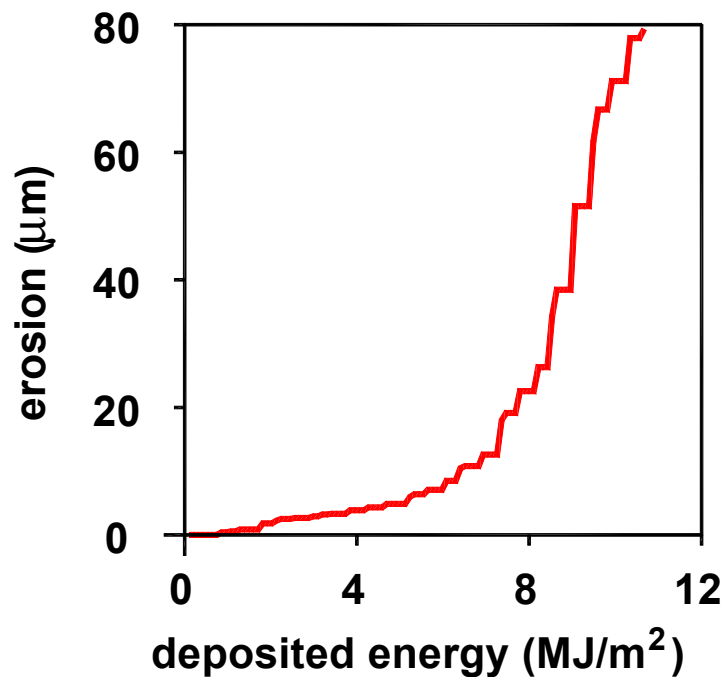


Fig. 93. Onset of brittle destruction as function of the deposited energy for the GOL-3 experimental condition with volumetric heating with $200 \text{ MW}/\text{cm}^2$. The critical failure stress value is $\sigma_{0s} = 0.005$. The energy deposition range is up to 500 microns, time duration is $5 \mu\text{s}$

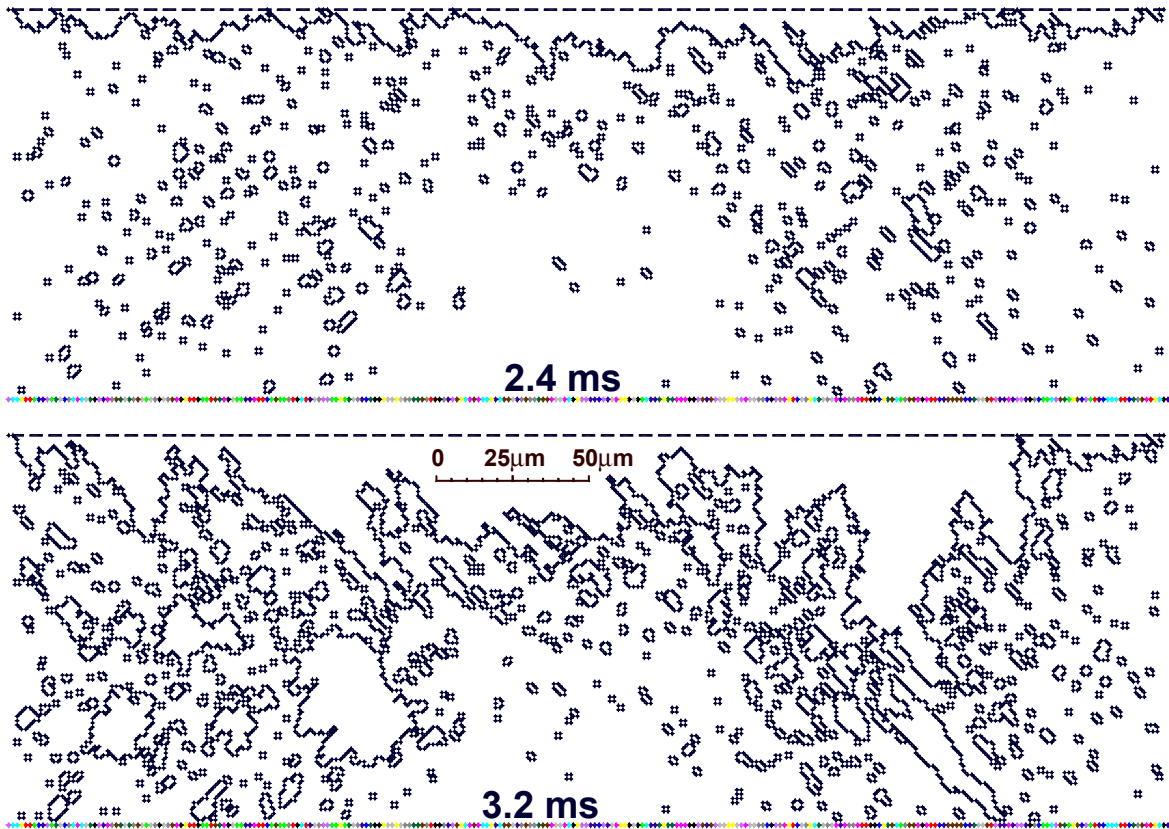


Fig. 94. Crack propagation and evolution of brittle destruction for volumetric heating, simulating run away electrons with a power density of 2.5 GW/m^2 at two different times

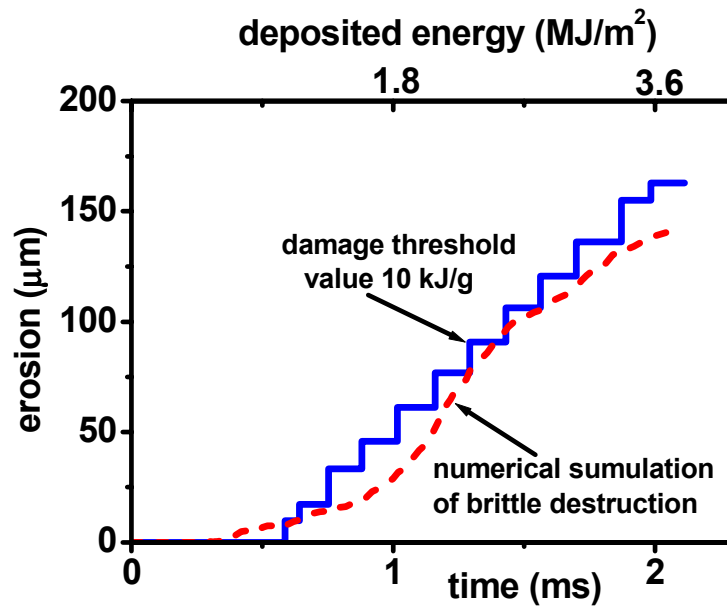


Fig. 95. Comparison of calculated erosion rates by brittle destruction for pyrolytic graphite for JEBIS conditions. Initial sample temperature is 1200 K